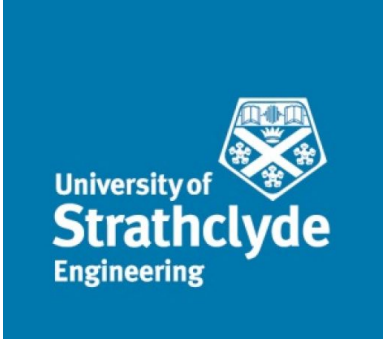

Combining Microfluidics with Raman Spectroscopy for the Study of Emerging Cancer Therapies

EngD Thesis

Jacob Melnyk

Centre for Doctoral Training in Medical Devices and Health Technologies
Department of Biomedical Engineering
University of Strathclyde, Glasgow

June 17, 2021

This thesis is the result of the author's original research. It has been composed by the author and has not been previously submitted for examination which has led to the award of a degree.

Abstract

Lipid synthesis is known to be upregulated in cancerous cells in order to promote their growth and survival. Recently, drugs targeting the lipid synthesis pathway have become a research interest for new anti-cancer therapy applications. Label-free Raman spectroscopy has been demonstrated as an analysis technique that can measure changes in the lipid content of cancerous cells when treated with such drugs. In this thesis, a microfluidic device was developed which aims to provide a miniaturised platform on which to study the lipid content of single cancerous cells when treated with lipid synthesis targeting drugs. This is the first report of a microfluidic device being used for this application.

PDMS, a common material used for microfluidics, was found to be incompatible with lipid Raman spectroscopy due to peaks within its Raman spectrum overlapping with those from cellular lipids. Fluorinated ethylene propylene (FEP), a type of Teflon, was selected as an alternative material as its Raman spectrum does not overlap with that of the lipids being measured. Many of the processes used to create the FEP microfluidic devices had to be developed and optimised, and device designs were revised due to limitations with FEP. Cancerous and non-cancerous prostate cell lines PC3 and PNT2, were seeded in the device and treated with the fatty acid synthase inhibitor Orlistat or steroyl-CoA desaturase inhibitor CAY10566. Raman spectroscopy revealed a significant increase in lipid content for PC3 cells treated with Orlistat ($p < 0.0001$), but not for PNT2 cells, nor for either cell line treated with CAY10566. In comparison, both PC3 and PNT2 cell lines showed a significant increase in their lipid content when treated with orlistat in glass-bottomed dishes and glass coverslips ($p < 0.0001$).

While changes in the lipid content of PC3 cells were successfully detected in the devices, difficulties in creating and operating FEP microfluidic devices led to the conclusion that FEP is not recommended as a material for microfluidics unless absolutely necessary. A number of potential future developments to the device are discussed with the aim of improving its function and increasing its novelty. This thesis presents one of the first attempts to apply an FEP-based microfluidic chip to a specific biological application and is the only report to utilise Raman spectroscopy in combination with FEP microfluidics.

Acknowledgements

I would like to thank The EPSRC, the Centre for Doctoral Training in Medical Devices and Health Technologies, Duncan Graham and Michele Zagnoni for providing this opportunity.

I would also like to thank Corinna Wetherill for help with maintaining the cell cultures and Lauren Jamieson also for help with maintaining cell cultures and for providing much of the ground work for this project.

I would like to thank Mynie, Scott, Audrey, Josh, Pretheepan, John, George and the bar staff at Ark for their support and keeping me sane throughout the course of the project.

Finally, I would also like to thank Beth for her support and for nagging me into finishing this thesis.

Contents

List of Figures

List of Tables

List of Tables

Chapter 1.

Introduction

Lipid synthesis is upregulated in cancerous cells [1] due to their importance in rapid proliferation, migration and survival [2–4]. Inhibition of the lipid synthesis pathway has been shown to have an anti-tumour effect and therefore monitoring the effects of drugs which inhibit this pathway could lead to new cancer therapies [5–9]. Raman spectroscopy has been demonstrated as a non-destructive tool which can be used to estimate cellular lipid content [10]. This thesis aims to build upon this research by investigating the compatibility of Raman lipid analysis with a miniaturised microfluidic platform for culturing, treating and imaging single cells. In this chapter, the background behind lipid metabolism in cancer cells and its importance is discussed, followed by an overview of Raman spectroscopy and how it can be applied to study cellular lipids. Finally, a discussion of microfluidics, including materials, theory and application to drug screening, is presented.

1.1 Lipid Metabolism in Cancer cells

Cancerous cells are reported to have upregulated *de novo* lipid synthesis [1] and drugs that inhibit stages in related pathways, such as the fatty acid synthase inhibitor Orlistat, have been shown to have an anti-tumour effect [5]. Since normal cells rarely produce their own lipids, instead acquiring them from exogenous sources [11], it is believed that drugs targeting *de novo* lipid synthesis can therefore be used to specifically target cancer cells, making them a current research interest, as reviewed by Omabem Ezeani and Omabe [12]. This section will introduce the basic biochemistry of lipids, discuss how and why their metabolism is altered in cancer, and will review recent research into drugs affecting lipid synthesis for anti-cancer applications.

1.1.1 Lipids

Lipids are a diverse class of biomolecules defined as being poorly, if at all, soluble in water, but are soluble in organic solvents such as chloroform or toluene [13]. Although this definition includes molecules such as sterols, this thesis is primarily focused on fatty acid containing lipids such as fats, phospholipids, sphingolipids and eicosanoids.
Fatty acids consist of a long hydrocarbon chain with a carboxyl group at one end. Fatty acids may be saturated if they do not contain carbon-carbon double bonds or unsaturated if they contain one or more carbon-carbon double bonds. To form a fat such as a triglyceride, three fatty acid chains bond to a glycerol molecule through their carboxyl groups (Figure 1.1.A). Phospholipids consist of two fatty acids bonded to a glycerol molecule in the same way as in a fat, however the third hydroxyl group of the glycerol molecule is bonded to a phosphate group [14]. This phosphate group can be linked to a variety of other small molecules including choline, serine and glycerol1 (Figure 1.1.B). The phosphate and additional groups of phospholipids are commonly referred to as the 'head' and are hydrophilic, whereas the hydrophobic fatty acid chains are referred to as the 'tails'. Due to the hydrophilic and hydrophobic natures of each end of the molecule, phospholipids will self-assemble to form a bilayer structure in aqueous environments so that their tails are shielded on the inside with their heads facing outward (Figure 1.1.C).
Fats are stored in adipose tissue which is used for storing energy, insulating the body and protecting vital organs. Due to their self-assembly into bilayers, the main function of phospholipids is to form the bulk of cellular membranes. Membranes are vitally important as they provide barriers around cells and organelles, controlling the movement of substances through proteins embedded in the lipid bilayer [14].
Other fatty acid containing lipids include sphingolipids and eicosanoids [13, 15, 16]. Sphingolipids are themselves diverse in structure, but typically consist of a head group, a sphingosine tail and an additional fatty acid tail (Figure 1.2.A). Sphingolipid function can vary from being a structural part of a membrane to cell signalling [13].

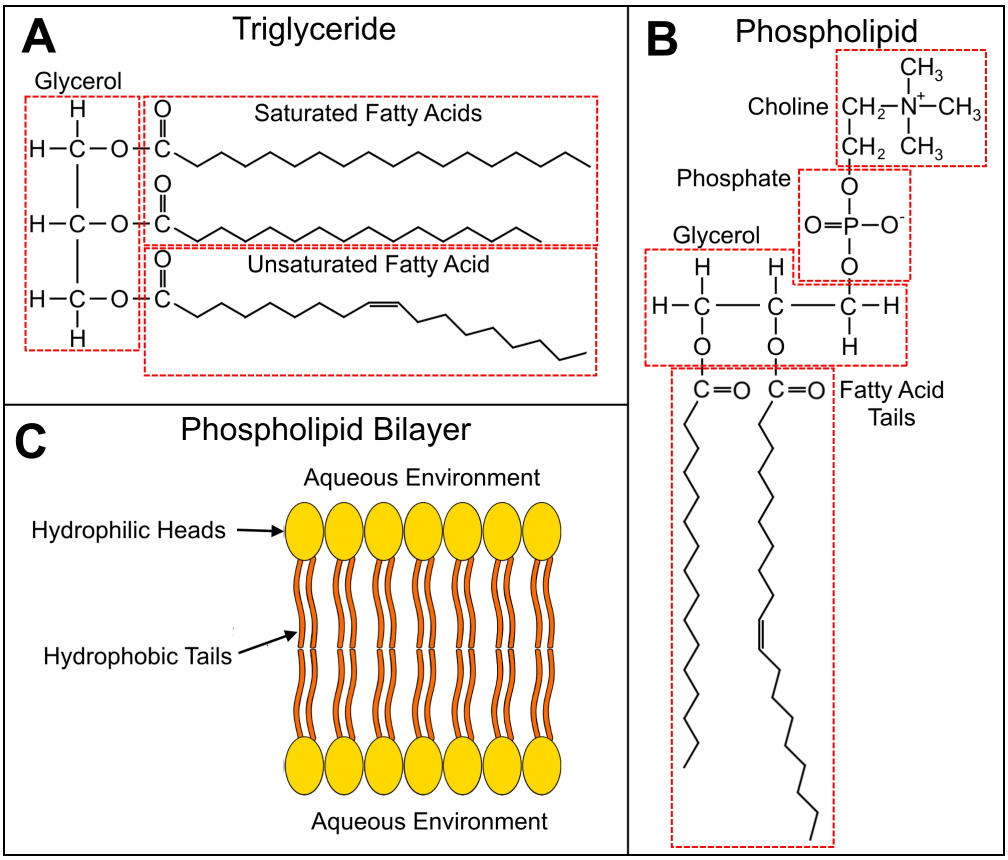

Figure 1.1: Structures of simple fatty acid containing lipids. A) A triglyceride molecule consisting of two saturated and one unsaturated fatty acid chains linked by a glycerol molecule. B) Typical phospholipid with a choline head linked to a phosphate group, a glycerol group and two fatty acid chain tails. The choline head is interchangeable with a number of different head molecules and the lengths and saturation of the fatty acid chains may vary. C) Phospholipid bilayer with hydrophilic heads on the outside and hydrophobic tails on the inside.

Eicosanoids are derived from the 20-carbon fatty acid arachidonic acid and include prostaglandins and leukotrienes which are used for cell signalling (Figure 1.2.B). For a full review of Eicosanoids and their role in cancer, see Wang and Dubois [16].

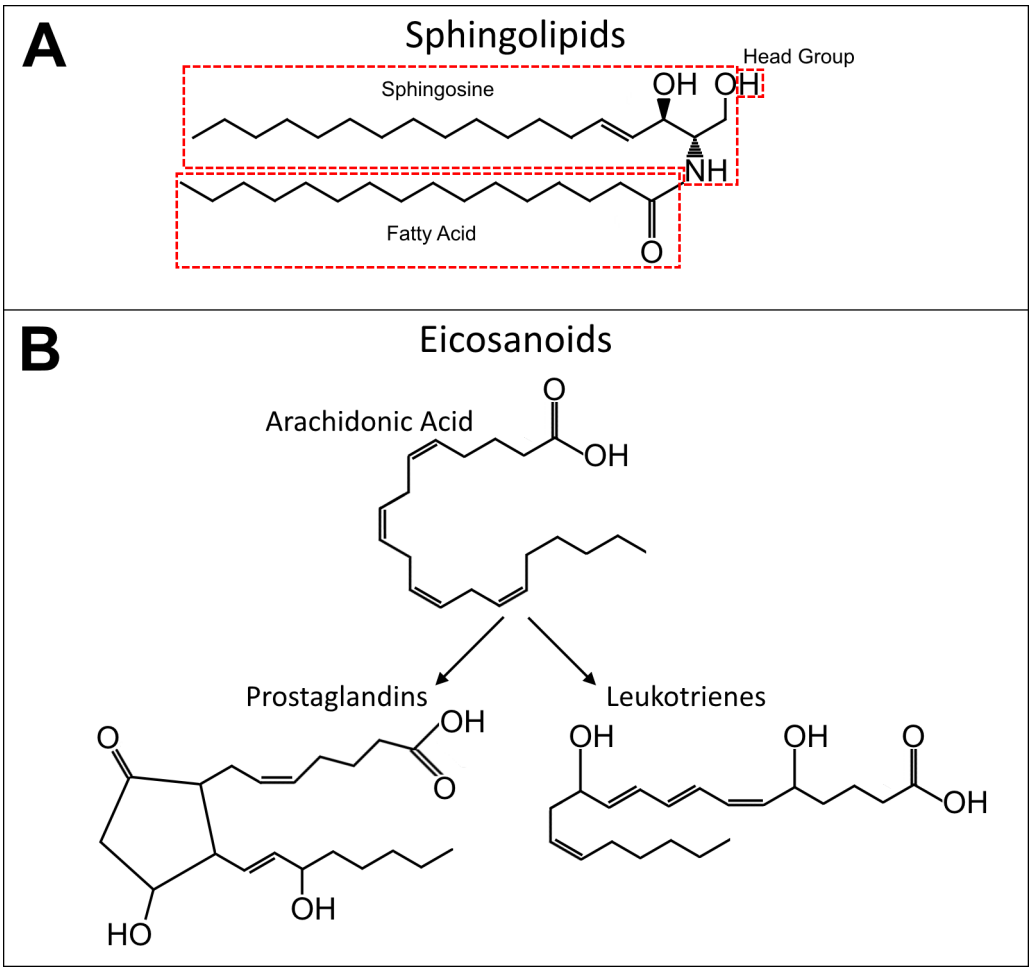

Figure 1.2: Other fatty acid containing lipids. A) Simple sphingolipid consisting of a sphingosine chain, a fatty acid chain and a Hydrogen head group. B) Arachidonic Acid is the precursor molecule to the eicosanoid family of lipids which include prostaglandins and leukotrienes.

1.1.2 Metabolic Changes in Cancerous Cells

Cancerous cells undergo a metabolic transformation, leading to an increased rate of glycolysis and lactic acid production in aerobic conditions. This is known as the Warburg effect [17,18]. As a consequence of the increased rate of glycolysis, there is also an upregulation of the Pentose Phosphate Pathway, which uses glucose-6-phosphate, an intermediate of glycolysis, to produce precursors for ribonucleotides [19].

The reduction of Nicotinamide Adenine Dinucleotide Phosphate ($NADP^+$ to NADPH) is required during several steps of this pathway, and the NADPH produced can go on to be oxidised again during fatty acid synthesis. For a full review of the role of the Pentose Phosphate Pathway in cancer see Patra and Hay [20].

An additional consequence of the Warburg effect is the upregulation of *de novo* lipid synthesis [1]. Typically, healthy cells do not produce their own lipids in this way, instead acquiring fatty acids and lipoproteins from the bloodstream [21]. In cancerous cells, citrate from the Kreb's cycle is converted to Acetyl-CoA, which can in turn be converted to Malonyl-CoA. Acetyl-CoA and Malonyl-CoA are then repeatedly condensed by Fatty Acid Synthase (FASN) to form palmitate, a 16-carbon saturated fatty acid [22] (Figure 1.3). This condensation requires NAPDH to act as a reducing agent. Palmitate produced in this process can then be further elongated and desaturated to produce a variety of fatty acids. These fatty acids can then be converted into various triglycerides, phospholipids, eicosanoids and sphingolipids (Figure1.3). Lipid synthesis is regulated by Sterol Regulatory Element Binding Proteins (SREBPs), a family of transcription factors. Under normal conditions, SREBPs are inactive and associated with SREBP-Cleavage Activating Proteins (SCAPs) in the endoplasmic reticulum. When there is a depletion of sterols, the SREBP-SCAP complex is translocated to the Golgi apparatus, where it is cleaved by the proteases SP1 and SP2. This releases an active form of the SREBP, which translocates to the nucleus and activates genes for various enzymes involved in lipid synthesis, including FASN [13].

1.1.3 Roles of Lipids in Cancer

Due to their structural function in membranes, a plentiful supply of lipids is essential for the rapid proliferation of cancer cells. Additionally, lipids play important roles in cell signalling to promote the proliferation, migration and survival of cancer cells [22]. Lysophosphatidic Acid (LPA), a simple phospholipid, has been linked to the progression of cancer due to its effects on cell proliferation, migration and survival (Reviewed in full by Mills and Moolenaar [2]). LPA binds to a number of G-protein-coupled receptors, including those coupled to G_i and $G_{12/13}$.

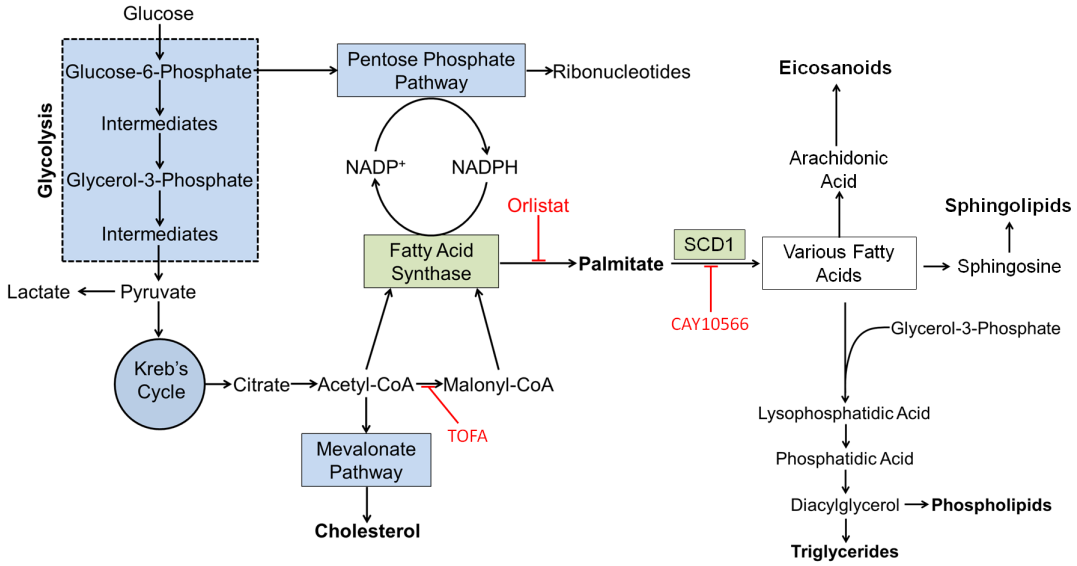

Figure 1.3: Simplified *de novo* lipid synthesis pathway. Glucose is converted to pyruvate by glycolysis, which is then converted to both Acetyl-CoA and Malonyl-CoA following the Kreb's cycle. These two molecules are then converted to palmitate by FASN, which is then desaturated to form a variety of fatty acids by SCD1. These fatty acids are then converted into phospholipids, triglycerides, sphingolipids and eicosanoids. Glucose-6-Phosphate from glycolysis is used in the pentose phosphate pathway to form ribonucleotides. During this process, NADP+ is converted to NADPH, which is used by FASN in the synthesis of palmitate. Another glycolysis intermediate, Glycerol-3-Phosphate is used in the synthesis of phospholipids and triclycerides. The drugs TOFA, Orlistat and CAY10566 are shown to inhibit various stages of the pathway.

Activation of G_i leads to stimulation of the mitogen-activated protein kinase pathway, leading to cell proliferation [23]; activation of the Akt pathway, which suppresses apoptosis leading to increased cell survival [24]; and activation of RAC, leading to lamellipodium extension on the leading edge of the cell [25]. Activation of $G_{12/13}$ leads to contraction of the cytoskeleton through activation of RHOA, which acts in combination with the lamellipodium extension caused by RAC to drive cell migration [25].

Sphingosine-1-Phosphate (S1P), a sphingolipid, has been found to promote survival proliferation, migration and angiogenesis in cancer (Reviewed by Pyne and Pyne [3]). As with LPA, S1P promotes proliferation and migration by binding to G-protein coupled receptors [26].

S1P can be converted to and from ceramide, which is pro-apoptotic. The conversion of ceramide to S1P therefore promotes cell survival by reducing ceramide levels [27]. S1P released from cancerous cells can also promote angiogenesis by binding to receptors on endothelial cells [28].

Prostaglandin E_2 (PGE_2) is an eicosanoid that is important for signalling in cancer. Secreted PGE_2 has been shown to stimulate endothelial cell proliferation and tube formation, leading to angiogenesis. Additionally, PGE_2 can bind to G-protein coupled receptors on cancerous cells, leading to the production of other pro-angiogenic factors [29]. PGE_2 has also been shown to promote cell proliferation by activating the Erk pathway. In addition, cells treated with PGE_2 to induce the Erk pathway have been found to be resistant to epidermal growth factor receptor inhibitors [4]. PGE_2 is also an immunosuppressor which inhibits the activity of cytotoxic T-cells both directly by upregulating CD94 and NKG2A complexes [30], and indirectly by downregulating antigen presentation on cancerous cells and inhibiting the maturation of dendritic cells [31].

Phosphotidylethanolamine (PE) is a phospholipid that can initiate autophagy by binding to autophagy-related protein 8 (ATG8) [32]. Autophagy is the process by which cells degrade and recycle defective proteins and organelles, usually in response to nutrient depletion. Autophagy has been linked to cancer cell survival as it provides an additional energy source which counteracts both nutrient deficiencies in the tumour microenvironment, and the increased metabolic demands of cancerous cells. For a full review of autophagy in cancer, see White 2015 [33].

1.1.4 Drugs Inhibiting the Lipid Synthesis Pathway

Due to the upregulation of lipid synthesis in cancerous cells and the vital roles that they play in cancer proliferation, migration and survival, drugs inhibiting stages of the lipid synthesis pathway are a current research interest in the search for new cancer therapies [34].

Orlistat is one such drug. Originally developed to treat obesity by inhibiting lipases which break down triglycerides in the intestine [35], orlistat has also found to be an inhibitor of FASN, an important enzyme in lipid synthesis (Figure 1.3) [5]. Kridel *et al.* [5] demonstrated that Orlistat can inhibit cancer cell proliferation and induce apoptosis *in vitro* in a range of different cell lines. Additionally, they showed orlistat treatment resulted in a reduction in tumour growth *in vivo* in a murine model using PC3 cells. Orlistat was also shown by Browne, Hindmarsh and Smith [36] to have an anti-angiogenic effect on ex vivo human placental tissue. Yang *et al.* [37] used a proteomic approach to identify additional targets of Orlistat. From this study, 8 additional proteins were identified as targets for orlistat, with functions including protein synthesis, glycolysis, cell division and stress response. These proteins are likely to be off-targets for orlistat, with the potential to cause side effects, however it is possible that some of them may aid in orlistat's anti-cancer effects by mechanisms currently undiscovered. Other FASN inhibitors include cerulenin and C75. In two studies, Pizer *et al.* [6,7] investigated the effects of both of these inhibitors on xenograft tumour models in mice. In the first of these studies, cerulenin was to treat tumours of the multiple drug-resistant ovarian cancer cell line OVCAR3. A significant delay in disease progression was observed when the mice were treated with cerulenin early on [6]. In the second study, C75 was found to inhibit tumour growth in breast cancer cell line MCF7 xenografted mice without comparable toxicity in healthy tissues [7]. Cerulenin has also been shown by Fang and Shen [38] to induce apoptosis in hepatic cancer cells both *in vitro* and *in vivo*, while Murata *et al.* [39] showed that cerulenin can prevent the development of liver metasteses from colon cancer in mice. C75 has been shown to enhance the efficacy of radiotherapy in treating prostate cancer cells *in vitro* using both monolayer and spheroid cultures [40].

Stearoyl-CoA desaturase 1 (SCD1) is an enzyme that promotes the conversion of palmitate to monounsaturated fatty acids in the lipid synthesis pathway [22]. CAY10566 is an inhibitor of SCD1 which was used by Mohammadzadeh *et al.* [8] to alter the lipid composition of breast cancer explants.

While this study found no evidence to suggest that CAY10566 is cytotoxic towards cancer cells, the activity of SCD1 was significantly ($P<0.05$) reduced when treated with 1 µM CAY10566 for 48 hours. The level of inhibition was found to be greater in cancerous explants than in healthy tissues and increased the concentration of saturated fatty acids in the cancerous tissue only.

5-(Tetradecyloxy)-2-furoic acid (TOFA) is an inhibitor of acetyl CoA-Carboxylase, an enzyme which converts acetyl CoA to malonyl CoA prior to the synthesis of palmitate by FASN [41]. TOFA was found by Wang *et al.* [9] to reduce fatty acid synthesis and induce cell death in lung and colon cancer cell lines. The cytotoxic effects of TOFA on these cells was found to be cancelled out by the addition of palmitate.

1.2 Raman Spectroscopy

Raman spectroscopy is an analytical technique used to probe the chemical properties of a sample. This section will discuss the physics behind the technique, Coherent Anti-Stokes Raman Spectroscopy (CARS) and how these techniques can be used to detect and measure lipids.

1.2.1 The Physics of Raman Spectroscopy

Raman Scattering is the inelastic scattering of photons incident on matter [42]. In the vast majority of cases, light incident on matter will scatter elastically, i.e. without losing or gaining any energy. This is called Rayleigh scattering (Figure 1.4) [43]. In Raman scattering, a small amount of energy is transferred between the photon and the molecule. The energy of the photon is directly related to its wavelength by the equation:

$$E = \frac{hc}{\lambda} \tag{1.1}$$

where E is energy, h is Planck's constant c is the velocity of light and λ is the wavelength. As a result, this small energy transfer results in a change in wavelength for the scattered photon. The amount of energy difference is dependent on the vibrational energy band structures of the molecule.

This means that different atoms or molecules will scatter the photons with a unique spectroscopic 'fingerprint' [44, 45]. As a result, Raman scattering based spectroscopy has become a common technique for chemical analysis in a wide variety of applications such as detecting impurities in semiconductors [46], analysis of proteins and peptides [47] and the structural characterisation of graphite based materials [48].

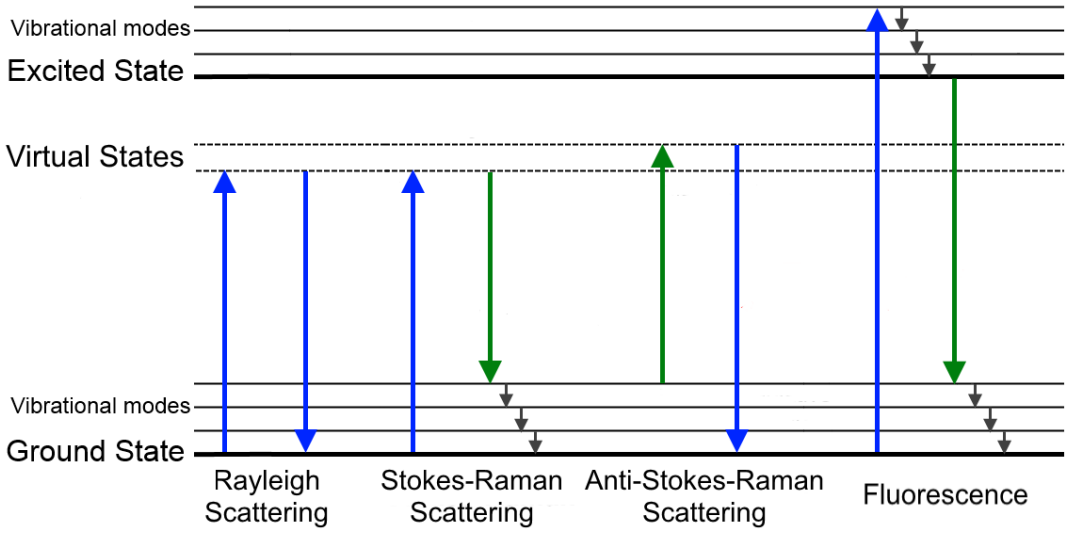

Figure 1.4: Jablonski energy level diagrams of Rayleigh scattering, Stokes-Raman Scattering, Anti-Stokes-Raman Scattering and Fluoreschence.

Raman scattering events can be categorised as being either Stokes or anti-Stokes. In Stokes Raman scattering, the molecule starts in the lowest vibrational mode of its ground energy state. A photon then interacts with the molecule, raising its energy to a temporary 'virtual energy level', before dropping back down to one of the vibrational modes of the ground state. This leads to a loss in the photon's energy and therefore an increase in its wavelength. In Anti-Stokes Raman Scattering, the molecule starts in one of the upper vibrational modes of its ground state. When the photon interacts, the molecule is again raised to a temporary virtual energy level before dropping down to the lowest vibrational mode of the ground state. The photon gains the energy lost from the molecule, leading to a decrease in its wavelength (Figure 1.4) [43].

Raman scattering differs from fluorescence as the molecule is only raised to a virtual energy level. In fluorescence the photon is completely absorbed by the molecule, which is raised to an upper energy level. The photon is then re-emitted at a longer wavelength when the molecule drops back down to its ground state [49]. The key difference between fluorescence and Raman is that the photon is not absorbed by the molecule during scattering events.

The vibrational modes of a molecule correspond to the different ways in which the atoms can vibrate relative to one another. In a simple diatomic molecule, only one mode is available, which is a simple stretching of the bond. This stretching can be described simply by Hooke's law:

$$\nu = \frac{1}{2\pi c}\sqrt{\frac{K}{\mu}} \tag{1.2}$$

where ν is the vibrational frequency, K is the force constant and μ is the reduced mass of the two atoms in the molecule [43].

More complicated molecules will have a higher number of possible vibrational modes equal to 3N - 6, where N is the number of atoms in the molecule. This is easily visualised in a simple triatomic molecule, which will have three possible vibrational modes corresponding to symmetrical stretches, bending and asymmetrical stretches (figure 1.5) [43].

The polarisation of the incident photons can also have an impact on the intensity of Raman scattering in crystalline samples depending on the direction of the polarisation in relation to the molecular axes [43]. In this thesis, Raman spectroscopy is used to probe biomolecules which are orientated in somewhat random directions, and such this effect is not of great impact. Polarisation of the scattered photons can also be affected by certain vibrational modes. Molecules undergoing a symmetric vibration do not tend to change the polarisation of the scattered photons, however asymmetric vibrations can alter the direction of polarisation.

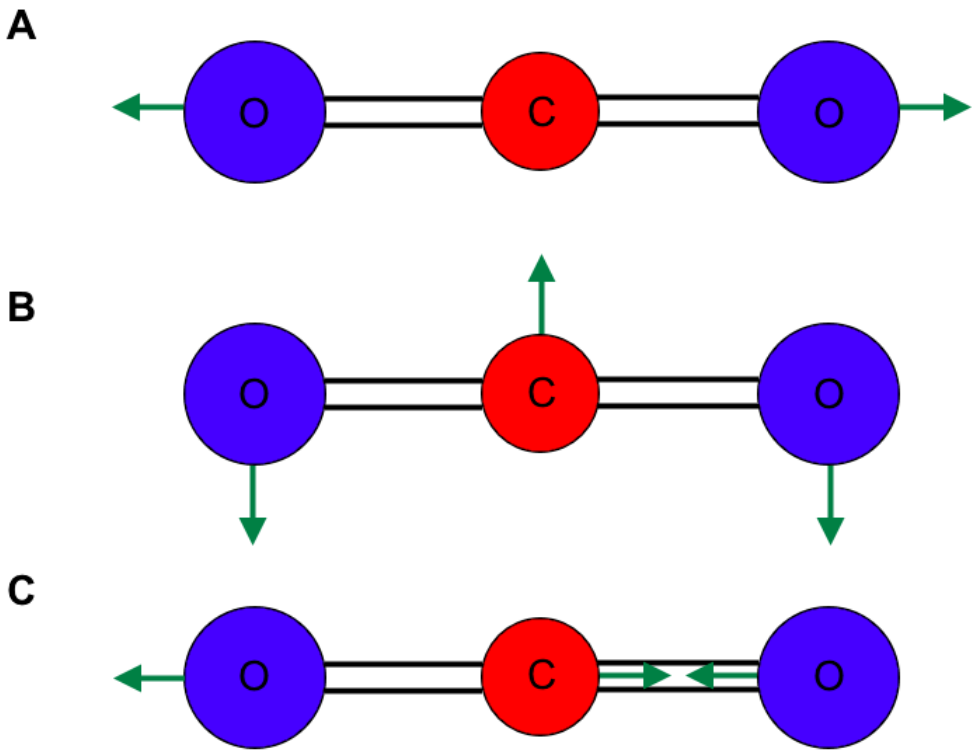

Figure 1.5: Vibrational modes in a CO_2 molecule. A) symmetric stretching, B) bending and C) asymmetric stretching.

A detailed mathematical description of this effect can be found in textbooks such as E. Smith's "Modern Raman Spectroscopy - A Practical Approach" [43] and is not required here to understand the content of this thesis.

1.2.2 Raman Spectroscopy as an Imaging Technique

Raman spectroscopy can be employed as an imaging technique by combining a Raman spectrometer with a scanning confocal microscope. By taking a spectrum of a sample at many points within a sample, a heatmap image of particular spectral peaks can be constructed. This allows for similar images to fluorescence to be obtained without the need for any dyes to be added to the sample. For example, Uzunbajakava *et al.* [50] used label-free confocal Raman imaging to produce maps of the protein and nucleic acid distributions in apoptotic cells.

These images were scanned in 250 nm steps and were able to show the presence of RNA in the cell nucleus for the first time by Raman spectroscopy.

Often in biological applications, label-free Raman spectroscopy may not be sensitive or selective enough to image specific molecules within a sample. Surface Enhanced Raman Spectroscopy (SERS) is a technique in which the analyte molecules are adsorbed to a metal surface. The incident photons excite localised surface plasmons on the metal surface creating localised electric fields which provide an amplifying effect to the scattered photons [51]. Metal nanoparticles are often used for this purpose. For example, colloidal gold nanoparticles were used by Kneipp *et al.* [52] to probe the chemical composition of live endothelial cells. Cells containing these nanoparticles were reported to show clearly defined Raman spectra with peaks corresponding to many of the different molecules found within the cell. By scanning the cells with a lateral resolution of 1 µm and taking a Raman spectrum at each point, intensity maps corresponding to the peaks associated with different molecules were created. From electron micrographs taken of the samples, it was reported that the nanoparticles had formed large aggregates within the cells. These nanoparticle aggregates were not homogenously distributed throughout the cells, leading to a greater degree of enhancement to the Raman signal in some regions of the cells, and barely any enhancement in others. While certain molecules such as DNA and phenylalanine were identified within the cells, the maps of these molecules are inaccurate due to the inhomogeneity of the nanoparticles. In order for this approach to be an accurate method of probing the molecular constituents of cells, the nanoparticles would have to be evenly distributed throughout the cells, leading to an equal amount of enhancement in all regions.

A more refined method of using nanoparticles for SERS analysis in biological applications is to target them to specific biomarkers. The metal nanoparticles can be coated with a 'dye' or 'Raman reporter' molecule with a well-defined Raman spectrum and then functionalised with a specific biomolecule, such as an antibody or DNA, which will target the nanoparticles to a specific molecule within the cell.

The use of such SERS nanoparticle labels has been used both in and out of cells for applications such as DNA and protein detection assays [53, 54] and the detection of specific biomarkers in cancer cells [55].
While the use of SERS active nanotags removes the label-free advantage of Raman spectroscopy over techniques such as fluorescence, such an approach can be more sensitive and offers greater scope for multiplexing while imaging with a single wavelength [56].

1.2.3 Coherent Anti-Stokes Raman Spectroscopy

Coherent Anti-Stokes Raman Spectroscopy (CARS) is a non-linear imaging technique based on anti-Stokes Raman scattering. It requires a more complicated setup than Stokes Raman spectroscopy techniques, which typically require only a single laser, as the sample must already be in an upper vibrational mode of its ground state prior to photon scattering. To achieve this, two tunable lasers, called the 'pump' and the 'stokes' are used. The difference in energies between the photons of the pump and stokes lasers is tuned to be equal to the energy difference between the ground and an upper vibrational mode of the molecule. This leads to the molecule being in the excited vibrational state. A third laser known as the probe then interacts with the molecule, raising it to a virtual state which then collapses back to the ground state in an anti-Stokes transition. This process can be simplified by using only two lasers whereby the pump and probe lasers are the same, however three photons must be incident on the molecule at the same time. (Figure 1.6) [43].
Unlike 'ordinary' Raman spectroscopy whereby a full spectrum is obtained for each measurement, CARS does not produce a spectrum from the sample. Instead it is tunable to specific vibrational transitions and is able to rapidly image the intensity of Raman scattering events at a particular wavenumber in a similar manner to fluorescence when used in a confocal scanning methodology. This can be advantageous in applications requiring heatmaps of only a few known wavenumbers as methodologies taking full spectra at each point tend to be much slower, require more data processing and generate unnecessary data from uninteresting spectral regions.

CARS was used by Evans *et al.* [57] to image CH2 groups in live murinal tissue with subcellular spatial and 'video-rate' temporal resolution. Cheng *et al.* [58] used multiplexed CARS to image lipid vesicles in live cells and Okuno *et al.* [59] used CARS to produce molecular fingerprints of live cells.

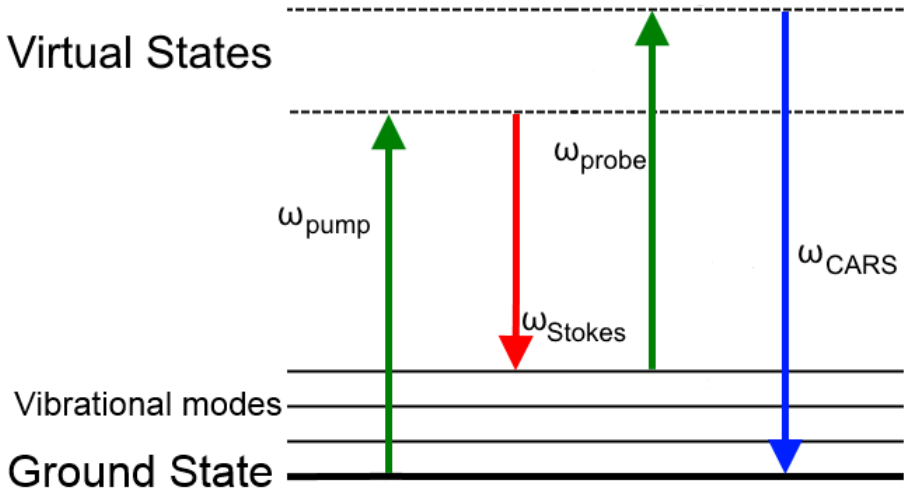

Figure 1.6: Jablonski energy level diagram for CARS transitions.

1.2.4 Lipid Imaging with Raman Spectroscopy

A number of studies have utilised Raman spectroscopy to image lipids.

Frank and McCreery [60] used Raman spectroscopy to compare normal and diseased human breast biopsy samples. The CH_2 stretching band at 1439 cm^{-1} was used as an indicator of the lipid to protein ratio. A reduction in the lipid content of samples with infiltrating ductal carcinoma was detected. This is likely due to the higher concentration of triglycerides found in normal breast tissues.

A more recent study into Raman imaging of human breast tissue explants was carried out by Abramczyk and Brozek-Pluska [61]. Information obtainable from Raman images of human breast ducts were found to be comparable to histologically stained samples.

By mapping the data with spectra for individual molecular components, the distribution of various biomolecules (including several lipids) could be seen. Palmitate, sphingomyelin and mammaglobin, a protein known to be overexpressed in breast cancer, were all identified as being present at high levels within cancerous cells that had infiltrated the lumen of a duct.

Sweetenham and Notingher [62] used a simultaneous combination of Raman spectroscopy and atomic force microscopy to image artificial supported lipid bilayers on a sapphire substrate. Although the system used was not sensitive enough to detect single lipid bilayers with Raman spectroscopy, clear spectra were obtained from multi-layered structures and two different types of lipid could be discriminated by the presence or absence of a peak at 1641 cm^{-1}.

Krafft *et al.* [63] recorded the Raman spectra of 12 different lipids found within brain tissue, including cholesterol, phosphatidic acid, phosphatidyl-choline and sphingomyelin. 'High wavenumber' Raman spectroscopy revealed a number of peaks in the 2700-3500 cm^{-1} region, including those originating from CH_2 stretching at 2850 cm^{-1} and CH_3 stretching at 2935 cm^{-1}. 'Low wavenumber' peaks between 400-1000 cm^{-1} were also identified for each of the lipids and were found to be better for discriminating between different lipid types, however the intensities are much weaker than those in the high wavenumber region, making them much harder to detect in biological samples. It was concluded that high wavenumber Raman spectroscopy could be a useful tool for determining the overall lipid concentration of biological samples.

Jamieson *et al.* [10] used high wavenumber Raman spectroscopy to investigate the effects of different drugs on the lipid composition of cancerous cells. Lipid content was estimated by calculating the ratio between the intensities of peaks at 2851 cm^{-1} (attributed to C-H stretches in CH_2 groups in the fatty acid chains of lipids) and 2933 cm^{-1} (attributed to C-H stretches in CH_3 groups, abundant in protein polypeptide chains). The drugs tested included the FASN inhibitor orlistat, SCD1 inhibitor CAY10566 and acetyl CoA-Carboxylase inhibitor TOFA as well as two positive control drugs cyclosporin and propranolol, both of which promote lipid synthesis. Counter-intuitively, cancerous PC3 cells showed an increase in lipid composition when treated with orlistat.

This is hypothesised to be due to either a stress response from the cells causing them to accumulate lipids from surrounding media, or due to continued elongation of fatty acid chains leading to a greater response at 2851 cm^{-1}. TOFA was shown to reduce the lipid content of PC3 cells, whereas no significant difference in lipid content was found for cells treated with CAY10566. This paper is the foundation for this thesis. While the work here was performed on traditional platforms, the work in this thesis aims to develop a convenient microfluidic platform in order to miniaturise studies into lipid analysis.

Outside of human biology, Raman spectroscopy has been used to measure intracellular lipids in micro-algae under nitrogen stress [64] and to map lipid-enriched organelles in bacteria [65].

1.3 Microfluidics

Microfluidic, 'lab-on-a-chip', devices are becoming increasingly popular as they provide novel platforms for many biological applications (Reviewed by Weibel and Whitesides 2006 [66]). Such devices are used to process fluids and biological materials through micrometre-scale channels. Advantages of such platforms in comparison to conventional platforms can include: higher throughputs, use of a smaller amount of reagents and generation of less waste leading to cheaper assays, 3D cellular models instead of 2D models and the ability to easily create concentration gradients of drugs and other small molecules. This section discusses the methods and materials for creating microfluidic systems, principals and practicalities of operating microfluidic systems and example applications of microfluidics used for drug screening.

1.3.1 Materials and Manufacture of Microfluidic Devices

A common method for the manufacture of microfluidic devices is soft lithography using the silicone elastomer polydimethylsiloxane (PDMS) [67–80] (Processes reviewed by [81]). PDMS has many desirable properties for microfluidic applications including optical clarity, biocompatibility and low cost.

It is usually supplied as a two part liquid prepolymer which when mixed and heated forms a solid polymer. Micropatterns, such as microfluidic channels, can be made on the surface of PDMS by curing the liquid prepolymer on top of a reusable master template. This creates a series of grooved features on one surface of the PDMS, which can be encapsulated to form enclosed channels by bonding the PDMS to a substrate (usually glass or another PDMS layer). The cost, speed, simplicity and reproducibility of this method make it a desirable technique for rapid prototyping of microfluidic devices.

The master template for casting PDMS is often made by photolithography on a silicon wafer [82]. In this process, UV radiation is used to cure a photoresist such as SU-8, onto a substrate such as a silicon wafer. A photomask containing a 2D pattern can be placed between the light source and the photoresist in order to create features such as microchannels (figure 1.7.A). This is then treated with a solvent to remove any uncured photoresist, leaving behind the features (figure 1.7.B-C). The height of the features can be controlled by spin coating onto the substrate at different speeds.

Despite its popularity, PDMS is not without its disadvantages. Due to its hydrophobic nature, some molecules and proteins are prone to adsorbing on to the channel surfaces or absorbing into the bulk PDMS [83, 84]. This could potentially limit the accuracy of the concentrations of drugs and other molecules being used in microfluidic based assays. Additionally, the flexibility of PDMS limits its use in high pressure applications as the microfluidic channels are deformable (alternative materials for high pressure applications reviewed by Sollier *et al.* [85]).

Alternative materials that have been used for microfluidic devices include: polyurethanes [83, 84], polymethyl methacrylate (PMMA) [86], glass [87] and Teflons [88]. Teflon was selected as a material to create microfluidic devices in this project as described in section 3

Teflons are a class of polymer based on fluorocarbon chains and have been used in microfluidics to synthesise peptides [89], perform viscocity measurement for petrochemical mixtures [90] and for electrochemical sensing [91]. Teflon microfluidic chips are desirable in such applications due to their resistance to strong solvents, where other materials such as PDMS might degrade.

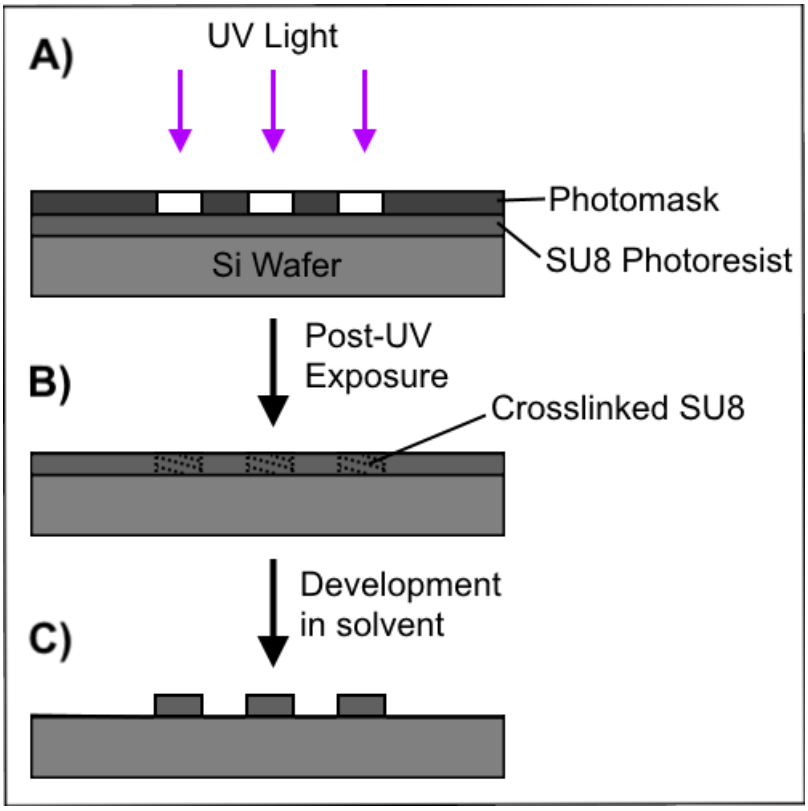

Figure 1.7: Basic photolithography concepts using SU8 on a silicon wafer. A) A layer of SU8 photoresist, spin-coated on a silicon wafer, is exposed to UV light through a patterned photomask. B) The photomask is removed and the regions of SU8 exposed to the UV light have crosslinked (shaded sections). This is then developed with a solvent to dissolve the un-crosslinked SU8. C) The wafer is now micropatterned with SU8 and can be used as a master for PDMS soft-lithography.

Polytetrafluoroethylene (PTFE) is the most commonly used teflon and consists of simple fluorocarbon chains with the chemical formula $[CF_2\text{-}CF_2]_n$. However, PTFE is not suitable for many microfluidic applications because it is opaque and microfluidics often uses microscopy as an analysis tool. Ren *et al.* [88] first described the use of the optically clear teflons perfluoroalkoxy alkane (PFLA) and fluorinated ethylene propylene (FEP) to create microfluidic devices. These devices were created by hot embossing, a technique whereby a polymer is heated to its glass transition temperature and pressed against a stamp to micropattern the features.

This was done by heating 0.1 mm thick teflon sheets to either 275°C (PFLA) or 265°C (FEP) and applying approximately 10 kPa of pressure for 2 minutes, using a specially prepared PDMS stamp. The PDMS stamp was cured with a 5:1 prepolymer to curing agent weight ratio as opposed to the standard ratio of 10:1 in order to make it stronger, and was treated thermally at 250°C for 1 hour to prevent outgassing during the hot embossing process. Micropatterned teflon layers were then thermally bonded at 260°C to encapsulate the device channels. This had to be done under very gentle pressure, using the thermal expansion of the teflon layers during heating, to prevent deformation of the device features. Devices bonded with too much pressure experienced collapsing of the channels, while devices bonded at lower temperatures weren't fully sealed. Teflon devices were found to be suitable for culturing cells for 120 hours, despite the apparent low gas permeability, and pneumatically controlled valves were successfully implemented into the devices. While this paper shows promising results for Teflon microdevices, there is no discussion of bonding strength or bond stability. Additionally, the paper claims that it is possible to hot emboss features down to 150 nm in diameter, however does not discuss the height of these features, a factor that will severely impact on the possible lateral resolution [92].

PDMS has also been used as a stamp for hot embossing PMMA [93]. In this instance the usual 10:1 prepolymer to curing agent ratio was used and the stamp was not heat treated prior to use. The embossing of the PMMA took place at 130°C, which is significantly lower than the temperatures used by Ren *et al.* as PMMA has a lower glass transition temperature than teflons. This is also lower than 150°C, the temperature at which PDMS will start to outgass according to Ren *et al.* [88], hence why the heat treatment of the stamp was not necessary and why a harder material was not required.

Teflon microfluidic devices have been used to synthesise peptides [89], viscocity measurement for petrochemical mixtures [90] and for electrochemical sensing [91]. Teflon microfluidic chips are desirable in such applications due to their resistance to strong solvents, where other materials such as PDMS might degrade.

There are limited examples of Teflon microfluidic devices being used in biological applications in the literature, however Shen, Xiong and Wu [94] reported coating FEP devices with a polydopamine coating, allowing for immunoassays to be performed.

1.3.2 Operation of Microfluidic Devices

A number of 'world to chip' interfacing methods exist for operating microfluidic devices. A common method of controlling devices is to connect inlet and outlet ports to syringe pumps with tubing (figure 1.8.A). This method is popular as it allows for precise control of flow rates within the device channels, which is essential for many applications [95].

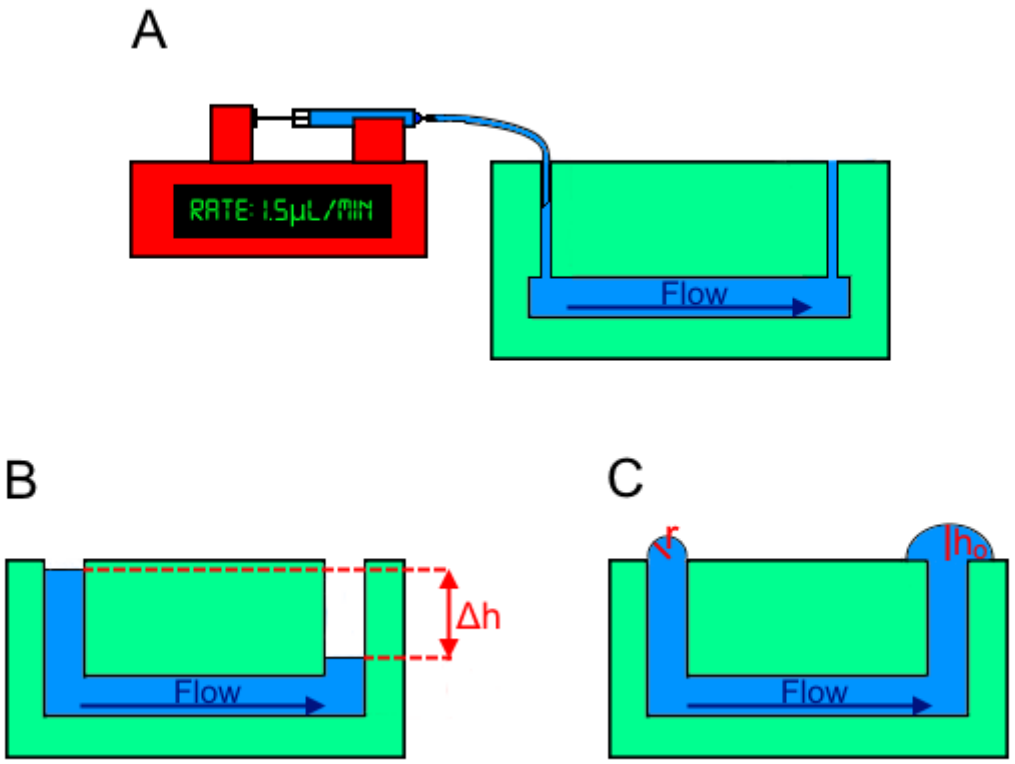

Figure 1.8: Common interfacing methods for microfluidics. A) Liquid is flown through the device at a constant rate by a syringe pump. B) Hydrostatic pressure drives the flow through a device from a filled well to an empty one. C) Surface pressure causes a flow from a small inlet droplet to a larger outlet reservoir droplet.

Flow within a device is analogous to current within an electrical circuit (Reviewed by Oh *et al.* [96]). Whereas in electronics, many principles are derived from Ohm's law:

$$U = IR \tag{1.3}$$

where U is voltage, I is current and R is resistance, in microfluidics the analogous equation is:

$$\Delta P = QR_{\mathrm{h}} \tag{1.4}$$

where ΔP is the pressure across the device, Q is the flow rate and R_{h} is hydraulic resistance. A number of principles from electronics can be used in microfluidics to predict flow within a device, including Kirchhoff's law and adding resistances in both parallel and series [96]. The hydraulic resistance of a channel is dependent on its geometry. For a channel with a rectangular cross section the resistance is often approximated to:

$$R_{\mathrm{h}} = \frac{12\mu L}{wh^3}\left(1 - \frac{192h}{\pi^5 w}\right)^{-1} \tag{1.5}$$

where h is the channel height, w the width and L the length [97]. The surface roughness of the channel can also impact the flow rate in a microfluidic device, particularly at the channel surfaces, and this can be incorporated into a more complex mathematical model [98], however this is not required to understand the work presented in this thesis. Syringe pumps can become impractical and costly when a device has a large number of independently addressable ports leading to a large number of syringe pumps needed and a large amount of space within a laboratory.

For simpler devices where precisely maintained flow rates are not essential, passive methods may be more user friendly. A simple method is to use inlet/outlet wells large enough to pipette into directly in a hydrostatic pressure driven system (figure 1.8.B). By pipetting into an inlet well connected to a corresponding, empty outlet well, the liquid will be driven through the channel and into the outlet. As the volume of liquid in the inlet increases and the volume of the liquid in the outlet increases, the flow rate of the liquid will slow until both inlet and outlet wells are at the same level.

An inlet well driving flow in this way is analogous to a discharging capacitor in an electronic RC circuit. In electronics, the capacitance, C, is given by:

$$C = \frac{q}{U} \tag{1.6}$$

where q is the charge stored in the capacitor. The hydraulic equivalent is then:

$$C_{\mathrm{h}} = \frac{V}{\Delta P} \tag{1.7}$$

where C_{h} is the hydraulic capacitance, V is the volume of liquid that will be discharged during flow. If the outlet is infinitely large, then V and Δ P are simply the starting volume and pressure in the inlet well. The pressure, P, within the well is given by:

$$P = \rho g h \tag{1.8}$$

where ρ is the density of the liquid, g is acceleration due to gravity and h is the height of the liquid in the well. This can be related to the volume in the well using simple geometry. Assuming a cylindrical well, this becomes:

$$P = \rho g \frac{V}{\pi r^2} \tag{1.9}$$

where r is the well radius.

Current, I, and voltage in a simple RC circuit will both drop as the capacitor discharges. These can be calculated by the equations:

$$I(t) = I_0 e^{\frac{-t}{RC}} \tag{1.10}$$

$$U(t) = U_0 e^{\frac{-t}{RC}} \tag{1.11}$$

where I_0 and U_0 are the initial current and initial voltage respectively, and R is the electrical resistance of the circuit. Hydraulic equivalents are therefore:

$$Q(t) = Q_0 e^{\frac{-t}{R_\mathrm{h} C_\mathrm{h}}} \tag{1.12}$$

$$\Delta P(t) = \Delta P_0 e^{\frac{-t}{R_\mathrm{h} C_\mathrm{h}}} \tag{1.13}$$

For channels with outlet wells of a defined size, the filling of the outlet well as the inlet well discharges must be taken into account. The flow will stop when the well pressures are balanced, so it is necessary to calculate the volume that will have been discharged when the well pressures are balanced. Assuming that both inlet and outlet wells are the same radius, the pressures will be balanced when they contain the same volume. Defining $V_\mathrm{i}(t)$ as the inlet well volume and $V_\mathrm{o}(t)$ as the outlet well volume, the total volume that will be discharged is simply:

$$V = \frac{V_\mathrm{i}(0) - V_\mathrm{o}(0)}{2} \tag{1.14}$$

Substituting this into equation 1.7 gives the hydraulic capacitance in terms of easily calculable starting values:

$$C_\mathrm{h} = \frac{V_\mathrm{i}(0) - V_\mathrm{o}(0)}{2\Delta P(0)} \tag{1.15}$$

The starting volumes of each well should be inconsequential to the hydraulic capacitance, which is entirely dependent on the geometry of the device.

In order to calculate C_h in terms of geometry only, $\Delta P(0)$ can be substituted in terms of starting volumes from equation 1.9:

$$C_h = \frac{V_i(0) - V_o(0)}{\frac{2\rho g}{\pi r^2}(V_i(0) - V_o(0))} \tag{1.16}$$

This equation simplifies such that all volume terms cancel out, leaving an equation in terms of well radii only:

$$C_h = \frac{\pi r^2}{2\rho g} \tag{1.17}$$

Values for capacitance can then be substituted into equation 1.12 in order to predict the flow within such a device.

Equation 1.17 assumes that the inlet and outlet radii are identical. For cases where this is not true, the hydraulic capacitance can be calculated by the equation:

$$C_h = \frac{\pi {r_i}^2 {r_o}^2}{\rho g({r_i}^2 + {r_o}^2)} \tag{1.18}$$

A full derivation for this equation can be found in Appendix C.

Another passive pumping technique involves using the surface tension of a small droplet to drive the flow [99]. A small droplet is placed on the inlet port, and a larger reservoir droplet is placed at the outlet port (figure 1.8.C). Surface tension will create a pressure in the droplets given by the equation:

$$P = \frac{2\gamma}{r} \tag{1.19}$$

where γ is the surface tension of the liquid and r is the droplet radius. With a large enough outlet reservoir, the pressure created by surface tension becomes negligible, however hydrostatic pressure needs to be considered. Hydrostatic pressure can be ignored for the inlet droplet as it is considered to be negligible. The flow rate in the device is then:

$$Q = \frac{1}{R_h}\left(\frac{2\gamma}{r} - \rho g h_o\right) \tag{1.20}$$

where h_o is the height of the outlet reservoir droplet.

This technique carries the same complications as with hydrostatic pressure, whereby as the volume is depleted, the flow rate in the device will change. Additionally, due to the very small volumes used, the pumping droplet will be rapidly depleted. An advantage of this technique over hydrostatic pressure is that it does not require as large inlet ports in the device.

1.3.3 Microfluidic Drug Testing Platforms

One promising area in which microfluidics has been applied is for creating novel platforms for testing cellular responses to drugs and other chemicals (reviewed by Huang and Lee [100]). Such systems can offer a number of advantages over conventional *in vitro* methods, usually a monolayer culture in a multi-well plate or petri dish, such as constant perfusion of culture media, isolation of single cells, drug concentration gradients, 3D microenvironments, mimicking of *in vivo* conditions, and lower reagent/waste volumes. While many studies have seeded cells into microfluidic devices and allowed them to adhere to the bottom surface in monolayers [67, 68], several methods for capturing and isolating single cells within microfluidic devices have been developed (reviewed by Nilsson *et al.* [101]). The study of single cells is important for many applications as it allows for cell-to-cell variation to be investigated [102].

One such solution is to use an array of small U-shaped structures to act as single cell traps as they flow through a channel (figure 1.9.A) [103]. This requires sub-cellular feature resolution, which is easily achievable with PDMS and other materials common to microfluidics. Di Carlo, Aghdam and Lee [103] used a microfluidic device containing such traps to capture single cells for studying enzyme kinetics. For traps of 10 µm depth, a single-cell trapping efficiency of >50% was reported and the inhibition of carboxylesterases was successfully measured by addition of nordihydroguaiaretic acid. Similar single cell traps were used by Cunha-Matos *et al.* to monitor the cellular uptake of gold nanorods [104] and by Probst *et al.* to trap single, rapidly proliferating E. Coli cells while washing away descendent cells [105].

Another method for trapping single cells is to use an array of microwells within a microfluidic channel, each large enough to accommodate a single cell (figure 1.9.B).

Cells within a channel containing such traps will fall into them by gravity. Rettig and Folch [106] used such a system and reported up to 92% single-cell trap occupancy, while Chen *et al.* used aptamer-coated microwells to selectively capture single tumour cells [69].

Single cells have also been encapsulated in droplets using two-phase microfluidic systems (figure 1.9.C) [70], however, cells isolated in this way will be subject to a limited amount of nutrients and may not be suitable for long-term assays.

By isolating single cells as described above, their analysis becomes much simpler as cells can often group together in monolayer cultures.

When cells are cultured in a well plate or other such conventional platform, they

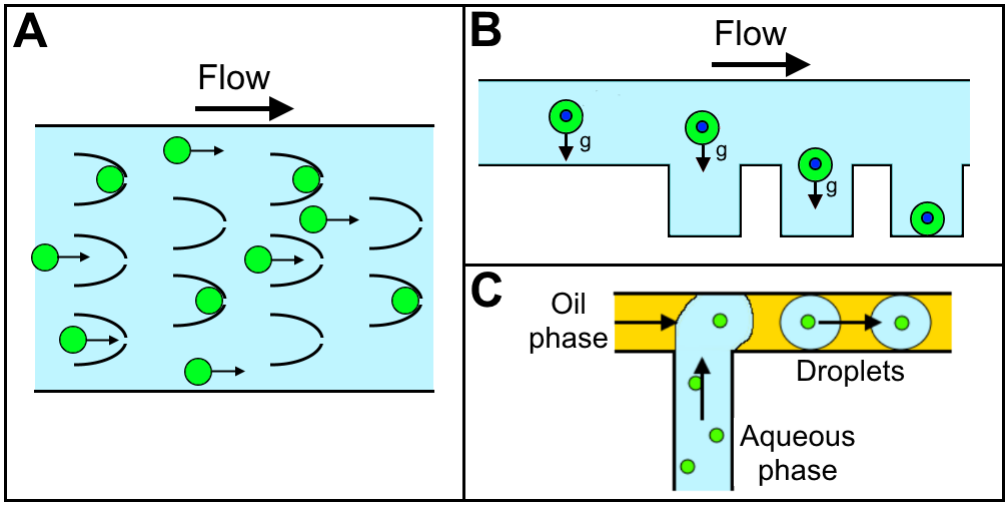

Figure 1.9: Methods for capturing single cells in microfluidic platforms. A) Single cells are trapped by U-shaped structures within a microfluidic channel. B) Cells drop into microwells while travelling through a channel. C) Single cells are captured in droplets in a two-phase microfluidic system.

are generally under 'static' conditions whereby culture media and drugs are delivered and removed intermittently. As a result, nutrients and drugs are depleted as the cells metabolise and waste products are not removed from the extracellular environment until the media is exchanged, leading to fluctuating culture conditions [107]. Even minor changes to the extracellular environment have been shown to impact on cell physiology [108].

When cells are cultured with constant perfusion of nutrients, the microenvironment can be stabilised, leading to consistent cell physiology (reviewed by Sittinger *et al.* [109]). Wu *et al.* [107] developed a microfluidic device for culturing chondrocytes under constant perfusion. This two-layer device consisted of five separate cell culture chambers in the bottom layer, connected to inlets and an outlet port via channels in the top layer. Chondrocytes were mixed with an agarose solution and pipetted into the culture chambers prior to bonding the two PDMS layers. This produced a 3D culture scaffold within each chamber, and the inlets were connected to medium-loaded syringes driven by a multi-channel syringe pump to provide constant perfusion of culture medium at 1 µL/hr.

Using conventional cell culture methods, concentration studies of drugs are usually performed in multi-well plates, with each well treated with a different concentration of drug. Microfluidic systems have been developed to instead supply a controllable concentration gradient across trapped cells in a high throughput manner.

One such device was developed by Kim *et al.* [110]. Cells were seeded onto a permeable membrane within the device through a top layer channel. Underneath the membrane was a gradient generating channel, where two laminar streams containing different concentrations of small molecules created a sharp concentration gradient at their interface (Figure 1.10.A.). Another approach is the so-called 'Christmas tree' gradient generator, first described by Dertinger *et al.* [111]. Such devices consist of two or three inlets at the top of the network which are repeatedly co-split at nodes into thin, serpentine channels where diffusion between the streams takes place. Each branch of the network contains an increased number of nodes, leading to an increased number of concentrations produced (figure 1.10.B.). At the end of these networks, the separated streams, each carrying a different concentration of molecules are often recombined into a wide channel in which cells may be seeded. This type of gradient generator was used by Wang *et al.* [67] with a series of cell culture chambers at the end of the final branch to study resistance of lung carcinoma cells to anti-cancer drugs.

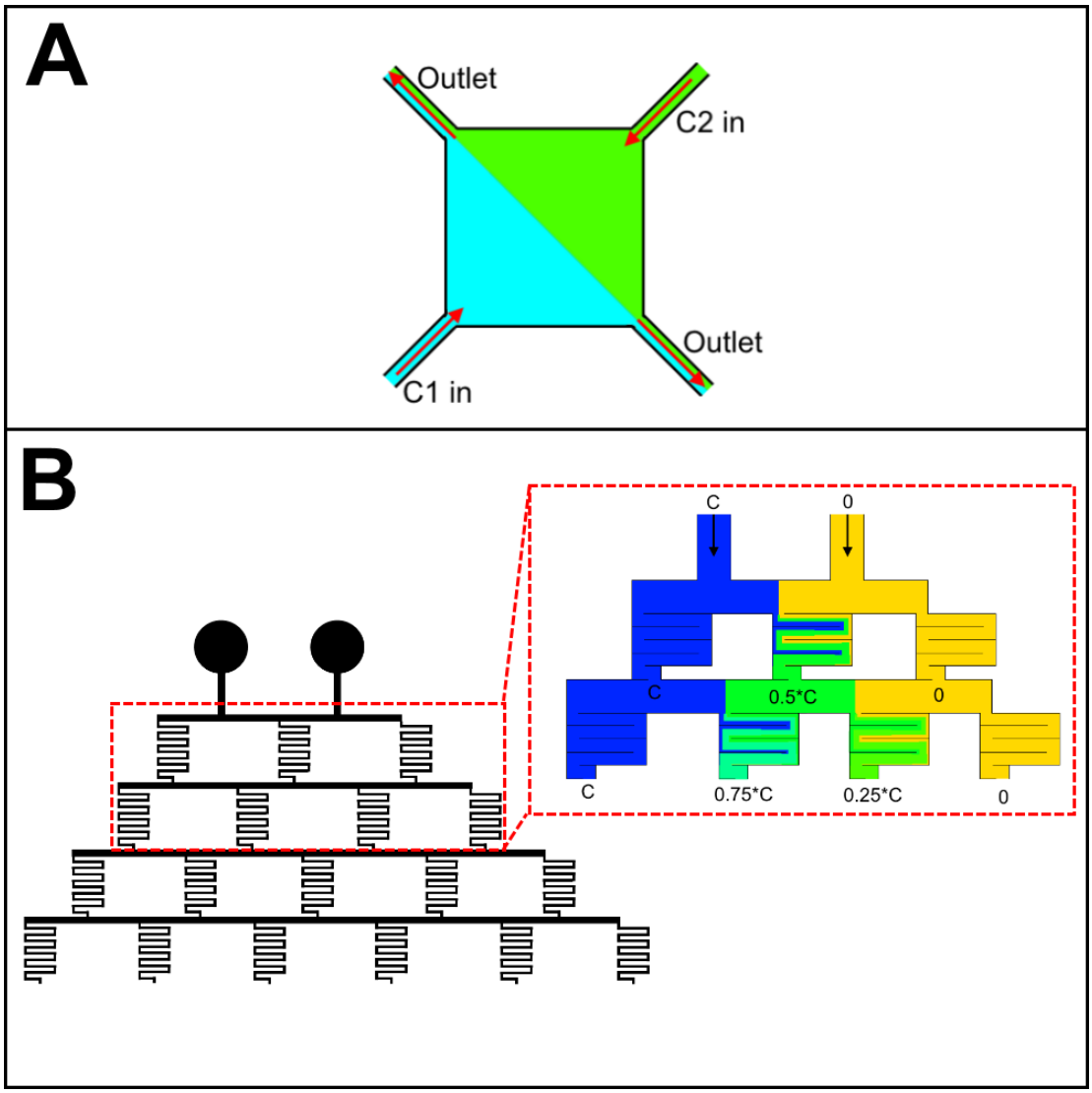

Figure 1.10: Microfluidic concentration gradient generation. A) Two opposing laminar streams of different concentrations meet in the middle of a square chamber, creating a sharp concentration gradient along the diagonal of the chamber. B) Schematic and principal behind the 'Christmas tree' concentration gradient generator. Four branches are shown in the schematic leading to six concentrations at the end. Insert shows the principal behind the structure whereby streams are mixed in small serpentine channels leading to different dilutions at each step. It is required that each pathway through the structure should have the same path length to ensure even dilutions.

In addition to single-cell analysis, microfluidic devices have also been used to create systems that are more representative of *in vivo* conditions. For example, microfluidic devices can provide a user-friendly solution to the creation of 3D spheroids, which are thought to be more representative of *in vivo* conditions than conventional 2D monolayers (reviewed by Fennema *et al.* [112]). Mulholland *et al.* [71] seeded cells into a microfluidic channel with large multi-cell wells along the bottom. Cells trapped in each well aggregated and formed spheroids within 48 hours. The channel containing the wells was linked to a gradient generator, and assays with the anti-cancer drug cisplatin were performed against a variety of cancerous cell types.

To further mimic *in vivo* conditions, Sin *et al.* [113] developed a microfluidic device consisting of three cell culture chambers interconnected by microchannels. Each chamber was used to culture different mammalian cells (lung, liver and "other") and the connecting channels circulated medium between the chambers to act as a mock circulatory system. The system also contained an integrated fluorescence-based oxygen sensor to monitor the oxygen content of the medium. A similar system was used by Viravaidya *et al.* [114], with an additional culture chamber for fat tissue, to measure the toxicity of naphthalene. The naphthalene was converted to 1,2-naphthalenediol and 1,2-naphthoquinone in the liver chamber and circulated to the lung chamber, where glutathione depletion was observed as a consequence.

Microfluidics has also been used for chemotaxis studies (reviewed by Wu, Wu and Lin [115]). One advantage of using microfluidics over traditional transwell assays is the ability to create and control more complicated chemical gradients. For example, Ricart *et al.* [116] generated competing chemokine gradients in a microfluidic device to investigate the migration of dendritic cells. In another study by Scherber *et al.* [117], used a microfluidic maze to show that epithelial cells could migrate through the shortest path towards a source of epithelial growth factor. Microfluidic devices have also been used for investigating signalling between neurons [72], simultaneous analysis of drug metabolites and cytotoxicity [73], and antigen detection assays [74].

A number of analysis solutions have been shown to be compatible with microfluidic systems. Most microfluidic materials, such as PDMS, PMMA, PFA and glass are optically clear, allowing for experiments to take place using optical microscopes to visualise the cells inside. Fluorescence microscopy is very commonly used with microfluidics, for example Rettig and Folch [106] imaged single cells treated with the fluorescent viability stains calcein and ethidium homodimer-1 (EthD) in microwells to show that over 99% of cells within the device remained viable after 30 minutes. Fluorescence has also been used in microfluidic systems to measure synaptic activity in neuronal networks [72], to measure enzymic activity [118], to monitor oxygen content of cell culture media [113] and for cell sorting [119].
Other analytical techniques used in combination with microfluidics have included Raman Spectroscopy (see section 1.3.4) infrared spectroscopy [120], chemiluminescence [121] and electrochemical sensing with integrated electrodes [122].

1.3.4 Raman Spectroscopy in Microfluidics

Raman spectroscopy has also been shown to be compatible with microfluidics. Many studies have utilised the on-chip mixing of nanoparticles with analytes for SERS analysis. For example Lee *et al.* [75] used a zigzag shaped microfluidic channel to mix malachite green molecules with silver nanoparticles. The malachite green adsorbed onto the nanoparticles and the concentration could be estimated from on-chip SERS analysis. A similar method was used by Yea *et al.* [76] to detect cyanide molecules in drinking water (figure 1.11.A). By mixing cyanide solutions with silver nanoparticles on-chip, the sensitivity of detection was reported to be enhanced by several orders of magnitude compared with standard techniques. Hoonejani *et al.* [78] used SERS to sequentially measure multiplexed biotags on polystyrene beads on a flow focusing microfluidic device (figure 1.11.B). From this different bead populations could be distinguished depending on their biotags. In another study, Zhang *et al.* [77] used gold nanorod SERS probes to monitor the interaction between fatty acid receptors of kidney cells and fatty acids on a microfluidic device with a gradient generator (figure 1.11.C).

From this a positive correlation between the fatty acid concentration and the SERS signal was reported, demonstrating potential for this approach at monitoring membrane receptor interactions. Willner *et al.* [79] encapsulated single prostate cancer cells in droplets and used SERS-active nanoparticles to measure the expression of glycans on their surface.

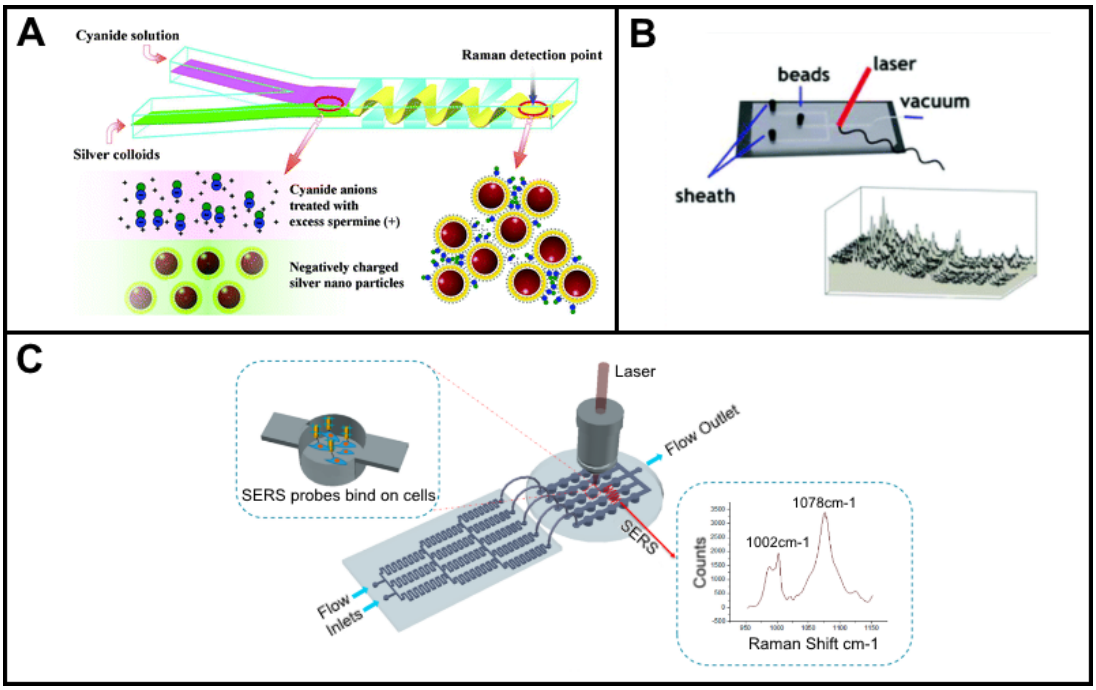

Figure 1.11: Microfluidic devices which utilised SERS as an analysis technique. A) Device used by Yea *et al.* [76] to detect cyanide in drinking water samples. Samples of cyanide anions are mixed on-chip with negatively charged silver nanoparticles, forming aggregates which are detected by Raman spectroscopy. Reproduced with permission from the Royal Society of Chemistry. B) Device used by Hoonejani *et al.* [78] to detect and distinguish between multiplexed populations of beads coated with different SERS biotags. The beads are 'flow focused' into the centre of a microfluidic channel where they are sequentially probed using Raman. Reproduced with permission from the Royal Society of Chemistry. C) Device used by Zhang *et al.* [77] to monitor fatty acid binding to receptors on kidney cells. The fatty acids were diluted to give five concentrations using a gradient generator which then fed into a cell culture array containing cultured kidney cells. SERS-active nanorods were then added to the cell culture array, allowing for bound fatty acids to be detected. Reproduced from [77]. Originally published by MDPI under an open access CC BY license.

A number of studies have used label-free Raman techniques and CARS in conjunction with microfluidics, negating the need for SERS-active metal nanoparticles. Kim *et al.* [80] used label-free Raman spectroscopy to analyse lipids produced by microalgae in a droplet microfluidic device as a proof-of-concept towards larger scale testing for the production of biofuels (figure 1.12.A). Differences in the rate of lipid production were reported as the nitrogen content was changed. Craig, Mazilu and Dholakia [123] used wavelength-modulated Raman Spectroscopy to discriminate between pharmaceuticals on a paper microfluidic device. Quantitative detection of both paracetamol and ibuprofen were reported at nanomolar concentrations, demonstrating that the technique used could overcome the inherent fluorescence background in paper microfluidics. CARS was used by O'Dwyer *et al.* [124] to image 5 µm polystyrene microparticles between 2850 cm^{-1} and 3200 cm^{-1} as they passed through a microfluidic channel as a proof-of-concept for utilising CARS in liquid biopsies. Bergner *et al.* [125] used CARS to image two solutions as they flowed through two separate microchannels, and were able to distinguish between two isotopomers of toluene.

Stimulated Raman scattering (SRS), a technique similar to CARS, was used by Cao *et al.* [68] to measure the lipid droplet content of single cells on a microfluidic device (figure 1.12.B). This involved seeding cells into a network of miniature culture chambers, with cells adhering to the device surface. A network of microvalves controlling the flow in the device was used to add the lipid oleic acid to the cells, which was shown to increase the amount of lipid droplets within the cells. Considerable cell to cell variation was reported, demonstrating the importance of single-cell studies.

The potential for microfluidic devices to provide novel and convenient platforms for studying the interactions between a large number of single cells and drugs makes it an attractive solution to expand upon the work by Jamieson *et al.* [10] in studying the lipid content of cancer cells. By utilising microfluidic techniques, there is the potential to miniaturise such studies, providing a simple way of providing single cells for analysis, a gradient generator to treat the cells with multiple concentrations of drugs and analysis of the cells with Raman Spectroscopy.

Future iterations of such a platform could also utilise 3D cell cultures and constant perfusion of nutrients and drugs in order to provide a better representation of *in vivo* conditions, however this is beyond the scope of this thesis.

1.4 Objectives and Thesis Outline

The aim of this work was to build upon the work reported by Jamieson *et al.* [10], in which label-free Raman spectroscopy was used to monitor changes in the lipid composition of cancerous cells when treated with drugs targeting lipid synthesis. It was aimed that the suitablility of combining this technique with a microfluidic device should be explored, allowing for the treatment of cells with multiple concentrations of lipid synthesis targeting drugs. The suitability of using such a device with CARS in order to increase the speed at which cells within the device could be imaged was also explored.

In chapter three, PDMS and other silicone and plastic based materials are shown to be incompatible with Raman imaging of lipid bands due to overlapping peaks. FEP is chosen as an alternative material since it contains no CH groups. The development of methods for successfully creating microfluidic devices with this seldom-used material is reported and discussed. In chapter four, FEP devices are used alongside traditional cell-culture platforms to investigate interactions between cells and FASN inhibitor orlistat or SCD1 inhibitor CAY10566. Results from both methods are compared.

In chapter five, the suitability of the device is discussed including complications arising from the FEP and the advantages and disadvantages of using the device over traditional platforms. Finally, a number of potential improvements to the device are discussed.

This thesis is the first report that a microfluidic device has been used as a platform to treat cells with lipid metabolism inhibiting drugs and monitored with Raman spectroscopy. Additionally, this is the first report where FEP has been used in microfluidics in order to solve a problem with overlapping Raman bands of the substrate and the analyte.

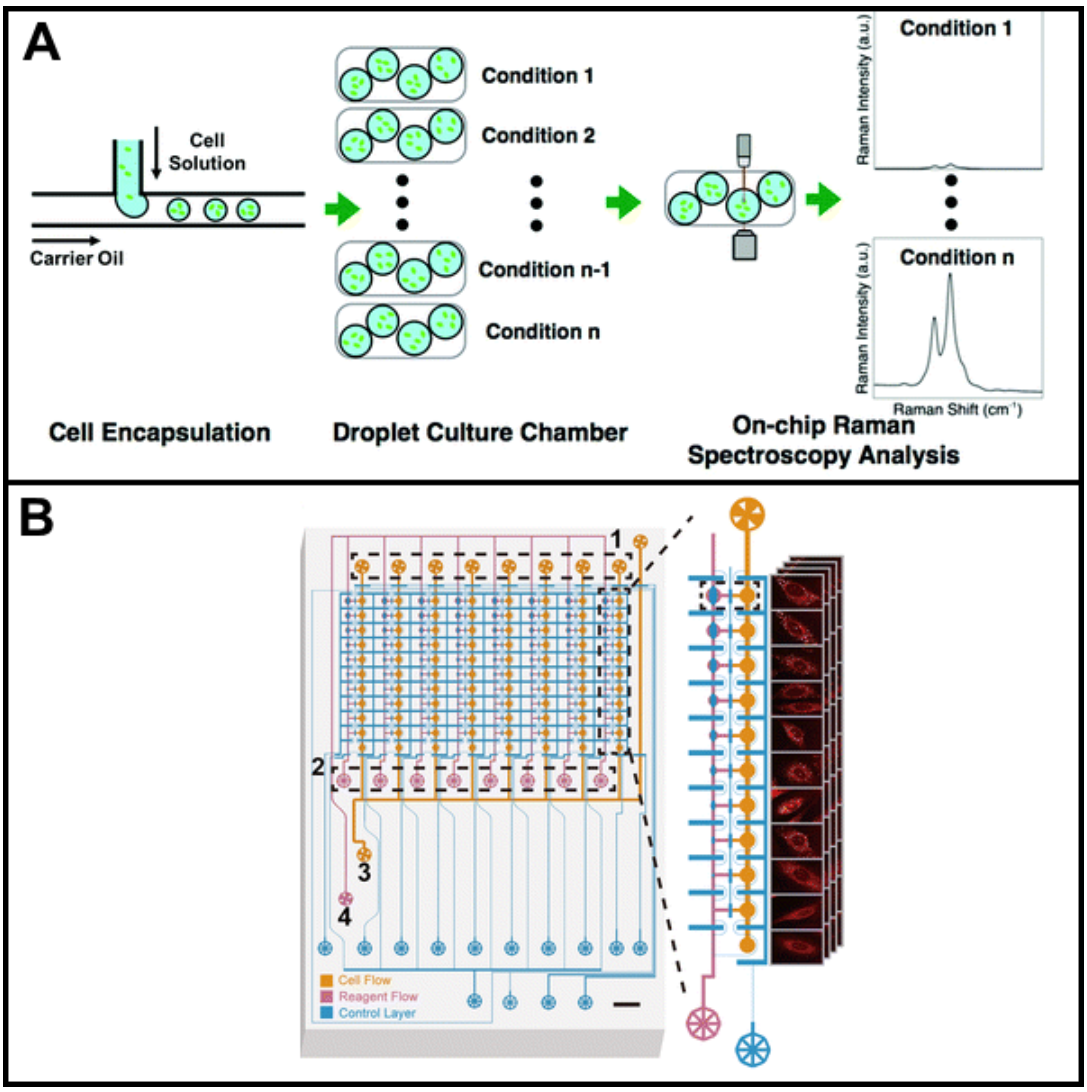

Figure 1.12: Microfluidic devices used with label-free Raman techniques. A) Device used by Kim *et al.* [80] for studying lipids produced by algae. Algae cells were encapsulated in droplets to provide a contained microenvironment. The amount of lipids produced by the algae over time could then be measured using Raman spectroscopy. Reproduced with permission from the Royal Society of Chemistry. B) Device used by Cao *et al.* [68] to measure lipid droplets in single cells. Cells were seeded in a culture chamber array and oleic acid was added through microvalves. SRS was used to measure the distributions of lipid droplets. Reproduced with permission from the American Chemical Society.

Chapter 2.

Materials and Methods

2.1 Equipment and Materials

Following are lists of equipment, materials and manufacturers that were used during this project.

2.1.1 List of Equipment

Equipment	**Manufacturer**
Photo-Masks (Chrome on Glass)	JD Photo Data, UK
Photo-Masks (Acetate)	JD Photo Data, UK
Oxygen Plasma Asher: Pico A	Diener Electronic, Germany
Manual Hydraulic Press: Atlas	Specac, UK
Bench Drill: FBS240E	Proxxon, Germany
Biopsy Punches (1 mm and 3 mm)	SmithKline Beecham ltd, UK
Hotplate: EchoTherm HP60-2	Torrey Pines, USA
Hotplate: 11-102-49SH	Fisher Scientific, UK
Spin Coater: Resist Spinner 5000	EMS, UK
Oven: UM200	Memmert, Germany
Vacuum Pump: Welch MP 101 Z	Ilmvac, Germany
Microscope: Axio Observer A1	Zeiss, Germany
Objective: 20X EC Plan Neofluar	Zeiss, Germany
Camera: Dalsa Genie-HM 1024	Stemmer, UK
Microscope: Axiovert A1	Zeiss, Germany
Objective: 20X EC Plan Neofluar	Zeiss, Germany
Camera: Dalsa Genie-HM 1024	Stemmer, UK

Raman Microscope: Rennishaw inViva	Rennishaw, UK
Objective: 20x N PLAN EPI	Leica, Germany
Camera: inViva CCD Camera	Rennishaw, UK
Raman Microscope: Witec Alpha 300 R	Witec, Germany
Objective: 50x LMPLAN	Olympus, Japan
Camera: CCD9422	Witec, Germany
Multiphoton Microscope: SP8	Leica, Germany
Objective: 25x HC FLUOTAR L	Leica, Germany
Detector: Inbuilt Photomultiplier tube	Leica, Germany
Syringe Pumps AL-1000	World Precision Instruments, UK
PTFE Tubing	Cole Parmer, USA
1ml Glass Syringes	Hamilton Company, USA
Needles	Fisher Scientific, UK
Glass Slides	Fisher Scientific, UK
Glass Bottomed Dishes	Ibidi, Germany
Glass Coverslips	VWR, UK

2.1.2 List of Materials

Materials	**Manufacturer**
Sylgard 184 (PDMS and Curing Agent) 1317318	Dow-Corning, USA
SU8 3035 Photoresist Y311074	MicroChem, USA
Microposit EC Solvent	Rohm and Haas, USA
Perfluorooctyl-trichlorosilane 448931	Sigma-Aldrich, UK
hydroxypropyl methylcellulose (HPMC) 9963	Sigma-Aldrich, UK
PBS Tablets 524650	Sigma-Aldrich, UK
FEP (0.5 mm and 3 mm) FP341400/FP343300	Goodfellow, UK
PTFE Sheets (0.5 mm) FP301400	Goodfellow, UK
76.2 Silicon Wafers 695	University Wafer, USA
Calcein C3099	Thermo Fisher Scientific, UK

Ethidium Homodimer-1 (EthD) E3599	Thermo Fisher Scientific, UK
Orlistat O4139	Sigma-Aldrich, UK
CAY10566	Thermo Fisher Scientific, UK
DMSO 276855	Sigma-Aldrich, UK
Acetone 13277983	Fisher Scientific, UK
Methanol 10141720	Fisher Scientific, UK
Isopropanol 11398461	Fisher Scientific, UK

2.2 Preparation of Microfluidic Devices

2.2.1 Device Design

Microfluidic devices were designed using CorelDraw X5 software to produce exact-size 2-D masks of the required features. These were then printed either on acetate or as chrome-on-glass by JD photo tools, UK to produce photomasks for photolithography. Chrome-on-glass masks are able to be printed with a higher resolution than acetate, and as such were used for masks requiring features less than 20 µm in size. Acetate masks were used where possible due to their lower fabrication cost.

2.2.2 Device Schematics: PDMS-Based Flow-Driven Device

Initial feasibility studies utilised a microfluidic device that was originally designed and used by Carlota Cunha-Matos [104, 126] for capturing single cells and treating them with nanoparticles. The device consisted of three inlets for seeding cells and creating a drug concentration gradient, all feeding into a central cell trap chamber (figure 2.1). This device was used as a starting point for Raman imaging of trapped cells as it was capable of trapping single cells and was readily available for use.

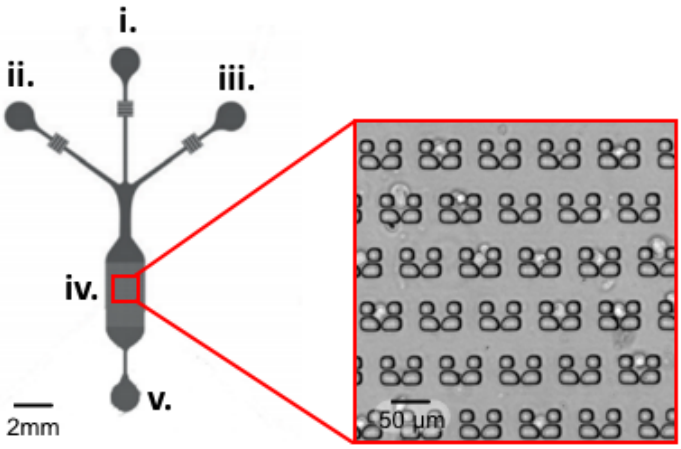

Figure 2.1: PDMS-based device schematics. Cells are seeded through inlet i. and driven towards the cell trap chamber iv. Once sufficient cells have been trapped, inlets ii. and iii. are used to co-flow cell culture media and drug-containing media to form a concentration gradient across the cell trap chamber. Waste exits the device through the outlet v. Insert shows brightfield view of the cell traps within the cell trap chamber. Image partly reproduced from [126].

2.2.3 Device Schematics: FEP-Based Flow Driven Device

To create FEP-based microfluidic devices, a two-layer approach was taken for device design whereby an upper layer of FEP contained the microfluidic channels for liquids and cells to pass through. This layer was bonded to a lower layer of FEP containing 'pit'-style cell traps beneath the channels for the cells to fall into. The initial flow-driven device consisted of a central chamber (i) connected to two cell-seeding inlets (ii, iii) and a concentration gradient generator (iv) (figure 2.2.A). This layer of channels was sat on top of a lower layer containing 40 µm diameter cell traps (figure 2.2.C). The purpose of this device was to capture cells within the traps beneath the central chamber and treating them with a variety of drug concentrations created by the gradient generator. Due to issues with the channels collapsing during bonding, a further iteration of the design contained six 200 µm diameter pillars within the cell trap chamber in an attempt to hold the chamber up during the bonding process (figure 2.2.B). Each inlet is 1 mm in diameter, with the intention of being connected to a syringe pump via PTFE tubing.

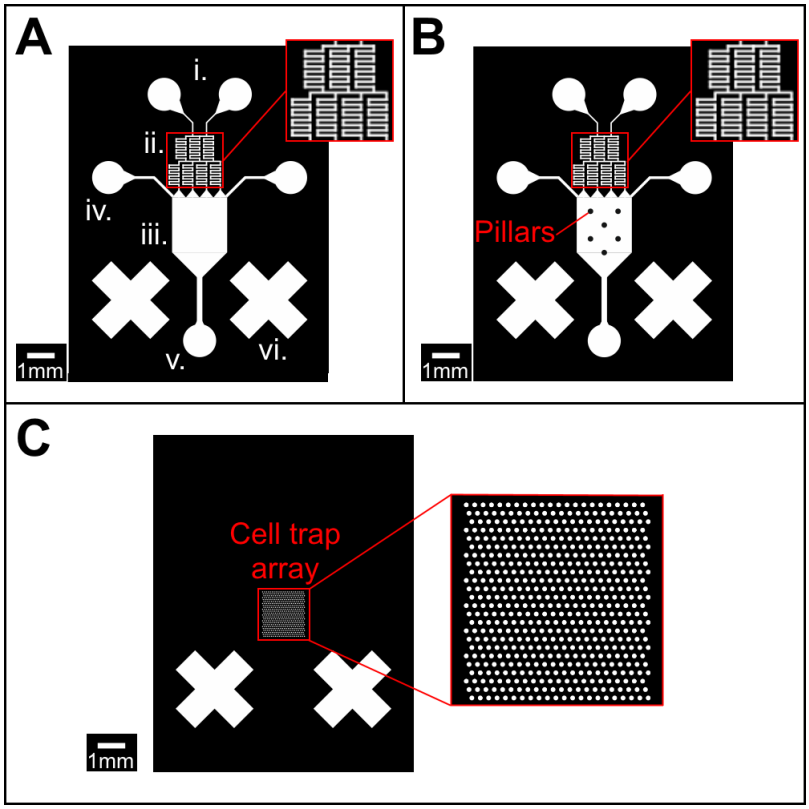

Figure 2.2: Flow driven FEP device schematics. A) Channel layer schematic with two drug inlets (i.) connected to a gradient generator (ii.) feeding into a central chamber (iii.). Two cell inlets (iv.) also feed into this chamber and there is an outlet for waste (v.). Two large crosses (vi.) are also included as an alignment feature to aid the accurate bonding of the two device layers. B) An iteration of the channel layer with the addition of six 200 µm pillars in the central chamber intended to prevent chamber collapsing during bonding. C) Trap layer containing 528 circular pit traps with diameters of 40 µm. This is designed to sit directly beneath the central chamber in the channel layers of the device. Device dimensions: Inlet/outlets: 1.2 mm diameter, Gradient generator: 0.05 mm width 8 mm total path length, Central chamber: 2 mm width, 3 mm length, Bottom channel: 0.2 mm width 2 mm length, side channels: 1 mm width 2 mm length, Cell traps: 0.04 mm diameter, 0.04 mm separation.

2.2.4 Device Schematics: FEP-Based Pressure Driven Device

Following difficulties with the flow-driven FEP device, a pressure-driven FEP device was designed as an alternative. This device consisted of five parallel cell culture chambers (figure 2.3.A), each containing three arrays of 156 40 µm diameter cell traps (figure 2.3.B). Each chamber had its own separate 3 mm inlet and outlet wells, allowing each to be treated under different conditions. Two 1 mm alignment holes were included in each layer to facilitate pegging the layers together prior to bonding.

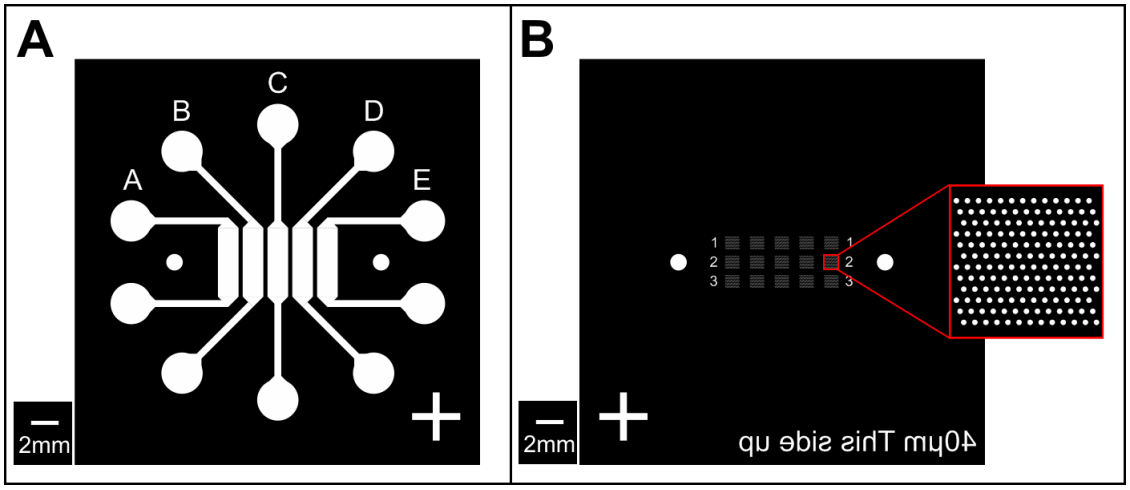

Figure 2.3: Pressure-driven FEP device schematics. A) Channel layer consisting of five parallel chambers each fed by a 3 mm diameter inlet well and connected to a 3 mm diameter outlet well. B) Trap layer containing three arrays of 156 40 µm diameter traps per chamber. Both layers contain two 1 mm diameter alignment holes to ensure that the traps and channels are aligned during bonding. Crosses on each layer allow an easy visual check of device alignment prior to bonding. Device dimensions: Inlet/Outlet wells: 3 mm diameter, Channels: 0.5 mm width, 5.3 mm length, Cell trap chambers: 1.5 mm width, 6 mm length, Cell traps: 0.04 mm diameter, 0.04 mm separation.

2.2.5 Fabrication of SU8 Masters for Microfluidic Devices

Microfluidic master templates, from which PDMS replicas could be cast, were fabricated by photolithography. Approximately 4 mL of SU8 3035 photoresist was spun onto a silicon wafer at a speed of 2500 rpm for 30 s to give a thickness of approximately 45 µm. This was then pre-baked at 95°C for 5 minutes.

A photo-mask (either acetate or chrome-on-glass) containing microfluidic features was then placed on top of the photoresist and the sample was then exposed to collimated UV light for 20 s and then heated to 65°C for 60 s and then at 95°C for 5 minutes. The master was developed in MicroPosit EC solvent for at least 3 minutes, or until features were clearly visibly. This was then hard-baked at 200°C for 20 minutes. In order to prevent PDMS from adhering to the master, it was silanised by vapour deposition of perfluorooctyl-trichlorosilane. This was done by adding 50 µL of perfluorooctyl-trichlorosilane to a dish placed beneath the master in a vacuum chamber. A vacuum was applied for 45 minutes to create a thin layer of silane on the master. This allowed PDMS to be cast on the master without becoming stuck.

2.2.6 Soft Lithography and Bonding of PDMS on Glass Devices

In order to create PDMS microfluidic devices and structures liquid PDMS prepolymer was combined with curing agent at a weight ratio of 10:1 and stirred until gas bubbles formed in the mixture. This mixture was then poured on top of the features of an SU8 master (described in section 2.2.5) and degassed in a vacuum chamber for 40 minutes until all of the bubbles were gone. This was then baked in an oven for at least 2 hours at 70°C - 80°C until set. Typically 30 g of prepolymer was used for this process to give an approximate layer thickness of 4-6 mm.

The PDMS was removed from the wafer and devices were cut out. Inlets and outlets were punched with a 1 mm biopsy punch. Devices were then placed inside an oxygen plasma asher alongside glass microscope slides. The pressure inside the asher chamber was reduced to 0.2 mBar before oxygen was flowed into the chamber for 6s at 50% power. The devices were removed from the asher and placed feature side down onto the slides in order to bond them together. The devices were then transferred to an oven at 70°C - 80°C for 1 hour to ensure maximum bonding between the PDMS and the glass.

2.2.7 Creation of PDMS Stamp for FEP Devices

To micropattern FEP for microfluidic devices, a hardened PDMS stamp first had to be created. PDMS was cast as described above in section 2.2.6 from an SU8 master to create the PDMS 'mould'. Since the features on this cast were 'grooved' they needed to be inverted by casting another PDMS layer on top to create a 'ridged' stamp. The PDMS mould was treated with oxygen plasma at 99% power for 2 minutes. Following this it was submerged in 0.1% Hydroxypropyl Methylcellulose (HPMC) in PBS solution for 30 minutes and dried with nitrogen. This created a thin layer of HPMC on top of the PDMS, allowing for PDMS-on-PDMS casting without the new layer sticking (figure 2.4.A).

The mould was then ready for the stamp to be cast on top of it. The mould was placed on a glass slide and, in order to ensure that the stamp was as flat as possible, 3 mm thick FEP spacers were placed around the edges (figure 2.4.B). Another batch of PDMS was mixed at a prepolymer to curing agent weight ratio of 6.7:1 (using 1.5x the normal amount of curing agent) in order to create a more rigid material for the stamp. This was degassed for 40 minutes and poured over the PDMS mould. A glass slide was then placed on top and clamped down with metal clips. This was then placed in an oven at 80°C for at least 2 hours. The new PDMS stamp was then peeled from the original cast and heat treated at 250°C for 1 hour in order to remove gasses that would otherwise leech out during the hot embossing process.

2.2.8 Hot Embossing, Drilling and Thermal Bonding of FEP

In order to create microfluidic devices from FEP, features are micropatterned using hot embossing, inlet/outlet wells are drilled and the two layers of the devices are thermally bonded to produce sealed channels. FEP sheets (0.5 mm or 3 mm thick) were cut to size and placed over the PDMS stamp. The FEP and PDMS was then placed between the plates on a thermal press. The plates were then tightened until they were almost, but not quite touching the sample, and heated to 265°C (figure 2.5.A). Once the sample was heated, the plates were then tightened on to the sample and left for 2 minutes.

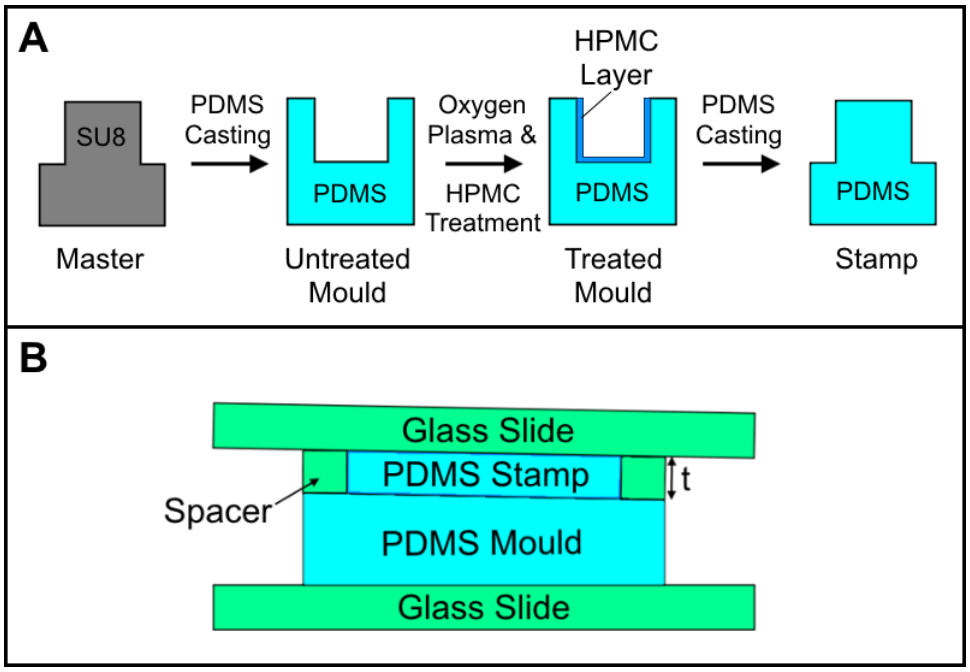

Figure 2.4: Method for the creation of the PDMS stamp used for the hot embossing of FEP. A) The PDMS mould is first cast from a SU8 master. This is then treated with oxygen plasma to reduce its hydrophobicity, allowing for treatment with HPMC solution, to create a thin HPMC layer. From this mould the PDMS stamp can then be cast. B) Flat casting technique used to create the PDMS stamp. When cast normally, there can be a tilt in a PDMS layer such as in the PDMS mould. The stamp needs to be as flat as possible for accurate transferral of features during hot embossing. Placing spacers of a known thickness between the mould and an upper glass slide ensures that the PDMS stamp is cast with uniform thickness.

The plates were then cooled, and the sample removed. Since the PDMS stamp is cured with a lower prepolymer to curing agent ratio, the stamp is more rigid than 'ordinary' PDMS, reducing its deformation under pressure.

Inlet and outlet holes/wells were then created. For flow driven devices, where tubing was to be connected, these were simply punched with a 1 mm biopsy punch. For pressure driven devices, where liquid was to be directly pipetted, 3 mm wells had to be made using a drill as 3 mm biopsy punches were damaged when punching was attempted. Guide holes in the centres of the wells were first punched from the featured side with a 1 mm biopsy punch. Following this, wells were partly drilled with a 3 mm drill bit from the non-featured side until only a thin layer remained.

The wells were then finished by punching out the remaining thin layer with a 3 mm biopsy punch from the featured side (figure 2.5.B). This process minimised the rough edges left behind by the drill.

Devices were then thermally bonded to form sealed microchannels. The FEP layers to be bonded were sandwiched between two blocks of 6 mm thick PDMS which contained the same grooved features as the FEP channel layer. This reduced the amount of pressure over the centre of the channels during bonding and decreased the risk of the channels collapsing. The layers of this assembly were aligned by punching 1 mm holes in alignment features and 'pegging' them together with cut and blunted needles. The assembly was then placed on a thermal press. The plates of the press were tightened until the top plate was just in contact with the top PDMS layer, and heated to 260°C. Sufficient pressure for bonding was provided by the thermal expansion of both the sample and the sandwiching PDMS. The sample was left for 10 minutes at 260°C before being cooled back to room temperature (figure 2.5.C).

2.2.9 Pre-filling of FEP microfluidic devices

Prior to loading pressure-driven FEP devices with cells, they were first pre-filled and treated to remove air bubbles. Devices were first filled with 70% IPA solution by applying 20 µL to each of the inlet wells. This filled the channels, but also created large air bubbles, especially over the trap arrays. The devices were then degassed for 5 minutes to reduce the size of these air bubbles. Liquid remaining in the inlet wells was then pipetted out, and 20 µL of PBS was added to each inlet well. Devices were monitored on a microscope while the PBS flowed through the device, washing out the IPA. This process was easily visible as there was a distinct loss of contrast in the channel features as the PBS filled the devices due to a close match between the refractive indices of PBS and FEP. All liquid was pipetted out of the outlet wells and 20 µL of PBS was added to them to minimise the risk of evaporation. PBS-filled devices were then placed in a fridge at 2°C - 8°C until use in order to allow the remaining air bubbles to completely dissolve.

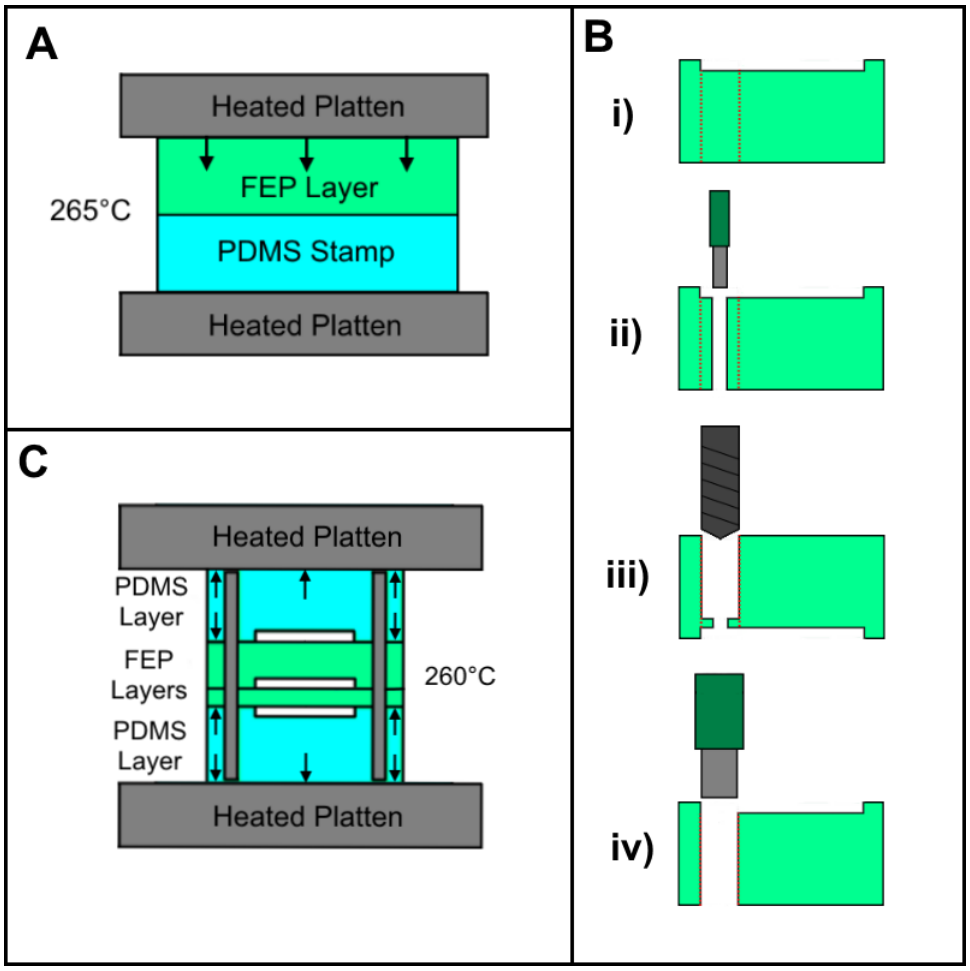

Figure 2.5: Methods for creating FEP devices. A) Hot embossing of FEP on the PDMS stamp. The plattens of the heat press are heated to 265°C and tightened by hand to produce enough pressure for feature transferral. B) Inlet/outlet wells are drilled into the FEP channel layer using a multi-step process. i) FEP layer features-side-up showing where well is to be drilled. ii) A 1 mm biopsy punch is used to create a guide hole from the featured side. iii) A 3 mm drill bit is used from the non-featured side to drill through most of the bulk, leaving behind a thin layer close to the featured side. iv) A 3mm biopsy punch is used to remove the thin layer from the featured side to ensure a smooth edge. C) Bonding of FEP devices. The FEP layers are aligned by putting two blunted needles through 1 mm alignment holes, ensuring that the cell traps will be directly below the channels. The layers are then sandwiched between two PDMS layers containing the same features as the channel layer. This assembly is placed between the plattens of the heat press with the top platten only just in contact with the top PDMS layer. The plattens are then heated to 260°C and thermal expansion of the PDMS provides enough pressure to bond the two FEP layers.

Devices stored for prolonged periods of time (3 days+) were frequently checked to ensure the PBS in the channels/wells had not evaporated, and were accordingly topped up with PBS when required.

2.3 Cell Culture

Cultures of PC3 human prostate cancer and PNT2 human 'normal' immortalised prostate epithelium cell lines were used in this project and were maintained and prepared by Corinna Wetherill and Lauren Jamieson. PC3 cells were cultured in Dulbecco's Modified Eagle's Medium (DMEM) and PNT2 cells were cultured in Rosewell Park Memorial Institute Medium (RPMI). Both media were supplemented with 1% penicillin, 1% fungizone and 10% foetal bovine serum (FBS).

2.3.1 Loading Cells in Flow-driven Microfluidic Devices

Suspensions of either PC3 or PNT2 cells at concentrations of $1x10^6$ cells/mL were first aspirated at 1.5 μLs^{-1} into PTFE tubing via syringe pumps loaded with 1 mL glass syringes. Following this, the pumps were set to dispense at 1.5 μLs^{-1} and when liquid was visibly leaving the ends of the tubing, tubes were inserted into the inlets of the microfluidic device. Cell seeding into traps was then monitored on a microscope until at least 50% of traps had been filled (approximately 20-30 minutes), the flow was halted and the tubing removed. The device could then be carefully transported to a Raman microscope for analysis. This process could have been run for longer to fill a greater number of traps, however these devices were only used in preliminary imaging studies where they were found to be unsuitable.

2.3.2 Treatment of Cells in Pressure-driven Microfluidic Devices

PBS was aspirated from the inlet and outlet wells of pre-filled FEP devices (described in section 2.2.9.). 20 µL of either PC3 or PNT2 cells at a concentration of $1x10^6$ cells/mL were then pipetted into the inlet wells and cell seeding was monitored on a microscope.

Once cells had settled into traps, residual volume from the inlet wells was aspirated and 20 µL of cell culture media (DMEM for PC3 cells and RPMI for PNT2 cells) was added to the inlet wells to flush through any residual cells within the channels. Devices were incubated for 24 hours at 37.5°C, all liquid was then aspirated from both inlet and outlet wells and 20 µL of cell culture media containing dilutions of either orlistat in DMSO, CAY10566 in DMSO or DMSO was pipetted into the inlet wells. Devices were left for 10 minutes for the drug containing media to fill the channels and all liquid was aspirated from the outlet wells. Both inlet and outlet wells were filled with the drug-containing media to prevent evaporation, and incubated for 48 hours at 37.5°C. Following incubaton, devices were checked under a microscope to ensure no air bubbles had formed in the channels. Cells were then either treated with fluorescent viability stains or fixed with paraformaldehyde (PFA) for Raman spectroscopy.

For cells undergoing fluorescence viability staining, all liquid was aspirated from the inlet and outlet wells of the device. 4 µL of Ethidium Homodimer-1 (EthD) and 1 µL of calcein were added to 2 mL of PBS. 20 µL of this solution was then added to each inlet well of the device, which was incubated at 37.5°C for 30 minutes. Following this, all liquid was aspirated from the inlet and outlet wells and 20 µL of PBS was added to the inlet wells to wash out residual stain from the channels. Cells were then treated with PFA prior to imaging. To fix cells within devices, all liquid was aspirated from the inlet and outlet wells of the device. 20 µL of PFA was added to the inlet wells of the device, which was left at ambient temperature for 30 minutes. All liquid was then aspirated from both inlet and outlet wells, and 20 µL of PBS was added to the inlet wells and left for 10 minutes to wash out any remaining PFA from the channels. All liquid was then aspirated from the outlet wells and both inlet and outlet wells were filled with PBS to prevent evaporation. Devices were then transferred either to either a fluorescence microscope for viability imaging (section 2.4.4) or to a Raman microscope for Raman analysis (sections 2.4.2 and 2.4.3).

2.3.3 Preparation of Cells on Coverslips and Dishes

0.5 mL of either PC3 or PNT2 cell suspensions at concentrations of $0.1x10^6$ cells/mL were added to either untreated glass bottomed dishes or 13 mm untreated glass coverslips in a 24 well plate. An additional 1 mL of appropriate cell culture media (DMEM for PC3 cells and RPMI for PNT2 cells) was added and the dishes/plates were incubated at 37.5°C for 24 hours. All liquid was then aspirated from the dishes/wells, and replaced with 1 mL media containing dilutions of either orlistat in DMSO, CAY10566 in DMSO or DMSO. Dishes/plates were then incubated for a further 48 hours before either being treated with fluorescence viability stains or fixed with PFA.

For cells undergoing fluorescence viability staining, the drug-containing media was aspirated and dishes/wells were washed with PBS. 4 µL of 2 mM EthD and 1 µL of 4 mM calcein were added per 2 mL of PBS, resulting in a solution containing 4 µM ETHD and 2 µM Calcein. 0.5 mL of this solution was added to each well/dish for 30 minutes at 37.5°C. This solution was then removed and cells were then washed with PBS and then fixed with PFA.

In order to fix cells with PFA, all liquid was first aspirated from the wells/dishes, which were washed with PBS. 0.5 mL of PFA was then added to each well/dish for 40 minutes before being aspirated and dishes/wells were washed again with PBS. Dishes/plates were then transferred either to either a fluorescence microscope for viability imaging (Section 2.4.4) or to a Raman microscope for Raman analysis (Sections 2.4.2).

2.4 Analytical Techniques

2.4.1 Raman Spectroscopy of Materials

In order to determine the compatibility of teflons with the Raman methodology and to compare spectroscopic properties to that of PDMS, small samples of PDMS (cured at a ratio of 10:1), PTFE tubing and 0.5 mm thick FEP were prepared and placed on a glass microscope slide.

Single Raman spectra of each of these were taken using a Witec Alpha 300R Raman spectrometer using 532 nm laser excitation, 50x dry lens and with 10 accumulations at an exposure time of 0.5s.

2.4.2 Raman Mapping of Cells

Cells either fixed to coverslips, glass bottomed dishes or in FEP microfluidic devices were mapped using a Rennishaw InViva Raman Microscope. Maps were made by manually drawing boxes around each analysed cell using Rennishaw Wire software. The maps were set up to measure 1 spectrum every 3 µm in both x and y directions with a dry 20x 0.4 NA lens, using a 1800 l/mm grating and a 50 mW 532 nm diode laser. The settings used for each spectrum were 1 s exposure time, 3 accumulations, 50% laser power (25 mW), centred at 3000 cm^{-1}. These imaging settings were optimised for obtaining Raman spectra from cells in FEP devices. It was decided that the imaging parameters should be kept identical when imaging cells in devices and on glass coverslips in order for a direct comparison. No visible damage could be seen in the cells following illumination with the laser.

2.4.3 CARS Imaging

Cells in microfluidic devices were imaged on a CARS-enabled multiphoton microscope using a 25x 0.95 NA water immersion objective lens. The system was set up to stimulate Raman scattering at 2851 cm^{-1} and at 2930 cm^{-1} for lipids and proteins respectively. Power, exposure and gain settings were varied in order to produce optimal images, however due to ineffective results no ideal settings were determined.

2.4.4 Fluorescence Imaging

Cells either fixed to glass coverslips, glass bottomed dishes or in FEP microfluidic devices that had been treated with fluorescent viability stains were imaged using either a Zeiss Axio Observer A1 or Axiovert A1 fluorescence microscope. Samples were imaged with excitation/emission wavelengths of 495/515 nm for calcein and 528/617 nm for EthD. Excitation intensity and exposure time settings were optimised for each image.

Cells in each field of view were then counted as either viable or non-viable depending on whether they were stained with calcein or EthD respectively.

2.5 Data Analysis

2.5.1 Analysis of Spectral Data

Spectral data from Raman maps was preprocessed using inbuilt functions within Rennishaw Wire v4.2 software for cosmic ray removal, baseline subtraction, noise filtering and smoothing. The preprocessed spectral maps were then exported as .spc files, which could then be imported into MATLAB for analysis.

A custom MATLAB script was used to analyse the data to calculate average L/P ratios for each analysed cell (figure 2.6.A, Appendix B). Preprocessed spectral data was imported into MatLab and truncated between 2800 cm^{-1} and 3050 cm^{-1} in order to exclude data from outwith the region of interest. Each individual spectrum was then thresholded based on the peak prominence of the highest peak detected by MATLAB's inbuilt 'findpeaks' function between 2915 and 2940 cm^{-1}, which is assumed to belong to the protein peak around 2933 cm^{-1}. Spectra with peak prominences below 100 were discounted from analysis in order to remove data from outwith the cell as well as weak or noisy spectra (figure 2.6.B). The threshold prominence value of 100 was chosen qualitatively as an approximate point at which the spectra are no longer significantly impacted by noise. Every passing spectrum was then averaged to give a mean spectrum for the entire map. Peaks were then detected using the 'findpeaks' function and identified as being the largest peaks between 2844 and 2856 cm^{-1} for lipids and between 2915 and 2940 cm^{-1} for proteins. The peak height for the lipids was then divided by the peak height for the proteins to generate an overall L/P ratio for the map.

L/P ratios from all maps of a given condition were then averaged to give a mean value and standard deviation for that condition. Different conditions were compared by using an unpaired student's t-test.

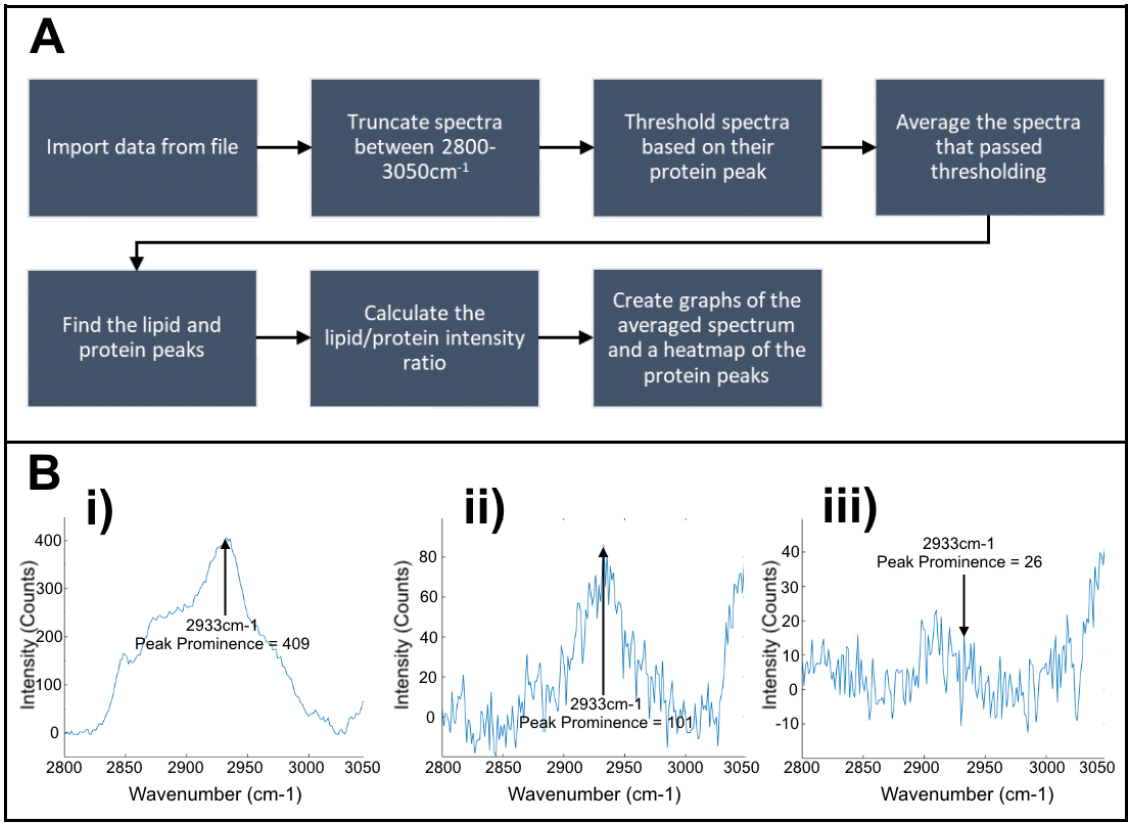

Figure 2.6: MatLab analysis script for calculating the L/P ratios from spectroscopic datasets. A) Flowchart detailing the workflow of the analysis script. After importing the data it is truncated between 2800 cm^{-1} and 3050 cm^{-1} to exclude data from unwanted parts of the spectra. The spectra are then thresholded based on the peak prominence of the protein peak and then all passing spectra are combined to form one average spectrum per cell. From this a lipid/protein ratio is calculated and graphs are produced of the average spectrum and intensity heatmaps of the lipid and protein peaks within each cell. B) Examples of i) passing, ii) threshold and iii) rejected spectra from the thresholding process with protein peak prominences of 409, 101 and 26 at 2933 cm^{-1} respectively.

2.5.2 Analysis of Cell Viability

Fluorescence images of cells treated with viability stains were analysed to give an overall viability. For each imaged field of view, the number of cells stained with calcein (green) were counted as viable, whereas the number of cells stained with EthD (red) were counted as non-viable. These numbers were combined with those from other fields of view and used to calculate the percentage of viable and non-viable cells. Fisher's exact test of proportions was used to compare the percentages of viable cells between different conditions.

Chapter 3.

Development of an FEP-Based Microfluidic Device for Raman Imaging of Cellular Lipid Composition

3.1 Introduction

Lipid metabolism is upregulated in cancer cells and recent studies have shown that Raman spectroscopy can be used to estimate the lipid content of cells by comparing peaks attributed to lipids and proteins (For a full discussion, see section 1.2.4). So far studies have focused on 'traditional' platforms such as glass coverslips or glass bottomed dishes. A simple microfluidic approach could allow for the miniaturisation of such studies, allowing for cells to be treated with multiple concentrations of drug on a single platform, enabling more experiments to be carried out simultaneously at the single-cell level. Additionally, such a device could potentially be used to study how the lipid composition of cancerous cells changes in real time as they are being treated with lipid targeting drugs.

This chapter describes the development a microfluidic platform capable of trapping single cells, treating them with multiple concentrations of drugs targeting lipid metabolism, and imaging the cellular response using Raman spectroscopy.

3.2 Raman Imaging of Lipids in a PDMS-Based Device

The initial device used for testing this concept was originally designed by Carlota Cunha-Matos and its operation described in Cunha-Matos *et al.* [104]. A schematic of the device can be found in figure 2.1. The device consists of a series of cell traps within a central chamber, with three inlets feeding into it.

The central inlet is designed to seed cells in the device, while the two flanking inlets are designed to generate a concentration gradient of drugs to treat the cells in the traps. An outlet to the bottom of the chamber allows for waste to be removed from the device. The device was designed to be made from PDMS on glass using standard soft lithography techniques.

A device was loaded with a suspension of PC3 cells at $1x10^6$ cells/ml at a flow rate of 1.5 µl/min for 1 hour. Once cells were loaded into the traps, the flow was stopped and the device was transferred to a confocal Raman mapping system (Rennishaw inViva). Single spectra, centred around 3000 cm^{-1}, were taken of cells in the traps, and of the background produced by the PDMS (figure 3.1.A). Despite the PDMS being well out of the plane of focus, it produced such a strong background signal that no spectral information from the cells could be obtained. The device was then transferred to a CARS system (Leica SP8 Multiphoton), as this system was had a significantly reduced background from out-of-focus signals due to having a smaller pinhole for confocal imaging. The lasers were tuned to image the sample at 2851 cm^{-1} and 2933 cm^{-1} corresponding to lipids and proteins respectively. While some weak signal from the cells was detected, signals still suffered from the high background, and images were dominated by the in-focus PDMS cell traps themselves (figure 3.1.B). As a result, PDMS was deemed to be an unsuitable material for this application and an alternative was sought.

3.3 FEP as an alternative Material

The unsuitability of PDMS as a material in this application comes from its chemical structure ($(C_2H_6OSi)_n$), containing two CH_3 groups per repeating unit. The lipid and protein peaks from the cells come from CH_3 and CH_2 groups respectively, and so the strong background peaks produced from the PDMS totally obscure the weaker peaks produced from the cells. Common alternative polymers used for microfluidics include polyurethane [127], polystyrene [128] and poly(methyl methacrylate) [129]. Like PDMS, all of these contain C-H bonds, ruling them out as suitable alternatives in this application. Glass devices are another alternative [87].

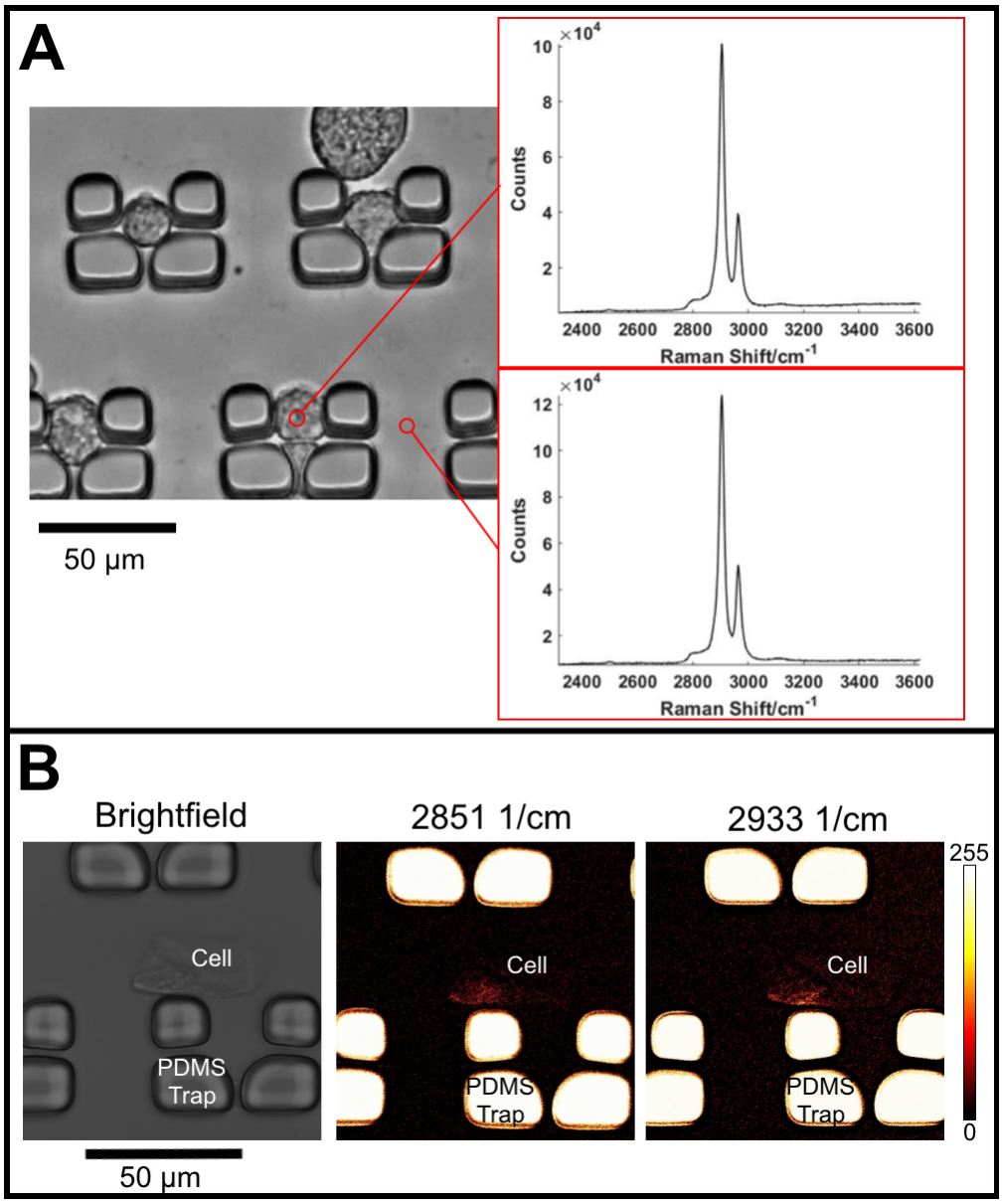

Figure 3.1: Raman and CARS measurements using original PDMS device. A) Raman spectra taken of a cell in one of the traps and of the background signal in the cell trap chamber. The two signals are shown to be indistinguishable, preventing analysis of the cells within the device. B) Brightfield and CARS imaging of a cell beside a trap. CARS images of the cell taken at 2851 cm^{-1} and 2933 cm^{-1} show a limited amount of signal coming from the cell, however the signal-to-noise is very poor and the images are dominated by the signal coming from the PDMS traps themselves. Colour scalebar shows pixel brightness in the CARS images, however images have been contrast-adjusted to maximise visibility of the cell for the purpose of demonstration. These images are therefore not quantitative.

The micropatterning of glass is difficult in comparison to other materials, and requires wet etching using hazardous chemicals such as hydrofluoric acid, a highly corrosive acid which can cause serious burns if it comes into contact with human skin or eyes [130]. Hydrofluoric acid etching may also have been problematic for creating the small single-cell trap features and the poor gas permeability of glass makes it an unsuitable platform for long term cell culture [131].

Fluorinated ethylene-propylene (FEP), an optically transparent type of Teflon, was chosen for as an alternative since it contains no C-H bonds. Its suitability for use in microfluidics was introduced by Ren *et al.* [88], who successfully developed a method for fabricating devices made from Teflons, and tested suitability for a number of applications including simple channels, pneumatic valves and cell culture devices.

To verify the suitability of FEP for Raman imaging, samples of FEP, Polytetrafluoroethylene (PTFE) and PDMS were prepared and their spectra measured (figure 3.2). PTFE is a common form of Teflon, but is not optically transparent, making it unsuitable as a material for this application. It is included here for comparison.

From these spectra it can be seen that neither PTFE or FEP contain any peaks between 2800 cm^{-1} and 3000 cm^{-1}, whereas PDMS does. This is the region in which cellular lipids and proteins are expected to be seen, and so these results indicate that Teflons are a more suitable material for creating devices capable of imaging cells in this way.

3.4 Flow Driven FEP Device Design

FEP devices require hot embossing in order to create features, as opposed to PDMS which uses soft lithography. Additionally, thermal bonding is required to seal the devices, as opposed to bonding using oxygen plasma. The smallest features on the original device are the gaps in the cell traps at 2 µm wide. While Ren *et al.* [88] claims that it is possible to hot emboss features as small as 150 nm, features of this size were deemed to be unlikely to survive the potentially destructive thermal bonding process. It was decided instead to use a single cell pit trap style (figure 3.3.B). This requires two layers of featured FEP, one on the top containing the channels and one on the bottom containing the traps.

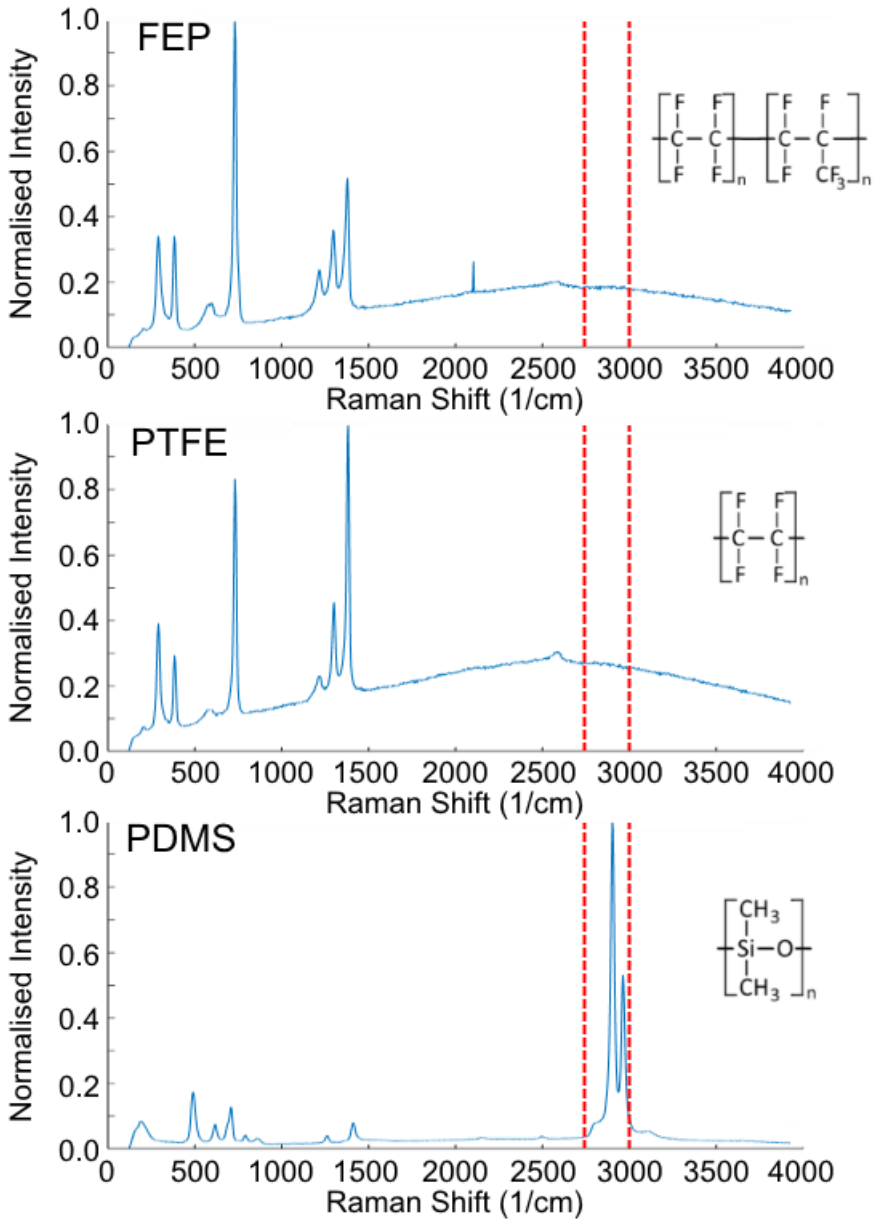

Figure 3.2: Raman spectra of FEP , PTFE and PDMS. Spectra are normalised between zero and one to allow for easy comparison between shapes. The red dashed lines show the approximate spectral region in which cell signals are expected to be measured. PDMS is the only one of these materials to contain large peaks in this region of the spectrum, demonstrating its unsuitability as a material for this application. Since there are no peaks in this region in either FEP or PTFE, they are much more suitable as substrates for Raman imaging of cellular lipid and protein peaks. Spectra taken on a Witec Alpha 300R Raman spectrometer using 532 nm laser excitation, a 50x lens, with 10 accumulations at 0.5 s exposure time.

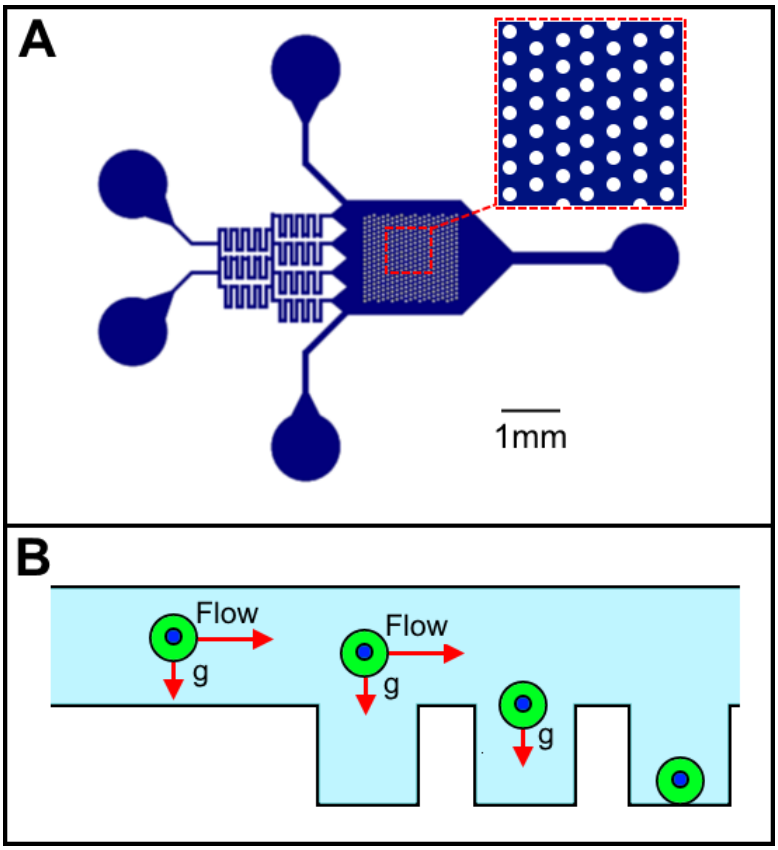

Figure 3.3: Syringe pump actuated FEP microfluidic device. A) Device diagram. Full schematics and a description of intended operation can be found in figure 2.2. B) Diagram showing the principal behind the pit traps. Cells flowing through the device will drop to the bottom of the channel and fall into the traps where they can be stored for treatment with drugs and analysis.

The new device design consisted of a central chamber filled with traps, fed by four inlets to the top and one outlet to the bottom (figure 3.3.A). As with the PDMS device, this device was designed to be flow driven, using syringe pumps and tubing in its operation. The first stage of its designed operation was to load the traps with cells from the two side inlets. Since the hydraulic resistance of the path to the bottom outlet is lower than that of the other inlets, the cells should flow down over the traps. Following successful loading, the cell inlets were designed to then be blocked by turning off the flow, but keeping them attached to the syringes. Drugs could then be added to the device using the other two inlets, connected to the microchannel style gradient generator [111], to provide a drug concentration gradient across the cell trap chamber.

3.5 Creation of a PDMS Stamp for Hot Embossing

Whereas PDMS can be easily cast and cured using a liquid prepolymer and curing agent, sheets of FEP can be micropatterned by hot embossing. According to Ren *et al.* [88], this will fail if done directly on to an SU8 master due to the trapping of air and must instead be done on a specially prepared PDMS stamp with a 5:1 weight ratio mix of prepolymer to curing agent (instead of the standard 10:1 ratio). This lower ratio results in a stiffer PDMS cast due to the increased amount of crosslinking agent. According to a paper by Wang, Volinsky and Gallant, PDMS cast with a 5:1 ratio should have an elastic modulus of approximately 3.6 MPa compared to an elastic modulus of approximately 2.6 MPa for PDMS cast at the usual 10:1 ratio [132].

An SU8 master was created with the new device design using standard photolithography techniques (Section 2.2.5). Since the features on the SU8 master are of the same profile as the desired PDMS stamp, a simple direct cast would result in features of the wrong orientation (figure 3.4.A). In order to create a stamp with the correct feature profile, a direct cast of the SU8 master using 10:1 PDMS (hereafter referred to as the PDMS mould), was treated with 0.1% hydroxypropyl methylcellulose (HPMC) solution for 30 minutes. This creates a thin layer of cellulose on the PDMS mould, allowing for the stamp to be cast without sticking.

It is important that the PDMS stamp should be as flat as possible to ensure even embossing of the FEP. In order to achieve this, a flat casting method was used when casting the stamp on the PDMS mould. 3 mm thick pieces of FEP were used as spacers and were placed around the edges of the PDMS mould. The PDMS mould was mounted on a 75x50 mm glass slide and the uncured 5:1 ratio PDMS was poured over the mould. A second glass slide was placed over the top, and secured using metal clips (figure 3.4.B). Aluminium foil was used to prevent the uncured PDMS from leaking out, and the stamp was cured in the oven at 70°C for 2 hours. Since the spacers kept the top glass parallel to the PDMS mould, the newly cast stamp had an even thickness of 3 mm. Additional casts did not require the spacers as the first cast left behind an even 3 mm high PDMS wall around where the first stamp had been cut out.

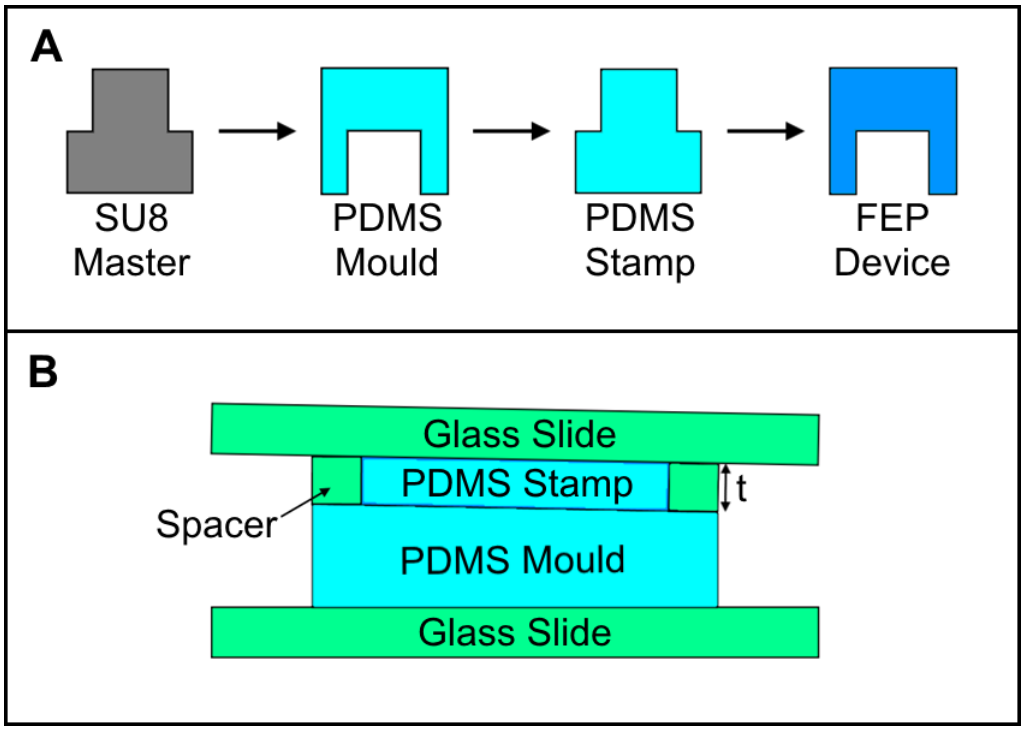

Figure 3.4: Casting methods used to create the PDMS stamp. A) Cross section profiles of channels created at various steps. The PDMS stamp has to be the same profile as the SU8 master so an intermediate PDMS mould is cast, allowing for the FEP device to have features of the correct profile. B) Flat casting method used to create an even thickness PDMS stamp on the PDMS mould.

The newly cast stamp was placed on a glass slide and heated to 250°C for 1 hour on a hotplate to remove gasses from the bulk as recommended by Ren *et al* [88]. During cooling back to room temperature, the PDMS cracked and became unusable, even when the temperature was ramped down in 5-15°C steps (figure 3.5.A). Initially this was done by allowing the mould to cool with the hotplate, but was attempted again by ramping down the temperature in 5-15°C steps. A standard 10:1 PDMS cast heated and cooled in the same way and was found to survive the process entirely undamaged, despite the claim by Ren *et al.* that PDMS cured at this ratio will form gas bubbles at temperatures over 150°C.

This process was repeated again, this time using an intermediate 6.7:1 weight ratio of PDMS prepolymer to curing agent (using 1.5 times the amount used in a standard 10:1 ratio cast).

As with the 10:1 ratio PDMS, this cast was found to withstand the heat treatment process, but is more rigid (According to Wang, Volinsky and Gallant, PDMS cast at a ratio of 7:1 will have an elastic modulus of approximately 2.9 MPa [132]), suggesting that it should be more suitable for use as a stamp in hot embossing.

Following successful heat treatment, it was discovered that the trap layer stamps were being damaged during the PDMS on PDMS casting process, with many of the traps being ripped off when peeling the stamp from the PDMS mould (figure 3.5.B). This was not found to be an issue with the channel layer stamp. It is likely that the HPMC was not effectively coating the traps on the mould due to their small size (30-50 µm) as well as the hydrophobicity of the PDMS. In addition to an ineffective stamp, the damaged traps were left behind in the mould, rendering it unusable (figure 3.5.B). To combat this, a step was added to the mould preparation protocol to treat it with oxygen plasma at 100% for 2 minutes prior to HPMC treatment. This reduced the hydrophobicity of the mould, allowing for effective HPMC coating of the traps. This resolved the issue and effective stamps could be cast on these moulds (figure 3.5.C).

3.6 Hot Embossing of FEP

According to the methods provided by Ren *et al.* [88], hot embossing of FEP should take place at a temperature of 265°C with an applied pressure of approximately 10kPa for 2 minutes. The heat press used for hot embossing has its pressure scale in tonnes rather than kPa. 10 kPa converted into tonnes gives 0.005 T, whereas the smallest increment on the pressure gauge is 0.04 T, an order of magnitude higher. This assumes that the pressure will be spread across the whole of the heated platens (3" in diameter), when this weight would actually be concentrated on the area of the sample being pressed, further reducing the required weight.

The original protocol used to emboss FEP was to place it on top of the stamp (figure 3.6.A) and to sandwich this between two sheets of PTFE. This assembly was then placed on the heat press, and clamped into place while the press was heated to 265°C.

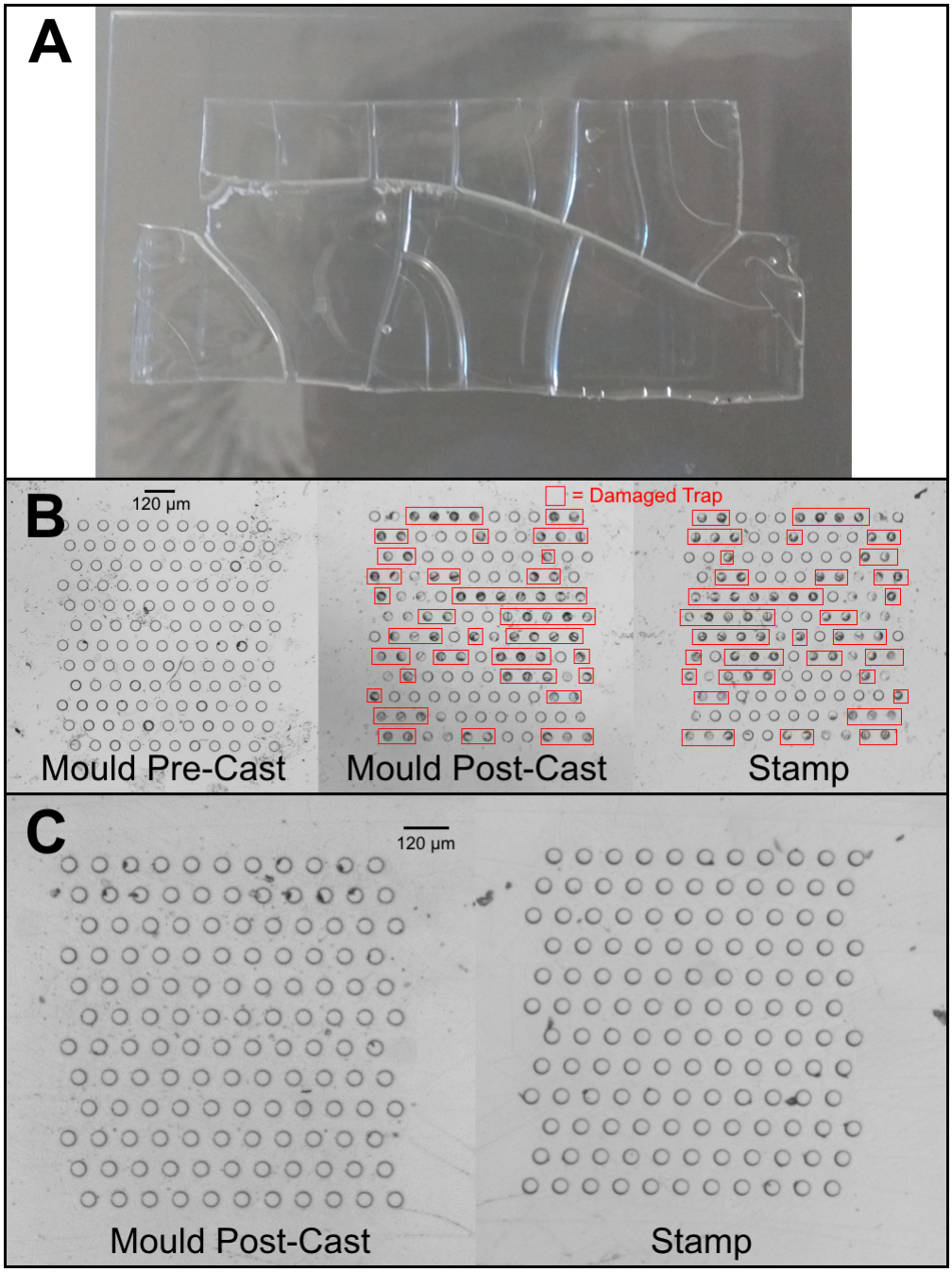

Figure 3.5: Problems creating the PDMS stamp. A) PDMS stamp cast with 5:1 ratio cracked during heat treatment making it unusable. B) Many traps damaged (highlighted in red) during casting of PDMS stamp on PDMS mould due to ineffective HPMC treatment, leaving both unusable. Note that the pattern of damaged traps on the stamp and mould are mirrored. C) Successful casting of PDMS stamp on a PDMS mould treated with oxygen plasma prior to HPMC treatment.

Once the press had reached 265°C, it was left for 1 minute to allow the sample to be evenly heated and then between 0.04 and 0.1 Tonnes of pressure was applied to the sample using the pump. This was applied for 2 minutes before the platens were cooled back to room temperature (figure 3.6.B.i.-iii.).

Initial attempts using this protocol on the trap layer resulted in severely deformed traps being produced in the FEP (figure 3.6.B.iv). There are a number of factors which may have contributed to this result. The FEP and stamp are clamped in place while still at room temperature, and thermal expansion of both materials will start to provide axial pressure as the sample is being heated. Since the PDMS stamp is comparatively flexible compared to room temperature FEP, the traps may be initially squashed when clamped in to place and this effect may be worsened by the additional pressure produced by thermal expansion. Additionally, since the two materials have different thermal expansion coefficients, they will undergo a different amount of lateral thermal expansion, which may further contribute to the deformed traps. To fix this issue, the protocol was adapted so that the sample is not clamped into place prior to heating. Instead the top plate is brought very close to the sample so that it still heats sufficiently, and once heated to 265°C, brought into contact with the sample for 1 minute to ensure correct temperature. Following this, pressure is applied for two minutes before the sample is cooled back to room temperature (figure 3.6.C.i.-iii.). It was also found that pressure from the pump is not required to produce features in the FEP, and so pressure is applied by tightening the plates by hand. While some traps still have a slight deformation, likely due to the traps being embossed at a slight angle, this change to the protocol vastly improved the features and reliably produces viable traps (figure 3.6.C.iv.).

3.7 Bonding of FEP Device Layers

While PDMS devices can be easily bonded using oxygen plasma, Teflon based devices require thermal bonding. This involves heating the two layers of FEP to near their melting point and applying a very small amount of pressure before cooling back to room temperature.

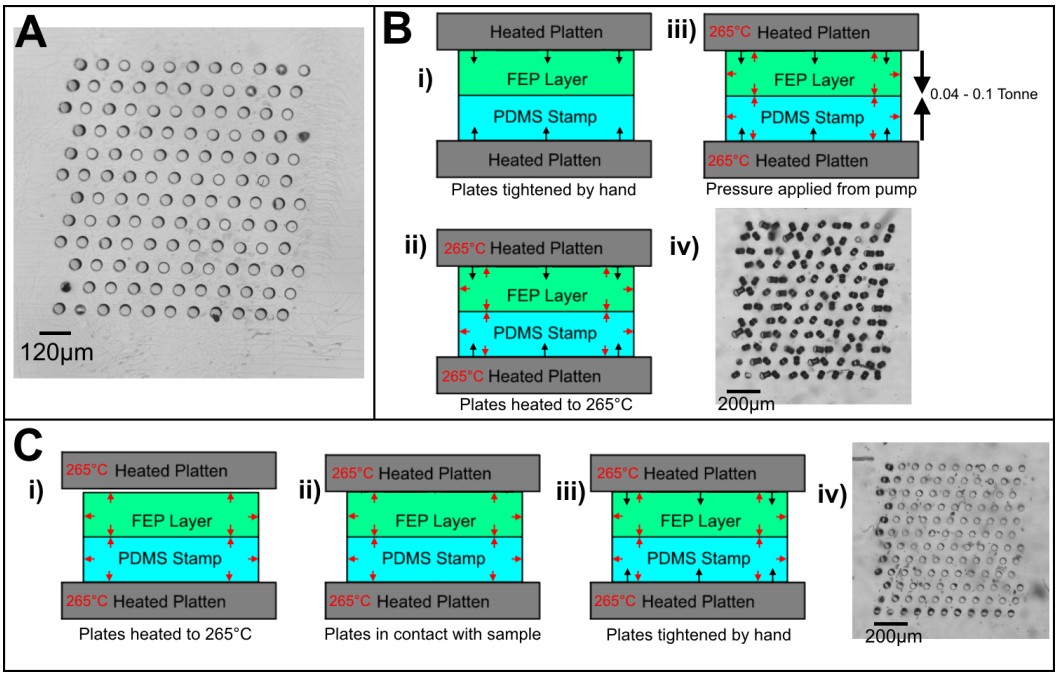

Figure 3.6: Hot embossing of traps. A) Stamp used for hot embossing showing uniform round traps. B) Original hot embossing protocol i) FEP is placed over the stamp in the heat press which is tightened creating a small amount of pressure (black arrows). ii) The heat press is heated to 265°C in order to bring the FEP to above its glass transition temperature. This also causes thermal expansion of the sample (red arrows). iii) 0.04-0.1 Tonne of pressure was applied using the hydraulic pump on the heat press. iv) The resulting FEP traps were highly warped and unusable. C) FEP pressing created using altered protocol. i) The sample is placed on the heat press with the top plate not quite in contact in order to allow for thermal expansion as it is heated to 265°C. ii) Once the heat press reaches temperature, the top plate is moved into contact with the sample for 1 minute. iii) The plates are tightened by hand to provide pressure for hot embossing. iv) The resulting traps are far improved compared to the original method, although some deformations are still visible.

This is a delicate procedure, as too much pressure will lead to damaged features and too little pressure will fail to bond the layers. Ren *et al.* [88] showed that a constant application of pressure will result in damaged features, and instead developed a method using thermal expansion to provide variable pressure. While Ren *et al.* used a stainless steel screw clamp to hold the sample in place as it was heated to 260°C, a similar method has been developed using only the heat press and some PDMS layers. The FEP sample was placed between two 6 mm thick flat layers of PDMS (cast at the usual 10:1 weight ratio) and placed on the heat press. The top plate was then lowered until it was just in contact with the top PDMS layer, and the press was heated to 260°C for 10 minutes. The sample was then cooled back to room temperature and the PDMS layers may be re-used for another device.

One difficulty in this process is aligning the top and bottom layers so that the traps are underneath the channels. While it is possible to align the features by eye, the low friction of Teflons makes it extremely difficult to transfer the sample to the heat press without the layers being displaced. To solve this issue, 1 mm holes were punched in alignment features in both the top and bottom layers, and the layers were "pegged" together using blunted needles (figure 3.7). This ensured that the layers were kept in alignment during the bonding process and that the traps were positioned underneath the channels.

It was frequently found after bonding that the devices would have a collapsed cell trap chamber, causing liquid to flow around the edges and not in the centre (figure 3.8.A). The narrower inlet channels were rarely affected by this, and liquid could be easily flown through. The original approach to combat this was to redesign the device with pillars built into the channel layer of the chamber (figure 3.8.B). This did not solve the issue, and devices created using these designs continued to collapse in the cell chamber. As an alternative solution, a directed pressure approach was developed. Instead of sandwiching the device between two featureless flat cast pieces of PDMS, layers containing the same features as the device channel layer were used to reduce the pressure being applied to the channels and chambers during bonding.

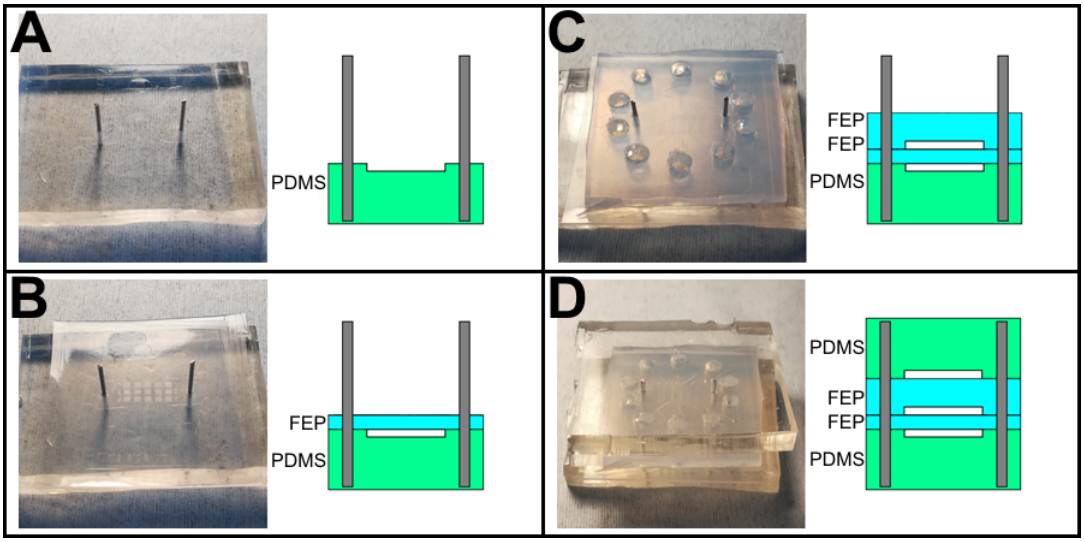

Figure 3.7: Alignment of layers during bonding. A) Lower layer of PDMS and blunted needles. B) Addition of trap layer FEP to assembly. C) Addition of channel layer FEP to assembly. D) Full bonding assembly with device layers sandwiched between upper and lower layers of PDMS all kept in alignment with blunted needles.

This prevented the chambers from collapsing, and allowed for devices to be entirely filled with liquid (figure 3.8.C).

3.8 Tubing

In order to interface the device with the syringe pumps, the inlets must be connected with tubing. This is easily achieved with PDMS by boring 1 mm holes in the inlets and inserting PTFE tubing (figure 3.9.A). Because of the flexibility of PDMS, the inlets warp to fit around the tubing and produce a watertight seal. This could not be replicated using the FEP devices as the inlets do not warp to fit around the tubing. Needles of various diameters were initially tested as an intermediate between the tubing and the inlets, but all available sizes were either too small, failing to create a seal, or too big, failing to enter the inlet.

A solution was found by inserting the tubing into the top of a 10 µl pipette tip. The bottom of the pipette tip could then comfortably be inserted into the device inlet, and due to its tapered shape, formed a watertight seal (figure 3.9.B). This allowed the devices to be connected to syringe pumps.

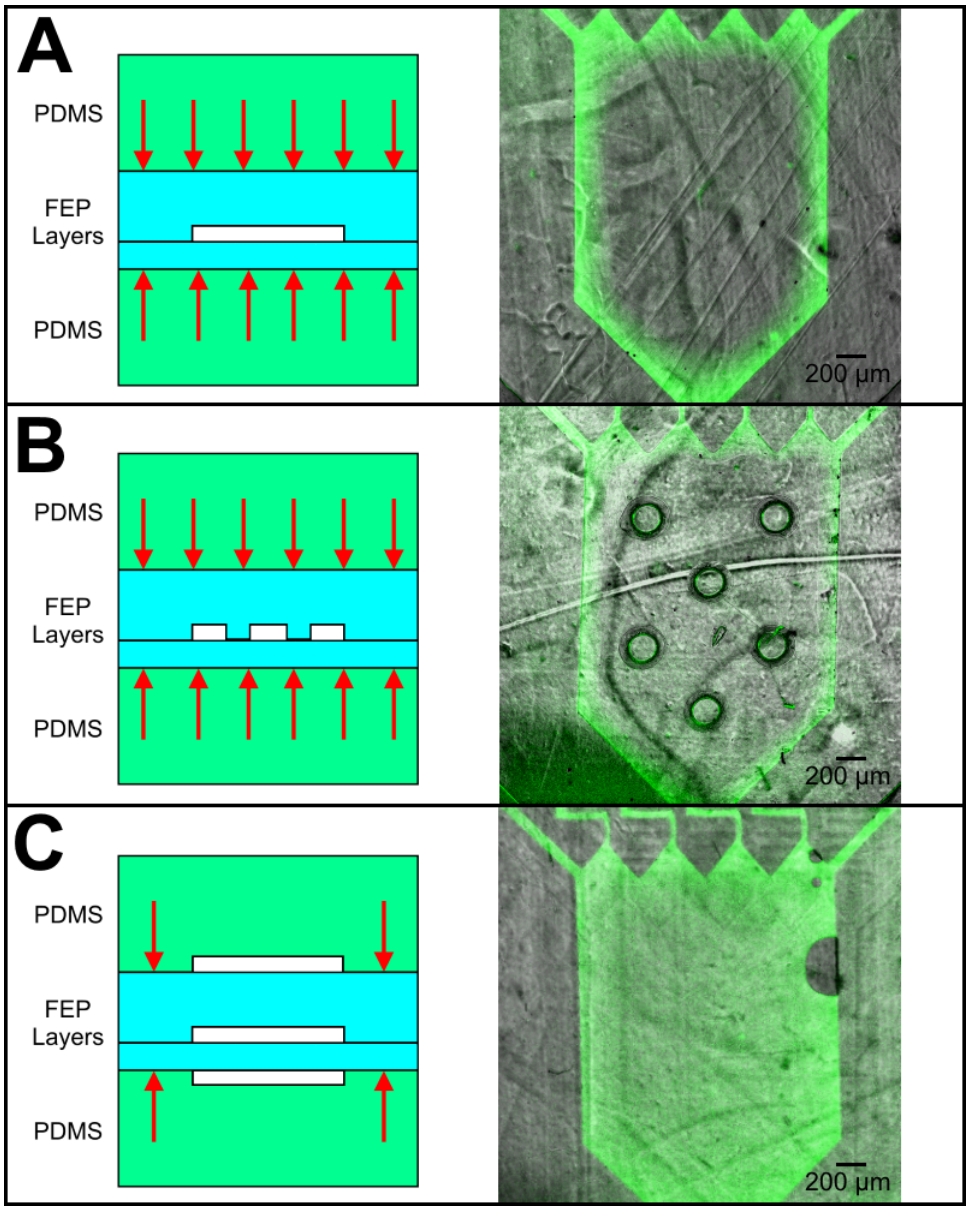

Figure 3.8: Device designs and bonding methods used to prevent collapsing chambers. Bonding diagrams and composite brightfield/fluorescence images of devices filled with calcein. A) Original device design bonded between two featureless layers of PDMS. B) Pillar device design bonded between two featureless layers of PDMS. C) Original device design bonded between two featured layers of PDMS.

Since the pipette tips were comparatively tall, and are relatively wide at the top, they were cut short (approximately 2-3 cm) so that only the bottom portion was used, allowing for easier handling.

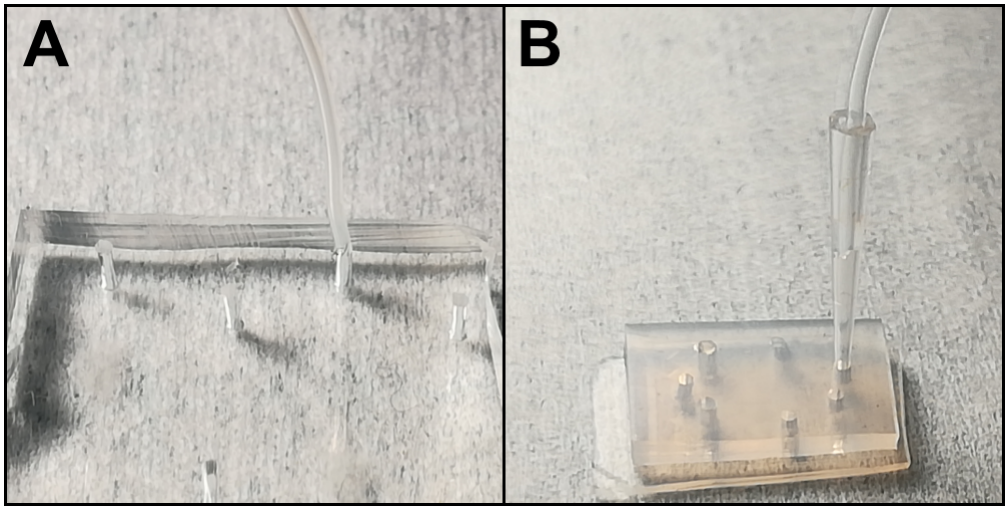

Figure 3.9: Tubing used to connect devices to syringe pumps. A) PDMS device with PTFE tubing directly connected to an inlet hole. B) FEP device with PTFE tubing connected to a shortened 10 µl pipette tip inserted into the device inlet.

3.9 Pressure Driven FEP Device Design

Early tests using the device revealed the design to be highly impractical. The main issue was that the bonding of the devices was very weak, leading to the devices being very easily damaged. This especially happened when inserting and removing tubing. No matter how careful the handling of the devices, the bonding consistently failed before an experiment could be fully set up.

An additional flaw in the design was the device's unsuitability for long term drug treatment experiments. The device was designed to establish a concentration gradient of drug across the cell trap array, however the continuation of such a gradient requires constant pumping or the drug will diffuse to all areas of the device at an even concentration. It was necessary to test the device with a 48 hour drug incubation period to compare its effectiveness with conventional techniques, and therefore this would require 48 hours of continuous pumping.

This is highly impractical as the device would also need to be incubated at 37.5°C. To solve both of these issues, the device layout was redesigned. Rather than a flow driven system using syringe pumps, a pressure driven system was chosen to drive flow in the device. Since the main cause of failure of the bonding was during the insertion and removal of tubing, this is advantageous as it merely requires the pipetting of liquids into inlet wells.

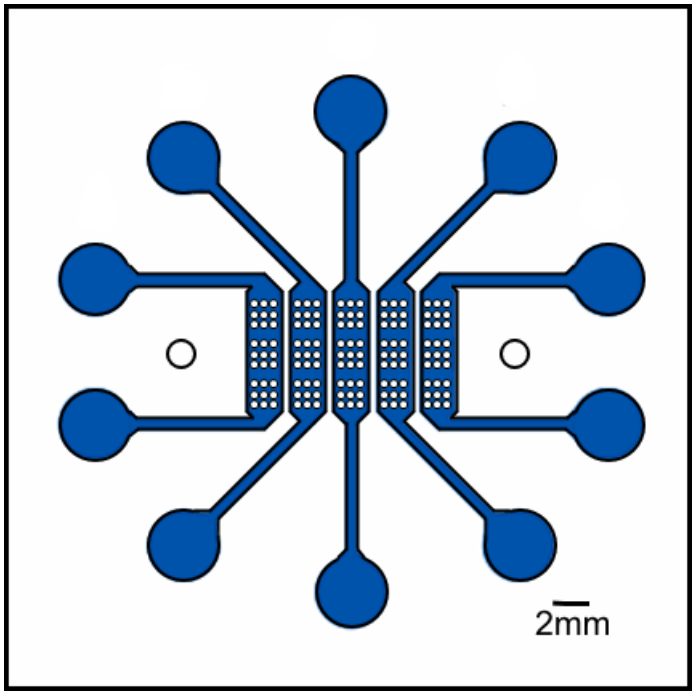

Figure 3.10: Pressure driven device design. The device has 5 parallel chambers containing three cell trap arrays each. Since each chamber is separate, they can each be kept under different conditions (e.g. drug concentration, drug type, cell type) allowing for up to 5 tests to be carried out on one chip. Two 1 mm alignment holes allow for easier alignment during bonding.

The new device consisted of five separate, parallel chambers connected to 3 mm inlet and outlet wells (figure 3.10). Each chamber contained three cell trap arrays, and could be filled independently from one another. This allowed up to five conditions to be tested per device such as cell type, drug type and drug concentration. The new device design also contained specific 1 mm diameter alignment features to allow for more accurate alignment during bonding.

Since the device did not require syringe pumps or the maintenance of a concentration gradient, it was far more suitable for 48-hour drug incubation studies. In addition, the device was far simpler to use than its predecessor, and therefore much faster to set up for an experiment.

The hydraulic capacitance of each channel can be calculated from equation 1.17. Given the inlet/outlet well radii of 1.5 mm, and using the density of water at 1000kgm^3 gives a hydraulic capacitance of 3.6x10^{-10} m^{3}Pa^{-1}. Since the cylindrical wells were to be created in 3 mm thick FEP sheets, their maximum volume can be easily calculated as 21 µl. By approximating the device as three hydraulic resistors connected in series, two with length 5.3 mm, width 0.5 mm and height 40 µm, and one with length 6 mm, width 1.5 mm and height 40 µm, and taking the dynamic viscosity of water to be 9.8x10^{-4} Nsm^{-2}, hydraulic resistance of the each channel can be approximated at 4.85x10^{12} Pasm^{-3} from equation 1.5. Assuming starting conditions of the inlet well being completely full and the outlet well being empty, equation 1.4 gives a starting flow rate of 0.36 µlmin^{-1}, which will then decrease as per equation 1.12. The flow rate in each channel should slow to 0.01 µls^{-1} after approximately 104 minutes, suggesting that this is insufficient for a constant perfusion system, however this is acceptable for initial experiments to test the suitability of the device.

Due to the larger size of this device compared to the flow-driven device, it was often found after bonding that the layers were partially unbonded (figure 3.11.B). The extent of the partial bonding could be easily visually assessed by looking at the underside. In order to increase pressure across the whole of the device, the heat press platens were moved closer together during bonding. This resulted in channel collapse despite using featured PDMS to direct pressure away from the device channels (figure 3.11.C). It was found that partially bonded devices could be re-bonded using an additional piece of PDMS over the top of the unbonded region to direct the pressure (figure 3.11.D).

3.10 Inlet and Outlet Wells

Since it is a soft material, inlet and outlet wells can be easily bored into PDMS using a biopsy punch.

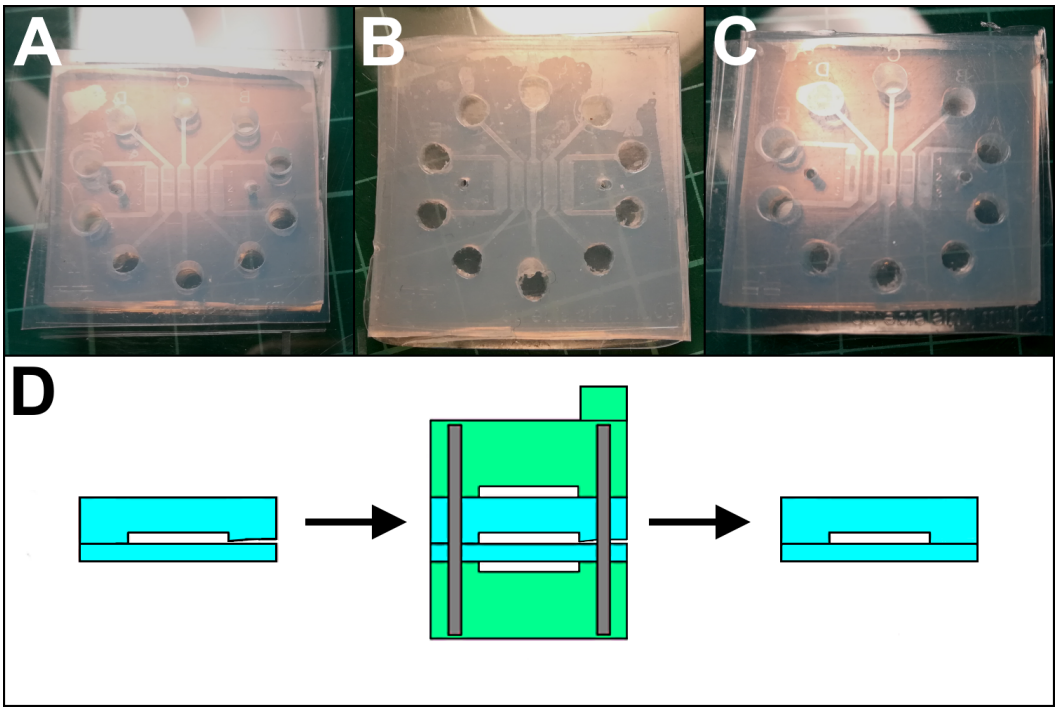

Figure 3.11: Bonding issues with the pressure driven device. A) Device bonded fully. B) Device unbonded in one corner. C) Device with collapsed cell trap chambers. D) Method for re-bonding partially bonded devices using an extra layer of PDMS over the top of the affected area.

FEP is much harder, and while inlets of 1 mm diameter can be comfortably made in the same way, larger holes such as the 3 mm diameter wells designed in the device are problematic with the 3 mm thick top device layers. Using a drill to bore 3 mm holes tended to leave rough edges on both sides (figure 3.12.A), which has the potential to interfere with bonding and/or block flow in the device. A drilling protocol was developed to prevent this. Firstly, 1 mm diameter guide holes are bored through the middle of the wells from the featured side using a biopsy punch. The device is then reversed and 3 mm diameter holes are partly drilled from the non-featured side, leaving a thin layer at the bottom of each well. Finally, the device is reversed again, and a 3 mm biopsy punch is used to punch out the remaining thin layers from the featured side (figure 3.12.B). This process ensures that there are no rough edges around the wells on the featured side, aiding with both bonding and flow within the device.

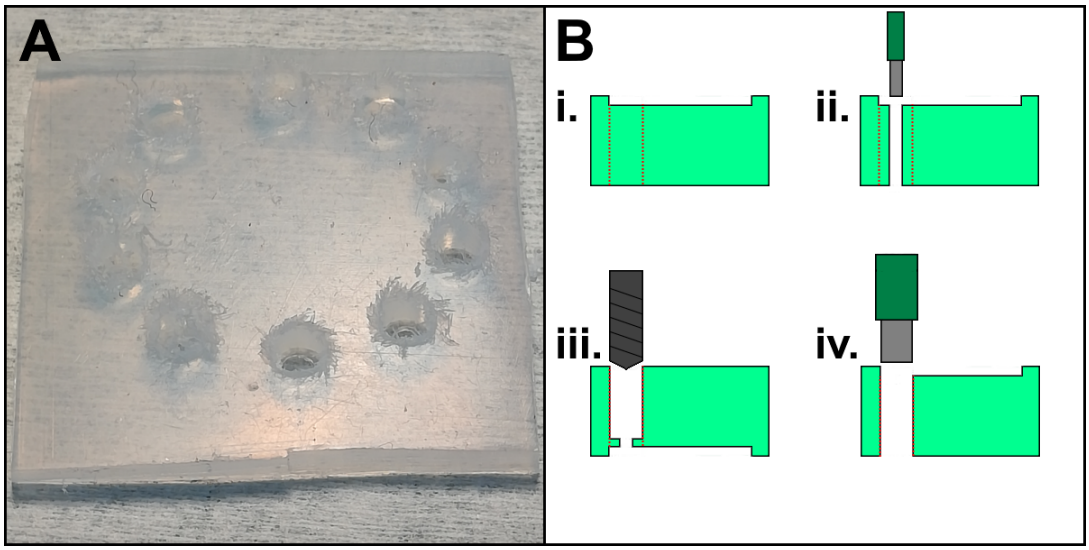

Figure 3.12: Creation of inlet and outlet holes. A) Rough edges left behind by drill. B) Method for avoiding rough edges on the featured side of the FEP channel layer. i) Area to be drilled in device. ii) Inlet/outlet is punched with a 1 mm punch from the featured side. iii) Inlet/outlet is drilled with a 3 mm drill bit from the non-featured side, but a thin layer is left behind. iv) From the featured side, the remaining thin layer of FEP is removed with a 3 mm punch.

3.11 Removal of Air Bubbles

FEP is a hydrophobic material, and as such it can be difficult to get aqueous solutions such as PBS or cell culture media to flow through the device channels at all when it is initially empty. To get around this, channels were first filled by pipetting 20 µl of a 70% IPA solution into the inlet wells. While this is effective at filling the channels and chambers, large air bubbles were frequently found to form over the traps. This significantly reduces the potential number of cells which can be trapped by the device. After filling all five channels with 70% IPA, a device was placed in a vacuum chamber for 5 minutes. The device chambers were imaged before and after degassing (figure 3.13.C), and the device was degassed for a further 5 minutes and the chambers imaged again. Since the air bubbles in this device formed exclusively over the trap arrays, the size of the air bubbles were measured as the percentage of traps that they affected. It was shown on initial filling that there was a large variance in the air bubble size between each of the five chambers (figure 3.13.A).

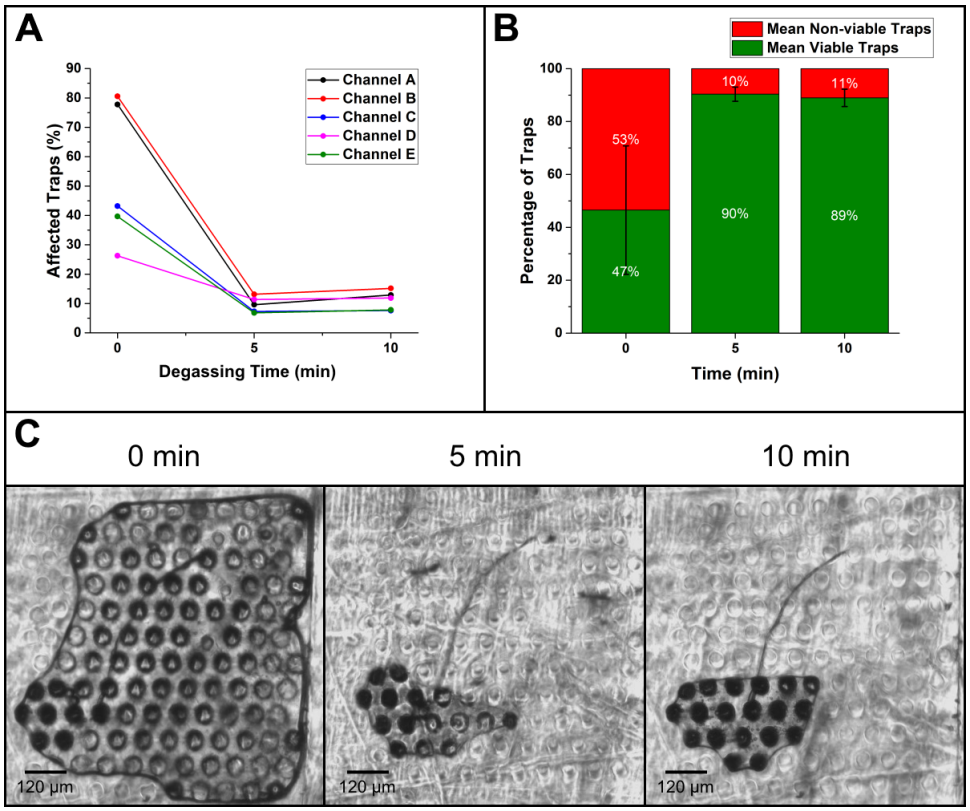

Figure 3.13: Reduction of air bubbles within a 70% IPA filled device by degassing. A) The percentage of traps in each channel affected by an air bubble upon initial filling and two 5-minute degassing steps. B) The mean percentage of traps per channel affected by air bubbles upon initial filling and two 5-minute degassing steps. Data is from 5 channels on one device, error bars are standard deviations of the percentage viable traps between each channel. C) Images of one cell trap array upon initial filling and following two 5-minute degassing steps.

Following five minutes of degassing, there was a considerable drop in the percentage of affected traps (53% to 10% (n = 5 channels), figure 3.13.B), however the additional five minutes of degassing showed no significant difference. As a result, a five minute degassing step was added to the device filling protocol.

While this degassing step greatly reduced the air bubbles formed in the devices, air bubbles still remained and blocked many of the traps. In addition to this, it was discovered that the air bubbles expanded significantly when placed in an incubator at 37.5°C and often completely blocked the channels, preventing flow within the device.

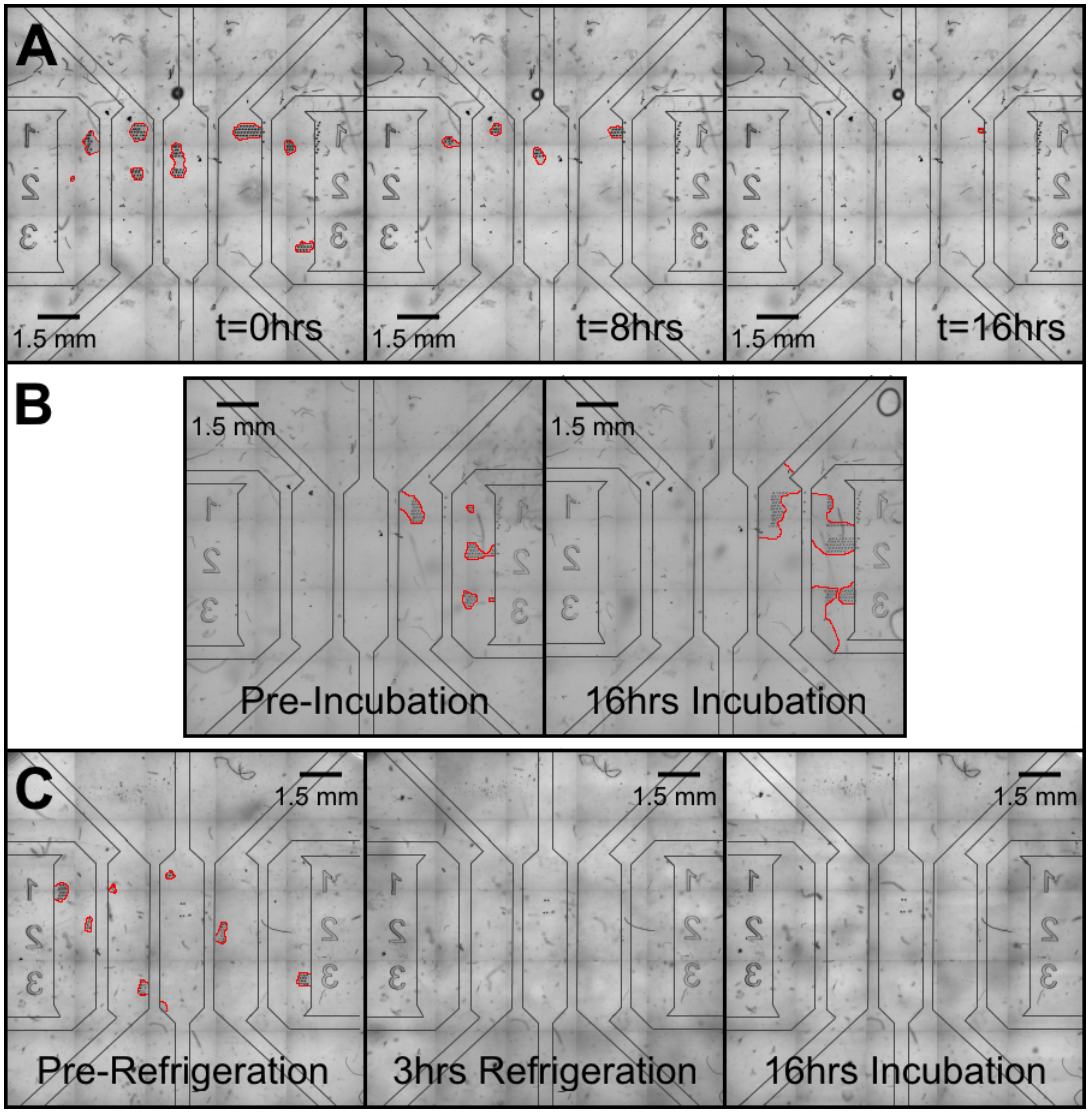

Figure 3.14: Tiled images showing processes for eliminating air bubbles. For clarity images have been overlaid with outlines of the channel boundaries and air bubbles are outlined in red. A) A PBS-filled device left overnight in ambient conditions showed a significant reduction in air bubbles. B) A PBS-filled device with air bubbles in only two of its channels was incubated overnight and shows significant expansion of the air bubbles, while the air-free channels are unaffected. C) A PBS-filled device was placed in a refrigerator, leading to all the air being dissolved. This device remained air-free following overnight incubation.

To investigate what was happening to the air bubbles, a device was filled with 70% IPA and degassed for five minutes to reduce the size of the air bubbles. The IPA was then pipetted out of the wells and replaced with a solution of PBS. The device was placed on a microscope and time lapse imaged with 30 minute intervals overnight (16 hours) at ambient conditions. In all five channels there was a reduction in the size of the air bubbles, with all but one containing no visible bubbles at all by the end of the experiment (figure 3.14.A). Following this, two of the channels in the same device had the PBS removed from their wells and were allowed to dry out. These channels were then re-filled as before with 70% IPA, degassed and then PBS. The device now had three of its channels (A,B and C) entirely filled with PBS and two of its channels (D and E) filled with PBS but with air bubbles. The device was placed in an incubator at 37.5°C overnight (approximately 16 hours), and images were taken before and after. The air bubbles in channels D and E expanded to the point where both channels became completely blocked, while the three channels containing no air bubbles initially remained completely clear of any visible air (figure 3.14.B). This demonstrated the importance of not only reducing, but entirely eradicating all air bubbles in the devices prior to any incubation.

Since air is more soluble in aqueous solutions at lower temperatures [133], a device was filled with PBS as before and placed in a refrigerator at 5°C for 3 hours. Following this step, all air bubbles in the device disappeared. The device was then placed in an incubator at 37.5°C overnight (approximately 16 hours), and the channels remained entirely free of air bubbles (figure 3.14.C). As a result, it was concluded that devices should be filled with PBS at least one day in advance of any experiments, and stored in a refrigerator to ensure that they are entirely free of air bubbles.

3.12 Chapter Summary

In this chapter PDMS was determined to be an unsuitable material for the device when Raman imaging lipids as peaks from the PDMS were obscuring any signal from the cells.

FEP, a form of Teflon, was selected instead due to a lack of CH bonds and had been previously demonstrated to be suitable for the creation of microfluidic devices by Ren *et al.* [88]. The Raman spectrum of FEP confirmed a lack of peaks in the 2800 cm^{-1} – 3000 cm^{-1} region.

Numerous problems arose during attempts to create FEP devices. Traps on the PDMS stamp ripped off during removal from the PDMS mould. This was solved by treating the mould with oxygen plasma prior to HPMC treatment to reduce the hydrophobicity, ensuring that the HPMC solution entered the traps. Initial attempts at hot embossing traps resulted in significant warping. This was solved by altering the protocol so that no pressure was applied to the sample during heating.

A method for bonding devices using a heat press was developed to keep the top and bottom layers in alignment. The wide chambers of the devices were found to collapse during bonding. This was fixed by developing a directed pressure bonding method to prevent excessive pressure directly over the chambers.

Due to difficulties with attaching tubing without bonding failure, the device was redesigned as a pressure-driven device. This also makes the device easier to operate as no syringe pumps or tubes are required.

Devices frequently contained large air bubbles upon initial filling. These expanded when placed in an incubator and often blocked entire channels. To eradicate air from the devices, a five-minute degassing step was introduced following filling. This reduced the air bubbles but did not remove them completely. It was found that by refrigerating the filled devices, all the air could be removed. With methodologies for creating FEP microfluidic devices have been developed and optimised, testing of devices with cancerous cells could take place.

Chapter 4.

Raman Imaging of Cellular Lipid Composition in a Microfluidic Device

4.1 Introduction

Following the successful creation of FEP based microfluidic devices, testing was performed using cancerous cells and drugs affecting lipid metabolism. For comparison with the devices, testing was also performed on fixed cells either in glass bottomed dishes and on coverslips. This was to compare the effectiveness of using the device against traditional platforms as used by Jamieson *et al.* [10]. The main drug tested was the fatty acid synthase inhibitor orlistat. Limited testing was also carried out using SCD1 inhibitor CAY10566. The effect of these drugs is described in section 1.1.4. Live/Dead fluorescence staining was also carried out on both glass coverslips and in devices to check the effects that Orlistat and the device have on cell viability.

4.2 Microfluidic Devices

With techniques for creating FEP-based devices now developed, their effectiveness as platforms for studying lipid synthesis targeting drugs could be evaluated.

4.2.1 Raman Spectroscopy

PC3 or PNT2 cells were added to channels on microfluidic devices that had been pre-filled with PBS (section 3.11). These devices were then incubated overnight and the media was then exchanged for either media containing 100 µM orlistat, 50 nM CAY10566. Since both drugs were diluted from stock solutions dissolved in DMSO (40 mM Orlistat and 200 µM CAY10566) media containing 0.25% DMSO was used as a control condition.

This is the same concentration of DMSO as could be found in all other conditions. The devices were then incubated for a further 48 hours before the media was washed out with PBS and then the channels were filled with PFA to fix the cells for 30 minutes. The PFA was then washed out with PBS and the cells were mapped with Raman Spectroscopy.

Individual cells were mapped by taking Raman spectra at 3 µm intervals in both x and y using a Rennishaw inViva confocal Raman microscope, 25 mW power, 3 acquisitions at 1 s per pixel. The spot size on the sample was approximately 1.6 µm diameter, corresponding to approximately 12.5 mW per µm. This is a fairly high amount of power focused into a very small area, however this does not take into account any attenuation from either the imaging system or the bottom layer of the microfluidic device, and no damage to the cells was visible following imaging. This was carried out for at least 10 cells per condition and the control and orlistat conditions were run in triplicate. Due to time constraints, CAY10566 was only tested once for both PC3 and PNT2 cells and so conclusions of its performance are less statistically robust than those of orlistat, however other studies suggest that its effect is much less than that of orlistat [10]. Most cells took between 8-12 minutes to map under these conditions, with each channel taking approximately 2 hours to image.

Maps of individual cells were analysed using the MATLAB script (Appendix B) with the same parameters to generate averaged cell spectra and calculate L/P ratios. These spectra can be seen to have a main peak at around 2930 cm^{-1} (attributed to proteins), and a prominent side peak at around 2850 cm^{-1} (attributed to lipids), as well as some other peaks in between. The side peak at 2850 cm^{-1} is seen to be relatively higher in PC3 cells treated with Orlistat than in other conditions (figure 4.1). These ratios were then pooled from all runs of each condition to calculate a weighted mean value for each condition (figure 4.2.A).

The L/P ratio for PC3 cells increased by 0.201 from 0.513 ± 0.074 to 0.714 ± 0.086, while PNT2 cells were found to have an increase of 0.036 from 0.481 ± 0.130 to 0.517 ± 0.123 when Orlistat was added.

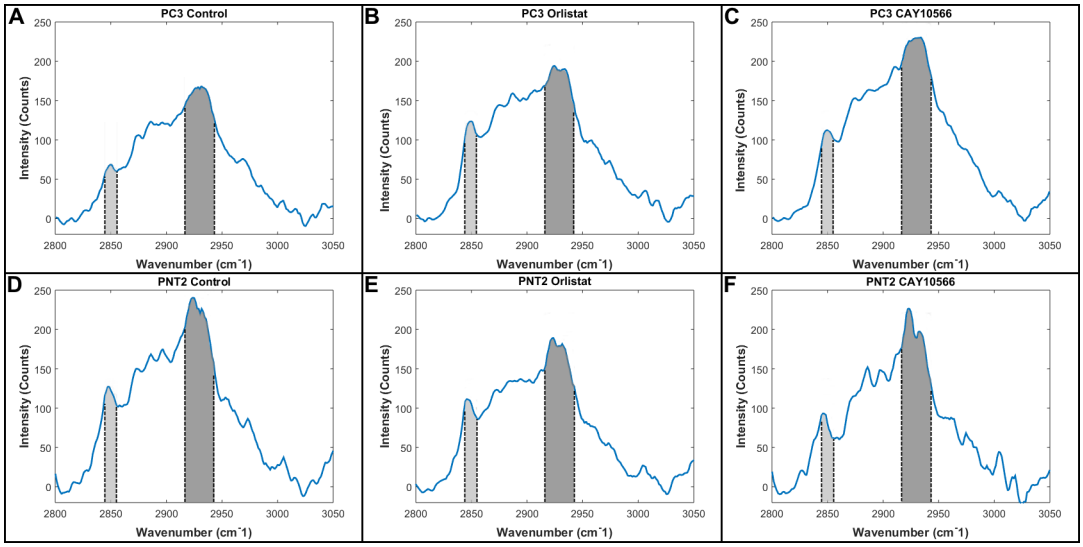

Figure 4.1: Representative averaged Raman spectra for cells in microfluidic devices. A) PC3 cell treated with DMSO for 48 hours. B) PC3 cell treated with 100 µM Orlistat for 48 hours. C) PC3 cell treated with 50 nM CAY10566. D) PNT2 cell treated with DMSO for 48 hours. E) PNT2 cell treated with 100 µM Orlistat for 48 hours. F) PNT2cell treated with 50 nM CAY10566. Spectra chosen for having L/P ratios close to the weighted average mean for all cells in each condition.

For PC3 cells, an unpaired t-test showed this increase to be statistically significant with $p < 0.0001$, however, for PNT2 cells the P value was 0.263, which indicates that the increase is not statistically significant (table 4.1). The L/P ratio for PC3 cells increased by 0.018 from 0.513 ± 0.074 to 0.531 ± 0.101, while PNT2 cells were found to have a decrease of 0.042 from 0.481 ± 0.130 to 0.439 ± 0.137 when CAY10566 was added. For both PC3 and PNT2 cells, unpaired t-tests showed that these differences were not be statistically significant, with p-values of 0.505 and 0.361 respectively (table 4.2).

Table 4.1: L/P ratios for cells in devices when under control conditions, when treated with 100 µM Orlistat, the increase in L/P ratio between control and Orlistat conditions and the associated p-value indicating the significance of the increase. Errors for L/P ratios are standard deviations, while errors for the L/P ratio differences are standard errors.

Cell Type	**Control L/P Ratio**	**Orlistat L/P Ratio**	**Difference**	**P-Value**
PC3	0.513±0.074	0.714±0.086	0.201±0.019	<0.0001
PNT2	0.481±0.130	0.517±0.123	0.036±0.032	0.263

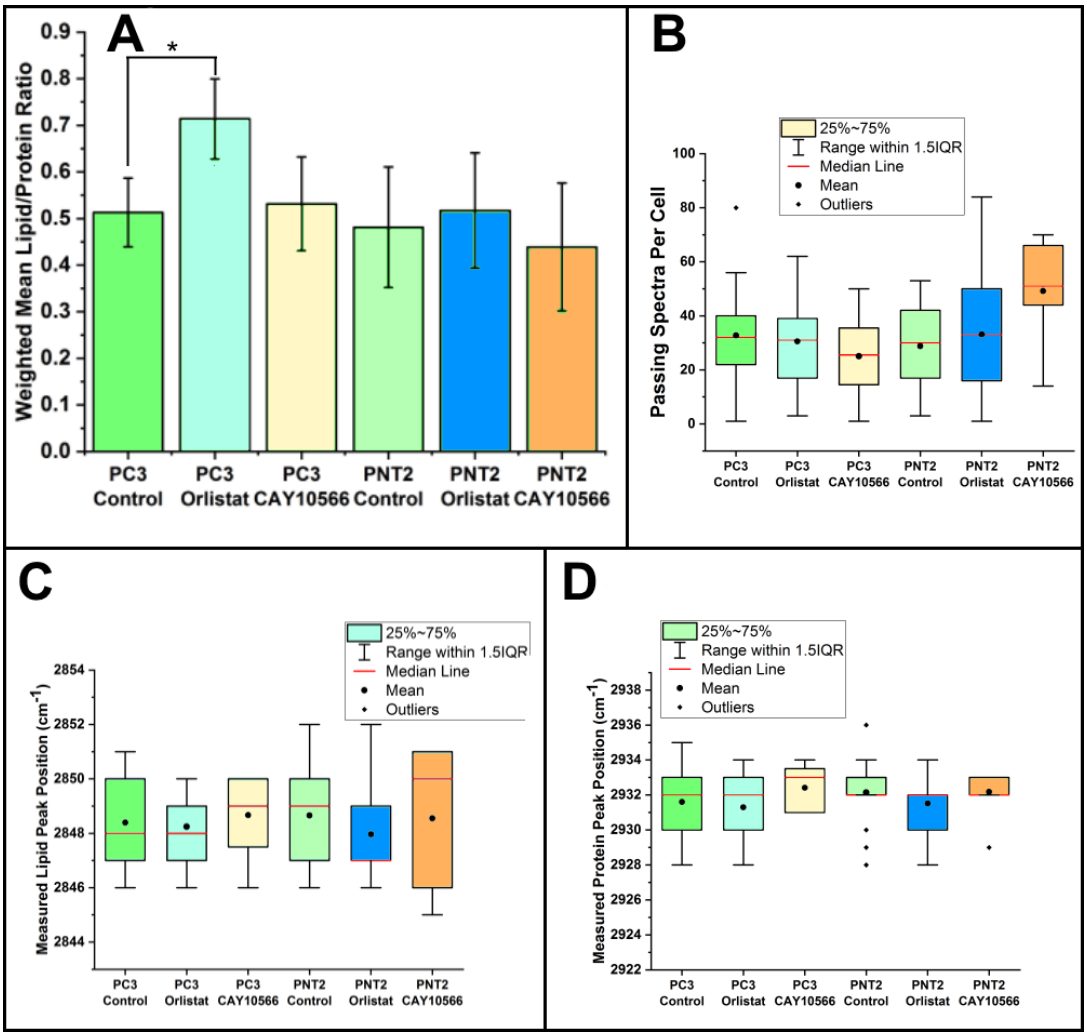

Figure 4.2: Analysis of spectroscopic data for cells in microfluidic devices. A) Weighted mean L/P ratios for each condition, combined from three separate repeats and with standard deviation error bars of all pooled cells. B) Average number of spectra per cell that passed thresholding in the MATLAB script per condition. C) Average protein peak wavenumber as detected by the MATLAB script per condition. D) Average lipid peak wavenumber as detected by the MATLAB script per condition. * indicates a statistical significance of $p < 0.0001$. All data has been pooled from three replicates with the exception of CAY10566 for which only one replicate was used. The total number of cells analysed for each condition are; PC3 control: 38, PC3 Orlistat: 37, PC3 CAY10566: 12, PNT2 Control: 35, PNT2 Orlistat: 29, PNT2 CAY10566: 11.

Table 4.2: L/P ratios for cells in devices when under control conditions, when treated with 50nM CAY10566, the increase in L/P ratio between control and CAY10566 conditions and the associated p-value indicating the significance of the difference. Errors for L/P ratios are standard deviations, while errors for the L/P ratio differences are standard errors.

Cell Type	**Control L/P Ratio**	**CAY10566 L/P Ratio**	**Difference**	**P-Value**
PC3	0.513±0.074	0.531±0.101	0.018±0.027	0.505
PNT2	0.481±0.130	0.439±0.137	-0.042±0.045	0.361

Cells across most conditions show a similar mean number of spectra (around 20-40 spectra per cell) that passed thresholding in the MATLAB analysis script (figure 4.2.B). PNT2 cells treated with CAY10566 had a slightly higher mean value at 49 spectra per cell. All conditions do show a large interquartile range. This is partly owed to variability in the sizes of the cells being imaged, but also to a large cell to cell variability in signal intensity. The wavenumbers at which the lipid peaks have been measured are consistent across all conditions, with mean values for each condition between 2848 cm^{-1} and 2849 cm^{-1} (figure 4.2.C). Interquartile ranges stretch between 2846 cm^{-1} and 2851 cm^{-1}, while there is a total range of 7 cm^{-1} in which this peak has been detected. The wavenumbers at which the protein peaks have been measured are also consistent across all conditions, with mean values for each condition between 2931 cm^{-1} or 2932 cm^{-1} (figure 4.2.D). Interquartile ranges stretch between 2930 cm^{-1} and 2933 cm^{-1}, while there is a total range of 7 cm^{-1} in which this peak has been detected (excluding outliers). The Raman spectrometer had a spectral resolution of 1.3 cm^{-1}, which could account to some of the variation in peak positions, however it is possible that some variation could be due to influence from other molecules or systematic errors relating to the Raman spectrometer or a combination of these.

4.2.2 Viability

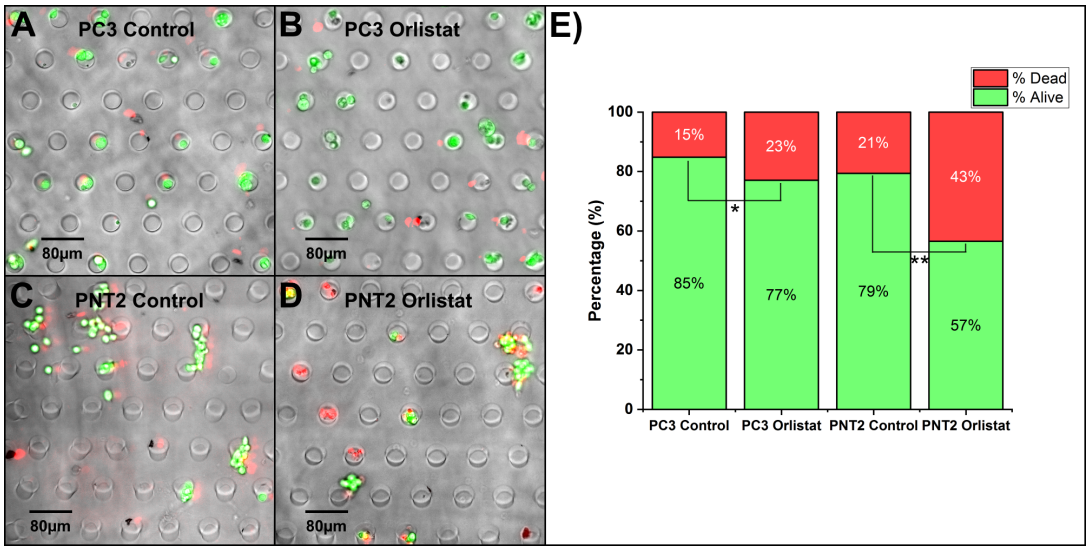

Figure 4.3: Viability of cells trapped in microfluidic devices treated with either DMSO or 100 µM Orlistat. Representative fluorescence images of A) PC3 cells treated with DMSO for 48 hours, B) PC3 cells treated with 100 µM Orlistat for 48 hours, C) PNT2 cells treated with DMSO for 48 hours and D) PNT2 cells treated with 100 µM Orlistat for 48 hours. Green fluorescence stain indicates that the cells were viable prior to staining, whereas red stain indicates that cells were already dead. E) Percentage of cells found to be viable per condition. Statistical significance: * $p = 0.035$, ** $p < 0.0001$. Number of cells analysed for each condition are; PC3 Control: 204, PC3 Orlistat: 366, PNT2 Control: 272, PNT2 Orlistat: 253

The effect that 100 µM Orlistat has on the viability of both PC3 and PNT2 cells in devices was investigated. As with spectroscopic studies, PC3 and PNT2 cells were loaded into devices and incubated for 24 hours before being treated with either 100 µM Orlistat or cell culture media containing 0.25% DMSO and incubated for a further 48 hours. Following this, and prior to fixing with PFA, cells were treated with the fluorescent viability stains calcein and EthD. Fluorescence images were then taken of the cells, and live/dead counts were performed across three cell trap arrays (figure 4.3.A-D). For PC3 cells, a decrease in viability from 85% to 77% was found when the cells had been treated with orlistat (figure 4.9.E). Hypothesis testing using Fisher's exact test for two proportions returned a P value of 0.035 indicating that this drop is statistically significant.

For PNT2 cells viability decreased from 79% to 57% with a corresponding P value of <0.0001 indicating statistical significance. These results suggest that orlistat has a greater impact on the viability of the non-cancerous PNT2 cells than it does on the cancerous PC3 cells, a result that is unexpected since orlistat should only impact the metabolism of cancerous cells. Due to time constraints, this experiment was only performed once, and this result may have been due to some external factor such as contamination within the channel. A number of cells can be seen to be present in the devices outside of the traps (figure 4.3.A-D). This is potentially an indication that the channel height may not be optimal, perhaps due to some deformation during the thermal bonding process, causing cells to become stuck outwith the traps. This should be investigated in future iterations of the device by increasing the height of the features during the photolithography stage.

4.2.3 Multiple Drug Concentrations

In order to demonstrate the potential of using the microfluidic device to test multiple conditions at once, an orlistat concentration test was performed. PC3 cells were seeded into four channels of one device and incubated for 24 hours. Media containing either 0.5% DMSO (control), 50 µM orlistat, 100 µM orlistat or 200 µM orlistat was added to the channels and the device was incubated for a further 48 hours. In this instance a higher amount of DMSO was used as a control than in other experiments. This is the equivalent amount of DMSO to the strongest orlistat concentration in this experiment. The drug-containing media were washed out of the channels with PBS and the cells were fixed with 4%PFA for 30 minutes. The PFA was washed out with PBS and individual cells were mapped with Raman spectroscopy.

Spectra were pre-processed and analysed using the same methods as previous experiments to obtain average L/P ratios for each cell. The ratios from each condition were then averaged to produce a weighted mean L/P ratio for each concentration (figure 4.4). As expected, an overall increase was observed from the control condition to the 200 µM orlistat condition ($p < 0.0001$).

The weighted mean value for 100 µM orlistat is lower than expected compared to other conditions and to previous experiments. It is not statistically significant compared to the control ($p = 0.8$) and has a larger standard deviation than the other concentrations. It is possible that this could be due to a reduced number of analysed cells per condition (n=8) as well as this experiment not being repeated leading to a reduction in the accuracy of the mean values calculated. Although a significant result was anticipated for the 100 µM condition, these results demonstrate that the device is capable of studying multiple concentrations of drugs whereas previous studies using Raman spectroscopy have so far only looked at a single Orlistat concentration of 100 µM [10].

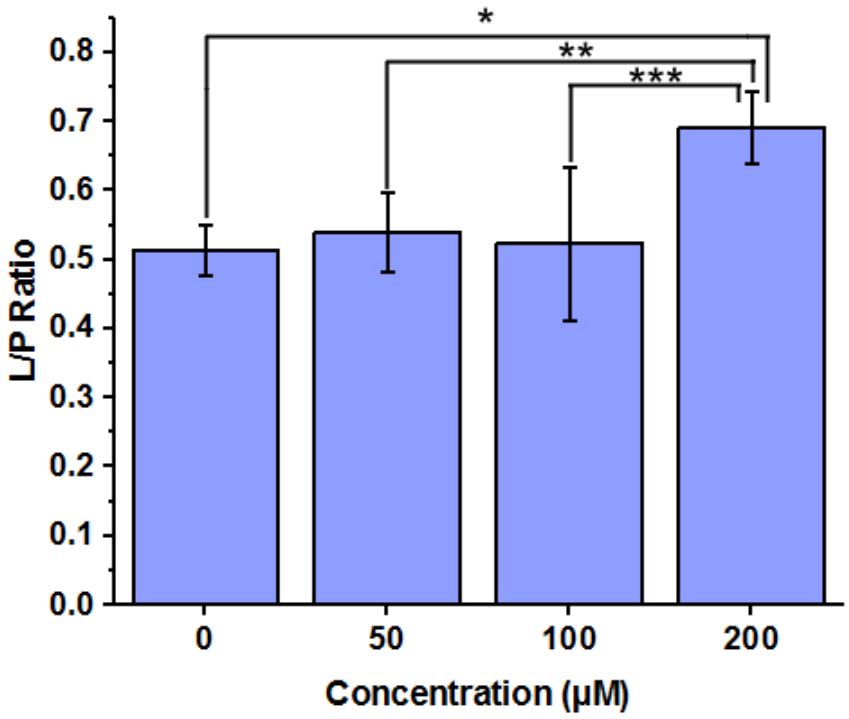

Figure 4.4: Weighted Mean L/P ratios of PC3 cells treated with multiple concentrations of Orlistat. Error bars show standard deviations of results for each condition. Number of cells analysed for each condition; Control: 8, 50 µM: 6, 100 µM: 8, 200 µM: 7. Statistical significance: * $p < 0.0001$, ** $p =$*0.0004, *** $p = 0.003$.

4.2.4 Trapping efficiency

Images of trap arrays from several experiments were collated and analysed to estimate the trapping efficiency of cells within the device. Ideally, the majority of traps would contain a single cell, however in practice, many are found to be empty and some are found to contain multiple cells (figure 4.5). When all 23 measured arrays were combined, 11.2% of cells were found to contain single cells, 8.2% of traps were found to contain multiple cells and the remaining 80.6% of traps were found to be empty. While this is far from ideal, a sufficient number of cells were trapped to perform preliminary Raman mapping studies. Trapping efficiency could be further improved by reducing the size of the cell traps to prevent multiple cells from occupying the same trap, and by seeding more cells in the device to further fill the traps. Additionally, many cells were found to have become stuck in the channels outwith the trap arrays (visible in figure 4.3.A-D.). Analysis of 817 PC3 cells revealed that approximately 49% of the cells appeared to be immobilised outside of the cell traps. These cells were counted from within the area of the trap arrays only. This suggests that either the channels are not sufficiently high enough (approximately 45 µm) to allow the passage of the cells or that the channels are still deforming during the bonding process leading to a decrease in channel height in the finished devices. Further iterations of the device should be made with deeper channels (50 µm or higher) in order to negate this effect.

4.2.5 CARS Imaging

Fixed PC3 cells in PBS-filled devices were imaged using CARS (Figure 4.6). Lasers were set to an energy difference of 2851 cm^{-1} to image cellular lipids (figure 4.6.A) and 2930 cm^{-1} to image cellular proteins (figure 4.6.B).

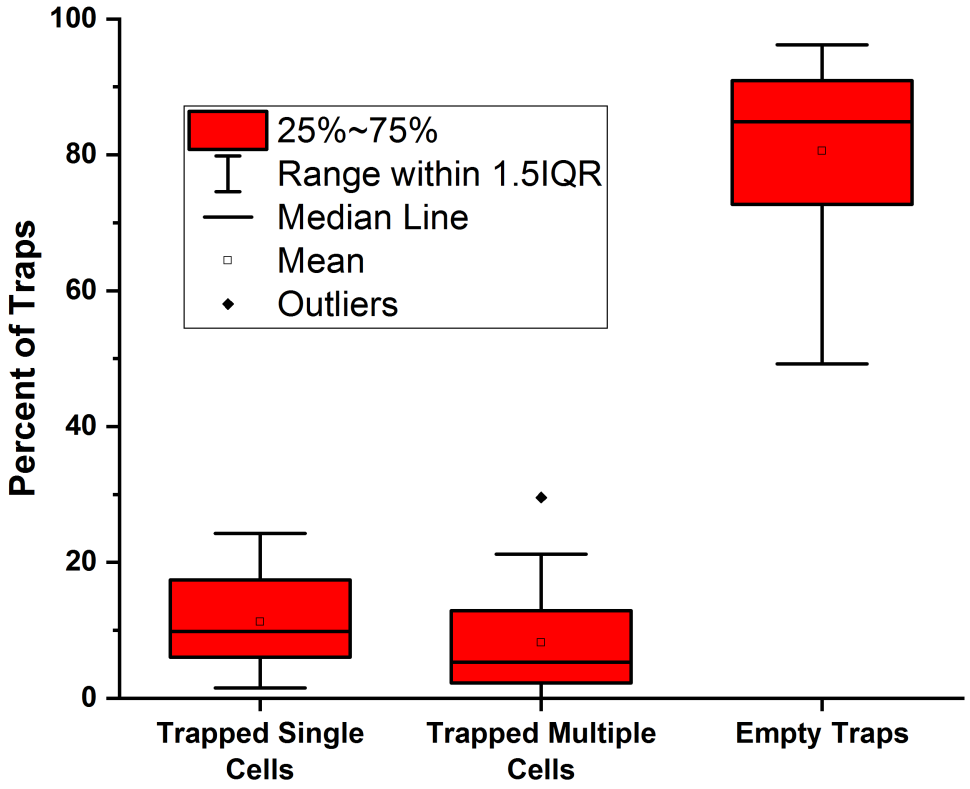

Figure 4.5: Device trapping efficiency. Data collected from 23 imaged trap arrays (n = 3036). Boxplots show variation in the percentages of traps within each imaged array that contained a single cell, multiple cells or were empty.

Signal from the cells was largely obscured by background within the traps, presumably coming from the surrounding PBS. This signal could also be seen within the channels of the device, but this is not visible in figure 4.6 as out of focus light is blocked by the pinhole of the imaging system. This is unexpected as PBS should not have a strong Raman signal at these wavelengths and did not cause issues when used with Raman mapping experiments. PBS was in fact used as a substitute for cell culture media when imaging in Raman mapping experiments because it produced a significantly reduced background. Further investigation is required to understand why PBS was producing such a strong background with CARS but not with Raman mapping.

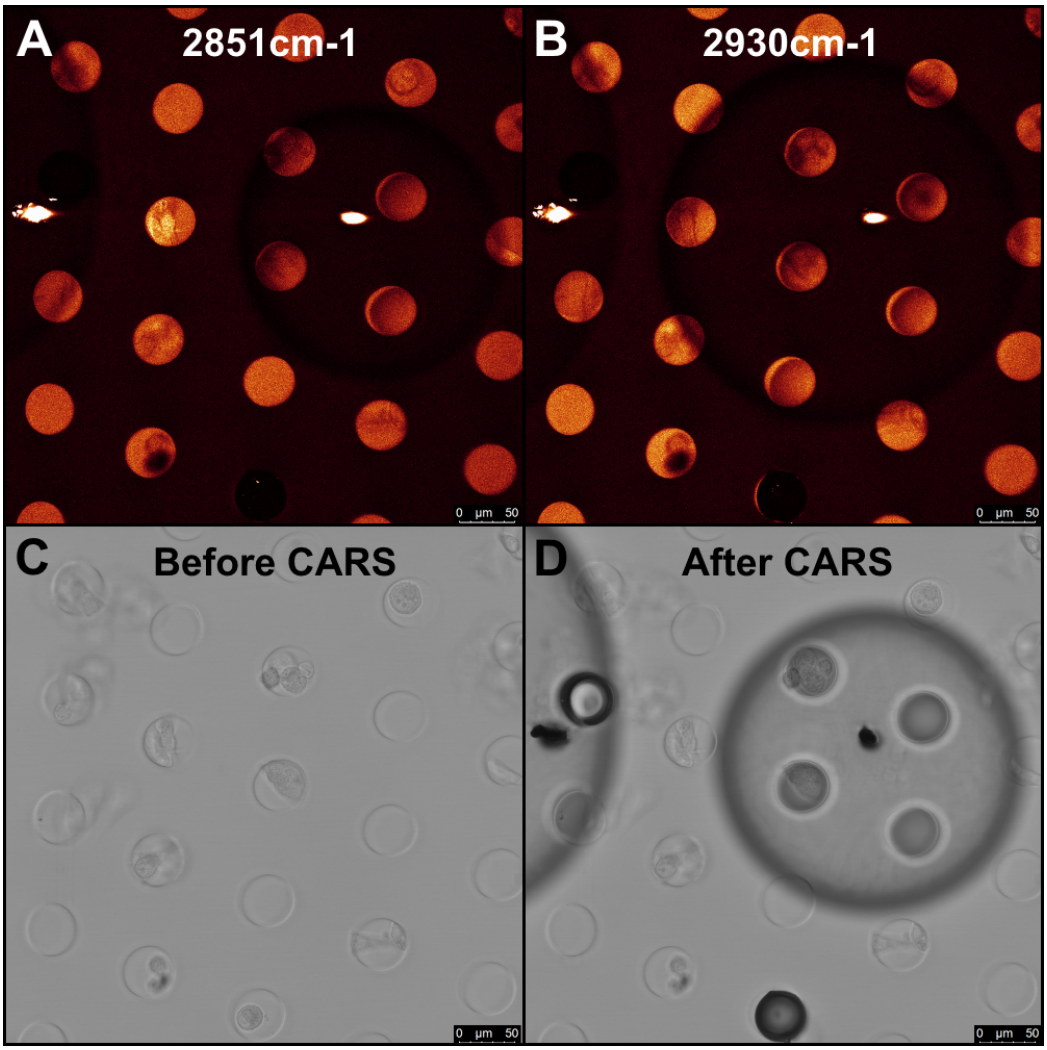

Figure 4.6: CARS imaging of device filled with PBS and PC3 cells. A) CARS image taken at 2851 cm^{-1} (lipid peak). B) CARS image taken at 2930 cm^{-1} (protein peak). C) Brightfield image taken before CARS imaging. D) Brightfield image taken in the same field of view after CARS imaging, showing large air bubbles formed by the CARS laser.

This background signal severely impedes the results, and as such useful quantitative analysis cannot be performed. Additionally, large air bubbles formed in the device during imaging (figure 4.6.C-D). Absolutely no air was present in the channels prior to imaging, and it appears that these air bubbles were produced by heating from the CARS laser. It was concluded due to the poor signal to noise ratio and the nucleation of air bubbles that CARS may be an unsuitable imaging method for measuring cellular lipid composition in the devices.

4.3 Glass Bottomed Dishes and Coverslips

In order to provide a comparison to aid in the evaluation of the microfluidic device, experiments were conducted using cells fixed to either glass bottomed dishes or glass coverslips.

4.3.1 Raman Spectroscopy

PC3 and PNT2 cells at concentrations of $1x10^5$ cells/mL were incubated with 100 µM orlistat for 48 hours and fixed with PFA in either glass bottomed dishes or on glass coverslips. These cells were prepared at a lower concentration than those used in microfluidic devices to avoid large clusters of cells on the substrate as analysis of single cells is required. All other aspects of cell preparation was identical to those used in microfluidics prior to incubation in the dishes/coverslips. These cells were then imaged with Raman spectroscopy to measure their L/P ratio. Since the Orlistat used was dissolved in DMSO, an equivalent amount of DMSO was added to cell samples to be used as a control. This ensured that the only difference between the drug treated cell samples and the control cell samples was the addition of Orlistat.
Individual cells were mapped with Raman spectroscopy by taking spectra at 3 µm intervals in both x and y. This was repeated for at least 10 cells per condition and the experiment was repeated three times. Spectral data for each map was then pre-processed using Renishaw Wire software and then analysed in MATLAB using the script described in section 4.2.

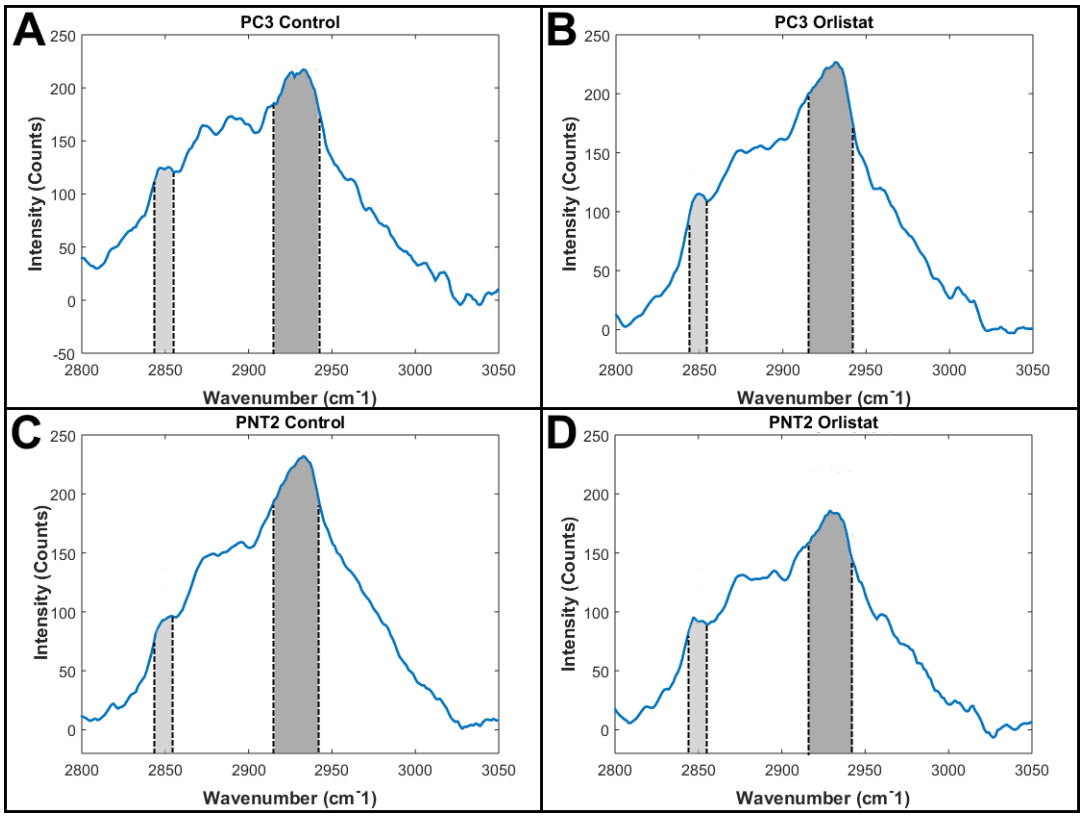

Figure 4.7: Representative averaged Raman spectra from cells fixed to either glass bottomed dishes or glass coverslips. A) PC3 cell treated with DMSO for 48 hours. B) PC3 cell treated with 100 µM Orlistat for 48 hours. C) PNT2 cell treated with DMSO for 48 hours. D) PNT2 cell treated with 100 µM Orlistat for 48 hours.

This generated an averaged spectrum for each mapped cell (figure 4.7) from which its L/P ratio was calculated.

Data from all three repeats were pooled for statistical analysis. The L/P ratios from each individually analysed cell were averaged to produce a weighted mean value for each condition, using the number of spectra per cell which passed thresholding in the analysis script as weights. This reveals an overall increase in the L/P ratio for both PC3 cells and PNT2 cells when treated with Orlistat (figure 4.8.A). This trend for the ratios to increase when treated with Orlistat is consistent with the findings of Jamieson *et al.* [10] and the findings with microfluidic devices. The L/P ratio for PC3 cells increased by 0.122 from 0.484 ± 0.071 to 0.606 ± 0.077, while PNT2 cells were found to have an increase of 0.100 from 0.393 ± 0.052 to 0.493 ± 0.088.

For both PC3 and PNT2 cells, unpaired t-tests showed these increases to be statistically significant with $p < 0.0001$ (table 4.3).

Table 4.3: L/P ratios for cells fixed to glass slides or glass coverslips when under control conditions, when treated with 100 µM Orlistat, the increase in L/P ratio between control and Orlistat conditions and the associated p-value indicating the significance of the increase. Errors for L/P ratios are standard deviations, while errors for the L/P ratio differences are standard errors.

Cell Type	**Control L/P Ratio**	**Orlistat L/P Ratio**	**Difference**	**p-Value**
PC3	0.484 ± 0.071	0.606 ± 0.077	0.122 ± 0.019	<0.0001
PNT2	0.393 ± 0.052	0.493 ± 0.088	0.100 ± 0.019	<0.0001

Cells across all conditions show a similar mean number of spectra (around 40-50 spectra per cell) that passed thresholding in the MATLAB analysis script (figure 4.8.B). All conditions do show a large interquartile range. This is partly owed to variability in the sizes of the cells being imaged, but also to a large cell to cell variability in signal intensity. The wavenumbers at which the protein peaks have been measured are consistent across all conditions, with mean values for each condition at either 2931 cm^{-1} or 2933 cm^{-1} (figure 4.8.C). Interquartile ranges stretch between 2929 cm^{-1} and 2936 cm^{-1}, giving a total range of 7 cm^{-1} in which this peak has been detected. The wavenumbers at which the lipid peaks have been measured are also consistent across all conditions, with mean values for each condition at either 2849 cm^{-1} or 2850 cm^{-1} (figure 4.8.D). Interquartile ranges stretch between 2846 cm^{-1} and 2854 cm^{-1}, giving a total range of 8 cm^{-1} in which this peak has been detected.

4.3.2 Viability Staining

The effect that 100 µM Orlistat has on the viability of both PC3 and PNT2 cells was investigated. As with spectroscopic studies, PC3 and PNT2 cells were cultured on glass coverslips and incubated for 48 hours with either 100 µM Orlistat or the equivalent amount of DMSO. Following this, and prior to fixing with PFA, cells were treated with the fluorescent viability stains calcein and ethidium homodimer (EthD). Fluorescence images were then taken of the cells, and live/dead counts were performed across three fields of view (figure 4.9.A-D).

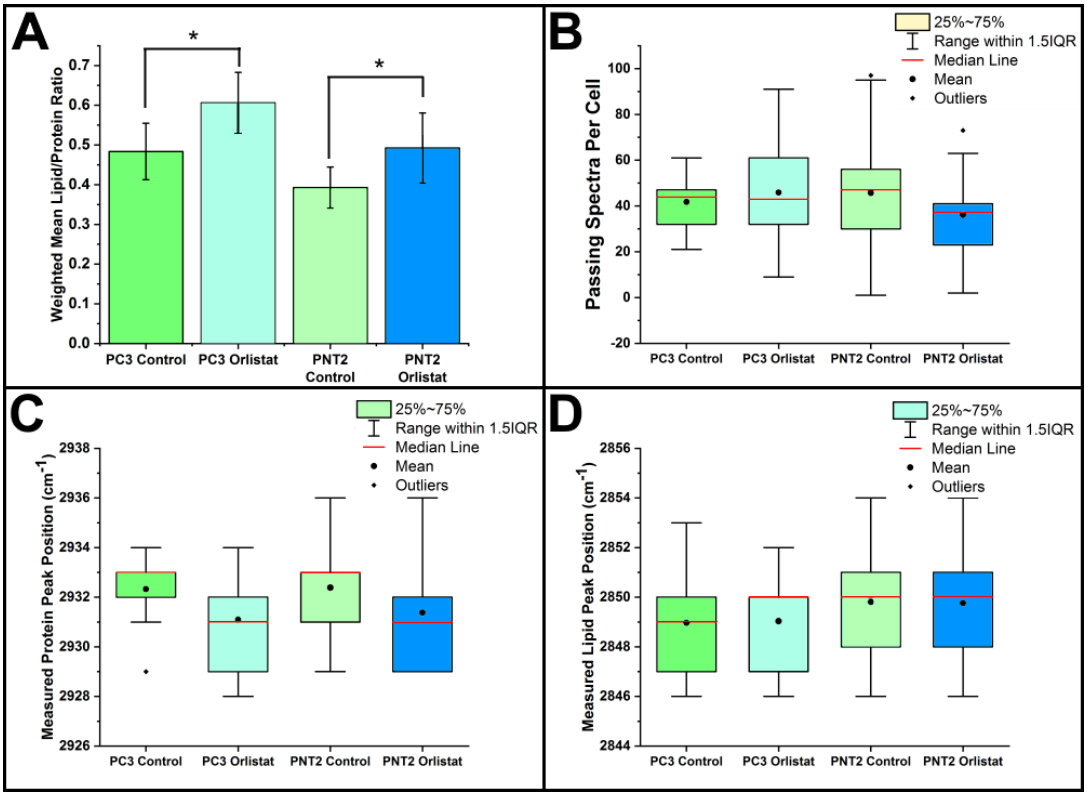

Figure 4.8: Analysis of spectroscopic data for cells fixed to glass bottomed dishes or glass coverslips. A) Weighted mean L/P ratios for each condition pooled from three separate repeats and with weighted standard deviation error bars. B) Average number of spectra per cell that passed thresholding in the MATLAB script per condition. C) Average protein peak wavenumber as detected by the MATLAB script per condition. D) Average lipid peak wavenumber as detected by the MATLAB script per condition. Stars indicate a statistically significant result difference to the relative control condition. Number of cells analysed per condition; PC3 Control: 31, PC3 Orlistat: 31, PNT2 Control: 31, PNT2 Orlistat: 29. Means and standard deviations calculated from all pooled cells from each condition. Statistical significance: * $p < 0.0001$.

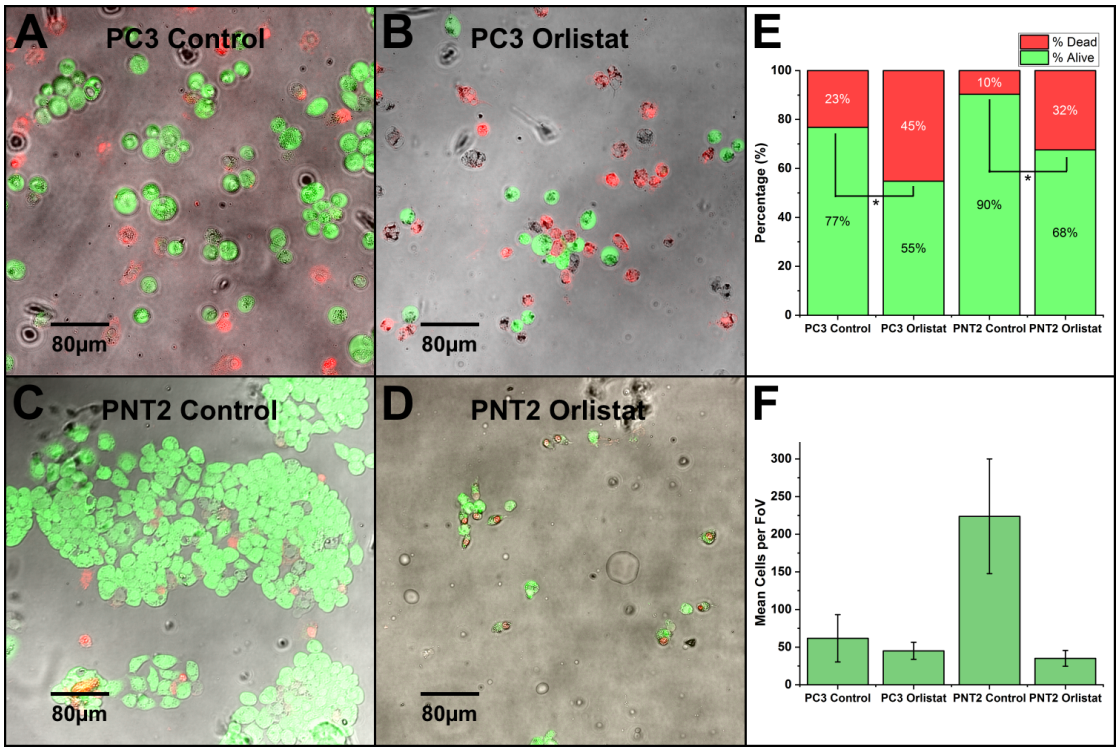

Figure 4.9: Viability of cells fixed to glass coverslips. Representative fluorescence images of A) PC3 cells treated with DMSO for 48 hours, B) PC3 cells treated with 100 µM Orlistat for 48 hours, C) PNT2 cells treated with DMSO for 48 hours and D) PNT2 cells treated with 100 µM Orlistat for 48 hours. Green fluorescence stain indicates that the cells were viable prior to staining, whereas red stain indicates that cells were already dead. E) Percentage of cells found to be viable per condition. F) Mean number of cells imaged in each field of view with standard deviation error bars. Statistical significance: * $p < 0.0001$. Three fields of view imaged per condition. Total cells analysed; PC3 Control: 185, PC3 Orlistat: 135, PNT2 Control: 671, PNT2 Orlistat: 105.

Significant drops were observed in the percentage of viable cells when treated with orlistat compared to the control (figure 4.9.E). For PC3 cells this drop is from 77% viability to 55% viability. For PNT2 cells this drop is from 90% viability to 68% viability. For both PC3 and PNT2 cells, hypothesis testing using Fisher's exact test for two proportions gave p-values < 0.0001 indicating that these drops are statistically significant. On top of this, a considerable drop in the number of cells imaged in each field of view is also noted when orlistat is added (figure 4.9.F) for PNT2 cells.

This is likely due to dead cells dissociating from the glass coverslips and being removed during wash steps, indicating that orlistat has a larger impact on viability than that measured by looking at the live/dead percentages alone. This data is derived from only one single experiment, and repeats are required to solidify the results. While it has been noted that there was a notably lower number of cells per field of view for PNT2 cells treated with Orlistat, no measurements of confluence were taken prior to the addition of Orlistat. Cell viability was not found to be impacted by Orlistat when similar experiments were carried out by Jamieson *et al.* [10] against both PC3 and PNT2 cell lines. This suggests that the loss of viability may have been due to an additional factor.

4.4 Comparison of Device and Coverslips

A significant ($p < 0.0001$) increase in the L/P ratio of PC3 cells when treated with 100 µM Orlistat was observed in both glass coverslips and FEP microfluidic devices (Figure 4.10). This increase was found to be larger when measured in devices than for cells on glass coverslips or glass bottomed dishes. A significant ($p < 0.0001$) increase in L/P ratio was also found for PNT2 cells on coverslips and glass bottomed dishes, however this was not reflected in the microfluidic device ($p = 0.263$). The standard deviations in the values calculated for the devices were larger for PNT2 cells, suggesting that they are less accurate than those for glass dishes and coverslips. This reduction in accuracy may be why a significant difference could be found for glass dishes and coverslips, but not in the devices.

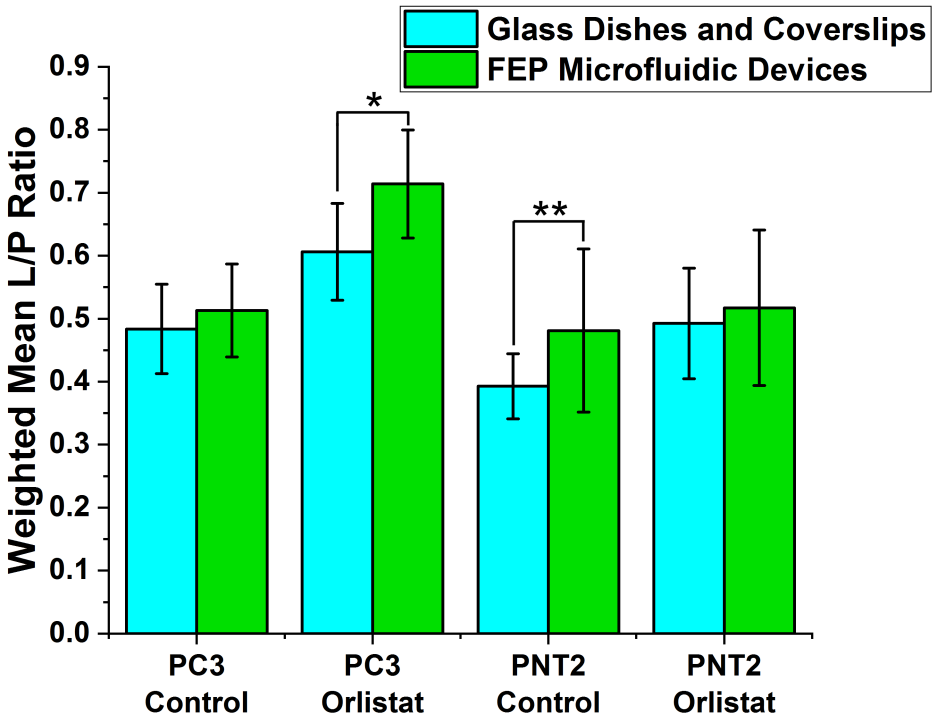

Figure 4.10: Comparison of weighted mean L/P ratios measured from spectra of PC3 and PNT2 cells treated with either DMSO or 100 µM Orlistat for both microfluidic devices and glass bottomed dishes/coverslips. Statistical significance: * $p < 0.0001$, ** $p = 0.0008$. Error bars are weighted standard deviations for all pooled cells analysed per condition. Number of cells analysed for each condition: PC3 control Devices: 38, PC3 Control Coverslips: 31, PC3 Orlistat Devices: 37, PC3 Orlistat Coverslips: 31, PNT2 Control Devices: 35, PNT2 Control Coverslips: 31, PNT2 Orlistat Devices: 29, PNT2 Orlistat Coverslips: 29. All conditions repeated three times and data from each repeat was pooled for analysis.

Overall Raman signals tended to be less intense for cells imaged in devices compared to cells on glass bottomed dishes and coverslips (figures 4.7 and 4.1). This was especially true for PNT2 cells, which tend to be smaller than PC3 cells. This is possibly due to background signal from the PBS that they are immersed in, which was not present on the coverslips or glass-bottomed dishes. While the PBS background was low enough to be easily removed during pre-processing, this reduction in intensity led to a lower average number of spectra per cell that passed thresholding in the analysis script (figures 4.8.B and 4.2.B). This also led to an increase in the number of mapped cells in which no spectra passed thresholding (these were removed from statistical analysis) and is a likely contributor to the larger standard deviations associated with the PNT2 L/P ratios.

Weighted mean L/P ratios for microfluidic devices tend to be slightly higher than those measured from cells on glass bottomed dishes and coverslips (figure 4.10, table 4.4). Unpaired t-tests reveal statistically significant differences for PC3 orlistat and PNT2 control conditions, with p-values of < 0.0001 and 0.0008 respectively. This could suggest that PC3 cells may be affected more by orlistat when treated in the devices as opposed to when they are on glass, however it is more likely that this is due to the higher background found from the PBS in the microfluidic devices and the manipulation of the data to remove it. The data nethertheless shows increases in the L/P ratios for both PC3 cells fixed to glass and PC3 cells in microfluidic devices when treated with orlistat.

Table 4.4: Comparison of L/P ratios measured from cells on glass bottomed dishes/coverslips and cells in FEP microfluidic devices under each condition.

Condition	**Coverslips L/P Ratio**	**Devices L/P Ratio**	**P-Value**
PC3 Control	0.484±0.071	0.513±0.074	0.104
PC3 Orlistat	0.606±0.077	0.714±0.086	<0.0001
PNT2 Control	0.393±0.052	0.481±0.130	0.0008
PNT2 Orlistat	0.493±0.088	0.517±0.123	0.396

Jamieson *et al.* also found statistically significant increases for both PC3 ($p < 0.001$) and PNT2 ($p < 0.001$) cells when treated with orlistat compared to the DMSO control [10]. Ratios were calculated here using a slightly different method and so exact values are not directly comparable, however the data found from microfluidic experiments with PC3 cells and from coverslips with both PC3 and PNT2 cells match with the Jamieson *et al.*'s findings. Additionally, Jameison *et al.* did not find a significant difference between control PC3 cells and PC3 cells treated with CAY10566. This finding is consistent with the findings from this thesis, however a significant difference ($p = 0.0003$) was also found for PNT2 cells treated with CAY10566, a result which was not mirrored here.

Live/Dead staining with calcein and EthD demonstrated a drop in viability for both PC3 and PNT2 cells when treated with orlistat on glass bottomed dishes and coverslips (figure 4.9.E). The accuracy of these results were called into question when it was observed that there was a considerable drop in the confluence, especially for PNT2 cells (figure 4.9.F). Since cells adhered to a surface will dissociate from that surface when they die, many non-viable cells will be removed during the wash steps involved in staining and fixing. This means that fluorescence counts are not an accurate measurement of viability in this case.

In the microfluidic devices however, cells are not adhered to a surface, but are instead immobilised within the cell traps. This means that the cells should remain in the device regardless of their viability during wash steps, although further investigation is required to verify this. This has both advantages and disadvantages depending on the application. In terms of viability staining it is advantageous as a far more accurate live/dead count can be performed. In terms of Raman mapping to measure lipid the content of cells, it is preferable to image only cells which remained viable up to the point of fixing with PFA. It is difficult to accurately determine the viability of the cells in the devices without staining them, and fluorescence stains contain numerous CH bonds which will affect the Raman spectrum between 2800-3000 cm^{-1}. It is possible that imaging a greater mixture of cells which were alive and cells which were dead at the point of fixing with PFA could lead to a greater variability in L/P ratio results.

Despite this, PC3 cells were found to have an increased viability in microfluidic devices compared to glass bottomed dishes and coverslips for both control and 100 µM orlistat conditions (figure 4.3.E). Viability was lower for both PNT2 conditions however, with an especially large drop for the 100 µM orlistat condition. It is possible that this increased mixture of viable and non-viable cells could be a further contributor to the increased standard deviations found in the L/P ratios of PNT2 cells in microfluidic devices.

Statistical significance of the viability results is limited as only one run of each condition was performed. Ideally, to check the consistency of how each condition affected viability, these conditions would have been run in triplicate. These results do however demonstrate that both PC3 and PNT2 cells can remain viable in the devices for the duration of the experiments being performed.

4.5 Chapter Summary

In this chapter, cancerous PC3 cells and non-cancerous PNT2 cells were seeded into either FEP microfluidic devices or glass bottomed dishes or coverslips. After 24 hours incubation, cells were then treated with media containing either 100 µM orlistat or 0.5% DMSO. These cells were then incubated for a further 48 hours before having this media washed off and being fixed with PFA.

Raman mapping revealed a significant increase in the L/P ratios of PC3 cells when treated with orlistat for both devices and glass bottomed dishes and coverslips. A significant increase was also found for PNT2 cells on glass bottomed dishes and coverslips, but this was not reflected in the microfluidic devices.

A single experiment was performed with CAY10566 in devices for comparison with orlistat. Neither PC3 nor PNT2 cells experienced a significant difference with respect to the control condition.

Viability staining found a decrease in viable PC3 and PNT2 cells when orlistat was added to both devices and glass bottomed dishes and coverslips. In devices, this decrease was more prominent for PNT2 cells, whereas it was more prominent for PC3 cells in glass bottomed dishes and coverslips.

PC3 cells all seeded in one device were treated with three concentrations of orlistat as well as a control medium. An overall increase in the L/P ratio was found as the concentration of orlistat was increased.

PC3 cells seeded in a device were imaged using CARS. The PBS in the device produced a considerable amount of background signal, severely limiting the amount of information that could be collected from the cells. Additionally, large air bubbles nucleated within the device, likely due to the pulsed laser. This suggests that CARS is not a suitable imaging methodology for this device.

Chapter 5.

Discussion and Conclusions

5.1 FEP as a Material for Microfluidics

After PDMS was determined to be an unsuitable material for this project, FEP was selected as an alternative due to the lack of CH bonds. A paper by Ren *et al.* presented methods for the creation of FEP-based microfluidic devices [88]. While Ren *et al.* presented methods for creating both PFA and FEP microfluidic devices, most of the results presented were from PFA-based devices and the paper contained little discussion of FEP ones. The literature contains few examples of Teflon based microfluidic chips, and many of these either use PFA [89, 134] or use Teflon as a coating on glass [135]. A recent paper, published after the conclusion of this project, used another Teflon, perflouropolyether (PFPE), to create microfluidic chips for processing organic solvents [136]. FEP-based microfluidic devices have been shown to be compatible with a polydopamine coating for immunoassays and cell culture [94], although this paper was a generalised proof-of-concept rather than being targeted towards a specific biological application. FEP has also been used to create micro-capillaries for ultraviolet irradiation of virus particles [137], however these capillaries were created by methods vastly different to those described by Ren *et al.* and used within this project. While still in a proof-of-concept phase, this thesis presents one of the first attempts to create an FEP-based microfluidic device tailored towards a very specific biological application rather than reporting very generalised potential applications. As such, a discussion of the suitability of the material for such applications is relevant.

A number of difficulties were encountered when trying to replicate the methods presented by Ren *et al.*, as described throughout chapter 3. When heat treating the PDMS stamps with the recommended 5:1 prepolymer to curing agent ratio (by using 2x the usual amount of curing agent for a 10:1 ratio), the stamps formed large cracks and became unusable.

This continued to happen even when the temperature was slowly ramped down in 5°C steps. According to Ren *et al.*, it is important to use a low prepolymer to curing agent ratio in order to create a hard enough stamp for hot embossing of Teflon and that the heat treatment is essential to de-gas the stamp prior to use [88]. In order to get around this problem, a prepolymer to curing agent ratio of 6.7:1 was used (i.e. 1.5x the usual amount of curing agent compared to the manufacturer's recommended 10:1 ratio). This prevented cracks from forming, however the stamps were unlikely to be as hard as those described by Ren *et al.*. It is unclear as to why the heat treatment of the 5:1 ratio stamp failed as no discussion of issues relating to this process is described by Ren *et al.*, however the PDMS used by Ren *et al.* was from a different supplier which may have contributed to a difference in the crosslinking at this ratio.

The softer stamp may have contributed to deformations that occurred when the stamps were first used to hot emboss FEP (Section 3.6). Another identified factor was likely the different thermal expansion coefficients of the stamp and the FEP. This was overcome by altering the hot embossing protocol such that the sample is not put under pressure until after it has heated. While this led to a vast improvement, some deformations still persisted when creating the 40 µm diameter cell traps. Ren *et al.* demonstrated micropatterning of features down to 150 nm [88], however no information was provided as to the height of these features, a factor which is likely to impact on the achievable lateral resolution.

The approach to bonding the devices was slightly different to that described in the literature, but works on the same principle of thermal expansion. Ren *et al.* used a finger tight steel screw clamp to hold the layers of FEP in place while heating to 260°C. Thermal expansion of the FEP layers then provided sufficient pressure to bond the layers together [88]. In this thesis, a similar method was developed that used the same thermal press as for hot embossing, using two layers of PDMS to sandwich the device layers and provide pressure from thermal expansion (section 3.7). Since the layers of the device required precise alignment, special 1mm diameter features were included in the design. These were punched out and the layers were pegged together with blunted needles to prevent them from sliding during the bonding process.

A further problem was encountered whereby the relatively large cell trap chamber was found to collapse during the bonding process due to the pressure being too high. Initially, a redesign of the device was attempted with pillars to hold up the chamber. This did not work and the chambers continued to collapse, so a directed pressure approach was developed. Instead of using two featureless layers of PDMS to sandwich the device, PDMS layers with the same features as the channels were used in order to minimise pressure over the channels of the device. While this was effective at reducing the collapsed chambers, all devices had to be visually inspected following bonding to ensure that they were not damaged.

The layers that made up the device were found to be bonded very weakly. Channels were found to be watertight, but the device layers were found to break apart very easily, especially when inserting and removing tubing. Increasing the bonding pressure by tightening the heat press plates led to deformed features and did not noticeably increase the bond strength. Ren *et al.* did not discuss the practicalities of connecting tubing, nor is there a discussion of bond strength in their devices [88]. It was decided that the device should be re-designed as pressure-driven rather than flow-driven to negate the need for tubing and syringe pumps. Since tubing did not need to be connected to the devices, they were far less likely to break in the middle of an experiment. This also made operation of the device much simpler, as cells and media could be easily pipetted into the inlet wells. The disadvantage of this approach is that a drug concentration gradient generator could not be utilised over the cell traps. Instead, the new device had five separate channels each with their own cell traps such that up to five concentrations of drug could be tested in parallel. This means that more solutions of drug are required to be prepared as there is no on-chip dilution. The loss of the gradient generator and therefore this change sacrificed a portion of the device's advantage over traditional platforms, however the structured cell traps remains as a large advantage for single-cell experiments. The new, larger devices also introduced a new problem for bonding, whereby some parts would not be fully bonded. This was overcome by re-bonding the devices with an additional thin layer of PDMS over the unbonded region, however every re-bond came with an additional risk of collapsing the device's channels.

Due to the poor gas permeability of FEP, the devices were prone to forming very large air bubbles, especially over the cell traps when first filled with liquid (section 3.11). This issue was not discussed by Ren *et al.* [88], however was overcome by degassing the devices in a vacuum and refrigerating to dissolve any residual air. This meant that devices needed to be pre-filled with liquid at least several hours prior to any experiments taking place.

It is also noted that there is a very poor contrast of microfluidic features under brightfield microscopy when the devices are filled with an aqueous solution such as PBS or cell culture media. This is believed to be due to the closeness of the refractive indices of FEP compared to water (1.34 and 1.33 respectively). This could potentially limit some applications of FEP-based microfluidics.

Overall, creating devices from FEP was found to be far more problematic than creating devices from PDMS. While Ren *et al.* provided basic instructions [88], a number of undiscussed issues were encountered and overcome, but not without compromise. Ultimately the suitability of FEP for creating microfluidic devices comes down to application. For this project it was necessary to avoid overlapping Raman peaks of the device and the cellular lipids and this is a unique application of this material. As previously discussed by Ren *et al.* [88] and tested by de Haas *et al.* [90], one of the main advantages of using Teflons is their chemical inertness, especially to strong solvents. Many of the other advantages of Teflons over PDMS are shared with other materials more commonly used such as polyurethanes [127] and polystyrene [128], and these materials are likely to be easier to work with than FEP. As a result, the findings of this project are not favourable for FEP as a material for creating microfluidic devices, unless the application demands it.

5.2 Raman Imaging of Lipids on the Microfluidic Device

It was aimed that the microfluidic device should build upon the work by Jamieson *et al.* [10], in which the lipid content of cancerous cells was measured using Raman spectroscopy after being treated with several drugs inhibiting various parts of the lipid synthesis pathway.

It was aimed that the device should be capable of simultaneously treating single cells with multiple concentrations of drugs in medium to high throughput manor and being able to measure the lipid content of the cells on-chip using Raman spectroscopy. Cells were also cultured in glass-bottomed dishes and glass coverslips as a comparison to the device.

While cells were successfully loaded into the device channels, the trap arrays did not work entirely as intended. After seeding, the majority of traps would remain empty (Approx 80%) while some would contain multiple cells (Approx 8%). Additionally, cells frequently became trapped in the device channels, outwith the traps. The expected behaviour of the device was that the majority of cell traps would contain a single cell, and that no cells would become stuck outwith the traps. A sufficient number of traps did contain single cells for analysis within this project, however this would need to be improved in order to fulfil the device's full potential. Reducing the trap size could prevent multiple cells from occupying the same trap, and increasing the cell seeding density, or seeding additional cells into the device could reduce the number of empty traps. It is also noted that cells would flow through different channels on the device at vastly different rates, despite being seeded at the same volumes. This suggests that some channels may have become deformed, most likely by partially collapsing during bonding. This would also explain why some cells were becoming stuck outwith the cell traps. If the channels were indeed partially collapsed, this would reduce the channel height and thus increase the hydraulic resistance as per equation1.5. An increase in hydraulic resistance would cause the initial flow rate within the channel to be lower as per equation1.4, as well as for the rate at which the dynamic flow rate decreases to be reduced as per equation1.12. A measurement of flow rates within the device was not performed during this project, however unpredictable channel deformation would suggest that theoretical calculations of channel resistance and flow rate are likely to be unreliable. This demonstrates that the fabrication methods were not optimal and need to be improved further.

A statistically significant ($p < 0.0001$) increase in the L/P ratio was detectable in cancerous PC3 cells within the device when treated with 100 µM Orlistat.

This is consistent with both findings from the glass-bottomed dishes/coverslips and with the literature [10]. A significant increase in L/P ratio for PNT2 cells was not detected however, despite this being the case for the fixed cells and as reported by Jamieson *et al.* [10]. Spectra from the devices tended to be weaker than spectra from the glass-bottomed dishes/coverslips, leading to generally fewer spectra per cell passing thresholding in the analysis script. Ratios from the devices had larger standard deviations than those from the glass-bottomed dishes/coverslips, making it harder to find statistically significant differences between conditions. This suggests that the devices may not be as effective for measuring Raman signals compared to traditional platforms. A potential improvement would be to use a thinner sheet of FEP for the lower trap-containing layer. The work presented here used a 0.5 mm thick sheet for this layer, however FEP sheets down to a thickness of 0.0125 mm are available from the same supplier. This would limit any potential attenuation of the signal between the cells and the objective lens of the microscope.

The fact that there is an increase in the lipid content of the cells when treated with orlistat, a FASN inhibitor, is perhaps counter-intuitive. It is nevertheless consistent with the findings of Jamieson *et al.*, who hypothesised that this may be due to a stress response from the cells, causing them to hold on to their lipids and to accumulate more lipids from the surrounding medium [10].

The SCD1 inhibitor CAY10566 was also tested on both PC3 and PNT2 cells trapped in the microfluidic device. Differences in the L/P ratio of these cells were not found to be statistically significant compared to controls. For the PC3 cells, this is consistent with the findings of Jamieson *et al.* [10], however in this paper, a significant ($p < 0.001$) difference was found for PNT2 cells.

The microfluidic platform was successfully used to treat PC3 cells with 5 different concentrations of Orlistat simultaneously. As expected, it was found that the cellular response to the drug tended to increase with applied concentration. As well as testing multiple concentrations of one drug, the device could potentially be used to simultaneously trial multiple drugs on a particular cell line, or to test the effectiveness of one drug on multiple cell lines.

In addition to Raman spectroscopy, fluorescence imaging of cells on the device was also demonstrated for viability staining. This revealed statistically significant drops in viability for both PC3 and PNT2 cell lines when treated with 100 µM orlistat. A surprising result here is that the viability of the non-cancerous PNT2 cells appears to have been more strongly affected than the cancerous PC3 cells, despite a change in L/P ratio being measured for PC3 cells and not for PNT2 cells. For cells fixed on glass bottomed dishes/coverslips, the viability of PC3 cells was more greatly affected by orlistat than PNT2 cells. It is however noted that in this environment, dead cells will dissociate from the glass surface and be washed off during the staining process, leading to an inaccurate live/dead count. As such, confluence must also be taken into account for an accurate measure of cell viability on such platforms. In the microfluidic device, the cells are trapped and therefore will not be washed out. This means that the live/dead count is a far more accurate measure of the viability of the treated cells. The downside of this is when experiments, such as Raman mapping, need to be performed on only viable cells. Without staining the cells it can be difficult to accurately assess viability, and fluorescence stains may alter the chemical composition of the cells. It can therefore be said that microfluidic platforms have an advantage over traditional methods when it comes to an accurate live/dead count, but are disadvantageous when analysis needs to be performed only on viable cells.

One of the intended advantages of the device is its throughput. Each channel contains three arrays of 132 single-cell traps, giving a possible total of 396 cells per condition. While investigating a large number of cells is possible using conventional platforms, the structured nature of the trap arrays makes it very easy to re-locate the same cells multiple times for a high throughput time study, something which is a future goal for this device. It was intended that the device should be capable of performing a time-study, investigating how the cellular lipid composition changed with time as the cells were exposed to various drugs. The confocal Raman mapping of cells can be a timely process, and is not suitable for this application; typically a single cell in the device would take 8-10 minutes to map under the settings used throughout this project.

While some initial attempts were made at gathering single spectra from individual cells at a low magnification, little to no spectral information could be obtained. With a higher magnification lens, cells needed to be mapped to produce averaged spectra to avoid localised variation skewing results. CARS is a very fast imaging methodology in comparison. For this reason, it was intended that CARS be used for time studies using the microfluidic device. When a device containing cells was imaged with CARS, a very high background was seen from the PBS within the device, obscuring signal from the cells. Additionally, the high powered lasers used on the CARS system caused large air bubbles to nucleate within the device channels. It is unclear why the PBS was giving such a high background at the imaged wavenumbers as this media was not an issue when analysing cells with Raman spectroscopy, it is possible that the cell culture media was not effectively washed out of the traps prior to analysis. The risk of nucleating air bubbles could possibly be mitigated by decreasing the power of the lasers.

With the loss of the drug concentration gradient generator from the original device design, one of the device's advantages over using traditional platforms was lost. As it stands, the device is capable of testing up to five concentrations of drug, each applied manually to each inlet well. While this could be replicated using fixed cells on a glass-bottomed multi-well plate, the device still has the advantage of being able to isolate single cells, and has the potential to be developed into a constant perfusion system rather than static culture one, which has been shown to be a more stable environment for culturing cells [109].

While Raman L/P results were replicated on the device for PC3 cells treated with 100 µM orlistat, a loss in sensitivity meant that a difference for PNT2 cells was not detected on the device. This could potentially be rectified by altering the imaging conditions, which were kept the same for all experiments so that they could be directly compared. The full throughput capabilities of the device could not be exploited due to the long Raman mapping time. Additionally, dead cells cannot be effectively washed out, leading to a potential mix of live and dead cells being mapped, where only live cells are desired.

Viability staining of cells within devices revealed that cells mostly remained viable within the device (79-88% under control conditions) which mitigates this risk somewhat, however PNT2 cells treated with orlistat were found to only be 57% viable. As such, the device is not without its limitations. the main advantage offered by the device in its current form is the miniaturisation compared to the traditional platforms used since it requires smaller volumes of cells, media and drugs.

In the literature, a microfluidic device reported by Cao *et al.* [68] was used to image cellular lipid droplets with stimulated Raman scattering (SRS), a technique similar to CARS. This device was constructed from PDMS, however the very low out-of-focus background associated with SRS meant that imaging the cells was not a problem. In initial imaging experiments within this project, CARS eliminated much of the out-of-focus background (section 3.2), however images were obscured by the in-focus cell traps in the devices used. Cao *et al.* did not use such cell traps, instead seeding cells into a network of miniature culture chambers and allowing the cells to adhere to the device surface. A network of microvalves was used to control flow in the device to add reagents to the culture chambers or to remove waste. A device similar in concept to this may have been a more appropriate choice for this project. There would still have been an issue with Raman spectroscopy due to the high background from out of plane PDMS, however such a device may have fared better with CARS imaging, and would not have had the issues discussed relating to FEP.

5.3 Future Developments

While the microfluidic device described in this thesis was successfully demonstrated to be capable of treating single cells with lipid synthesis targeting drugs and measuring metabolic changes with Raman spectroscopy, a number of improvements and developments could still be made.

Further optimisation of the manufacturing process is required, especially during bonding of the devices in order to prevent the malformation of channels which led to variation in flow rates and cells becoming stuck out with the cell traps. By having five parallel channels, the current device is limited to testing only five separate conditions. This has the potential to be scaled up with more channels per chip in a future revision.

By increasing the resistance of the channels and increasing the capacitance of the wells, the amount of time taken for the volume of the inlets to discharge through the channels could be increased, making the device more suited to constant perfusion. In order to improve the novelty of the device, one potential change would be to transform it from a single-cell platform to a multi-cellular one. By increasing the size of the cell traps, the device could be used to culture 3D spheroids in a similar manor to Mulholland *et al.* [71]. Spheroids are thought to offer a more accurate analogue to *in vivo* conditions compared to single cells [112], and so this would be a large advantage for the device when compared to fixed monolayer cultures.

An alternative single-layer PDMS-on-glass device could be designed with a similar concept to that used by Cao *et al.* [68]. Instead of trapping cells in PDMS traps, seeded cells could be allowed to adhere to the bottom layer glass of such a device and these cells could be treated with drugs supplied from a concentration gradient generator. CARS could then be used to analyse how the lipid composition of the cultured cells changes in real time as cells are treated with multiple concentrations of drug all in one miniaturised platform. This approach has the drawback that single cells would not be as well isolated from one another in comparison to a device in which single cells are trapped in either a U-shaped trap or microwell.

5.4 Conclusions

PDMS-based microfluidics was found to be unsuitable for Raman spectroscopy of cellular lipids due to the CH_3 groups within its chemical structure producing Raman peaks in the spectral ROI between 2800 cm^{-1} and 3000 cm^{-1}.

FEP was found to be a suitable substrate material for Raman spectroscopy of cellular lipids as, unlike many common materials for microfluidics, its Raman spectrum does not contain peaks between 2800 cm^{-1} and 3000 cm^{-1}. Raman spectroscopy of cellular lipids and proteins was successfully demonstrated on an FEP-based microfluidic device.

FEP was found to be a difficult material to work with when creating microfluidic devices as techniques are not as established compared with PDMS. Bond strength of the FEP layers were found to be particularly weak and devices could easily become damaged from gently inserting tubing in a flow-driven modality. While no analysis of the device cross section was performed, it is believed that channels could partially collapse during the bonding process leading to varying flow rates from channel to channel when used in a pressure-driven modality. Unless further improvements can be made to the manufacturing processes, FEP is concluded to be unsuitable for microfluidic devices requiring precise control of flow.

Raman spectroscopy of cells in the device generally produced weaker spectra than those measured on glass bottomed dishes or glass coverslips under the same imaging conditions. This led to some metabolic changes not being detected in the device. Imaging conditions were chosen to be the same for both devices and traditional platforms in order to directly compare the two methods. This could be further optimised for the microfluidic devices in order to produce a stronger signal (e.g. increasing the laser power).

Throughput of analysis was limited with Raman mapping as this takes a large amount of time per cell and CARS was found to nucleate air bubbles during imaging, however this could possibly be further optimised to avoid this issue.

Overall, the main advantages offered by the device in its current form over traditional platforms include miniaturisation, the isolation of single cells and its development potential for the constant perfusion of media and drugs.

Appendix A.

Acronyms and Abbreviations

CARS - Coherent Anti-Stokes Raman Scattering

DMEM - Dulbecco's Modified Eagle's Medium

DMSO - Dimethyl Sulfoxide

EthD - Ethidium Homodimer

FASN - Fatty Acid Synthase

FBS - Foetal Bovine Serum

FEP - Fluorinated Ethylene Propylene

HPMC - Hydroxypropyl Methylcellulose

L/P - Lipid/Protein

LPA - Lysophosphatidic Acid

NADP+/NADPH - Nicotinamide Adenine Dinucleotide Phosphate

PBS - Phosphate Buffered Saline

PDMS - Polydimethylsiloxane

PFA - Paraformaldehyde

PFLA - Perfluoroalkoxy Alkane

PFPE - Perfluoropolyethene

PGE2 - Prostaglandin E2

PMMA - Poly(methyl methacrylate)

PTFE - Polytetrafluoroethylene

ROI - Region of Interest

RPMI - Rosewell Park Memorial Institute Medium

S1P - Sphingosine-1-Phosphate

SCAP - SREBP Cleavage Activating Protein

SCD1 - Stearoyl-CoA desaturase 1

SRS - Stimulated Raman Scattering

SERS - Surface Enhanced Raman Spectroscopy

Appendix A. Acronyms and Abbreviations

SREBP - Sterol Regulatory Element Binding Protein

TOFA - 5-(Tetradecyloxy)-2-furoic acid

Appendix B.

MatLab Analysis Script

```
% Jacob Melnyk
% 18/04/2018
% Raman Lipid-Protein Peaks Analysis
%Generates Lipid/Protein ratios based on averaged spectra from a scan
%%%%%%%%%%%%%%%%%%%%%%%%%%%%%

%Clear variables from workspace
clear

%%%%%Parameters%%%%%
%Edit as needed

%Filename
fname = 'ENTER FILENAME';
%Set peak prominence threshold
threshold = 100;
%Set graphson to 1 to create graphs of data, 0 to bypass
graphson = 1;
%Set columns for heat map
col = 10;

%%%%%Get Data%%%%%
data = tgspcread(fname);
%Calculate number of spectra (n) and number of values per spectrum (m)
[m,n] = size(data.Y);
```

```
%%%%%Truncate Data%%%%%
%Set up empty vectors
x = [];
y = [];
%Truncate data between 2800 & 3050cm^-1
for i = 1:m
if data.X(i) > 2800 & data.X(i) < 3050
x = [x; data.X(i)];
y = [y; data.Y(i,:)];
end
end

%%%%%Threshold Spectra with prominent peaks%%%%%
%Flip matrices (Wire saves vector with decending wavenumber, Matlab requires ascending)
& ensure that y values are double.
xf = flipud(x);
yf = double(flipud(y));

%Setup vector to save spectra numbers with prominent protein peaks
s = [];

%Start loop to analyse each individual spectrum
for i = 1:n
%find peak values over threshold prominence, corresponding x values, widths and
prominences for spectrum j.
[pk, loc] = findpeaks(yf(:,i), xf, 'MinPeakProminence',threshold);

%Save significant protein peak spectra indices in vector
if loc > 2915 & loc < 2940
s = [s;i];
```

```
end
end

%Create matrix containing only interesting spectra
yt = yf(:,s);

%Average these spectra
yav = mean(yt,2);

%Print number of averaged spectra
averagedspectra = length(s)

%%%%%Find Protein/Lipid Ratio from averaged spectrum%%%%%
%Find lipid and protein peaks using findpeaks
[pks, locs] = findpeaks(yav);

%Find index of peak locations in lipid and protein ranges
lloc = find(xf(locs)>2844 & xf(locs)<2856);
ploc = find(xf(locs)>2915 & xf(locs)<2940);

%Find lipid & protein peak heights
yl = max(pks(lloc));
yp = max(pks(ploc));

%Find & display Lipid/Protein ratio
ratio = yl./yp

%Find and display peak positions
xl = xf(locs(lloc))
xp = xf(locs(ploc))
```

```
%%%%%Figures Control%%%%%
%If graphs are desired, create them, if not don't.
if graphson == 1
%%%%%Graph of Average Spectrum%%%%%
%Plot average spectrum
figure
plot(xf,yav)
title([fname, ' Average Spectrum'], 'Interpreter', 'none')
xlabel('Wavenumber (cm^-1)')
ylabel('Intensity (Counts)')

%%%%%Create Heatmap of Protein Peaks%%%%%
%Find closest x to 2930
xmap = find(xf > 2929 & xf < 2931);
%Create array of all intinsity values at given location
ivalues = [];

for i = 1:n
ivalues = [ivalues;yf(xmap,i)];
end

%Create vector of zeros
ivaluesmod = zeros(n,1);

%Insert intensity values of used spectra into zeros vector
ivaluesmod(s) = ivalues(s);

%Convert vector to matrix
map = vec2mat(ivaluesmod,col);
```

```
%Display Heatmap
figure
image(map,'CDataMapping','scaled')
colorbar
colormap(hot)
title([fname, ' Pixels used in ratio calculation - peak height at 2930cm^-1'], 'Interpreter',
'none')
else
end
```

Appendix C.

Hydraulic Capacitance Full Derivation

An inlet well driving flow in this way is analogous to a discharging capacitor in an electronic RC circuit. In electronics, the capacitance, C, is given by:

$$C = \frac{q}{U} \tag{C.1}$$

where q is the charge stored in the capacitor. The hydraulic equivalent is then:

$$C_{\mathrm{h}} = \frac{V}{\Delta P} \tag{C.2}$$

where C_h is the hydraulic capacitance, V is the volume of liquid that will be discharged during flow. If the outlet is infinitely large, then V and Δ P are simply the starting volume and pressure in the inlet well. The pressure, P, within the well is given by:

$$P = \rho g h \tag{C.3}$$

where ρ is the density of the liquid, g is acceleration due to gravity and h is the height of the liquid in the well. This can be related to the volume in the well using simple geometry. Assuming a cylindrical well, this becomes:

$$P = \rho g \frac{V}{\pi r^2} \tag{C.4}$$

where r is the well radius.

Current, I, and voltage in a simple RC circuit will both drop as the capacitor discharges. These can be calculated by the equations:

$$I(t) = I_0 e^{\frac{-t}{RC}} \tag{C.5}$$

$$U(t) = U_0 e^{\frac{-t}{RC}} \tag{C.6}$$

where I_0 and U_0 are the initial current and initial voltage respectively, and R is the electrical resistance of the circuit. Hydraulic equivalents are therefore:

$$Q(t) = Q_0 e^{\frac{-t}{R_\mathrm{h} C_\mathrm{h}}} \tag{C.7}$$

$$\Delta P(t) = \Delta P_0 e^{\frac{-t}{R_\mathrm{h} C_\mathrm{h}}} \tag{C.8}$$

For channels with outlet wells of a defined size, the filling of the outlet well as the inlet well discharges must be taken into account. The flow will stop when the well pressures are balanced, so it is necessary to calculate the volume that will have been discharged when the well pressures are balanced. Defining $V_i(t)$ and r_i as the inlet well volume and radius and $V_o(t)$ and r_o as the outlet well volume and radius gives:

$$\lim_{t\to\infty} \rho g \frac{V_\mathrm{i}(t)}{\pi {r_\mathrm{i}}^2} = \lim_{t\to\infty} \rho g \frac{V_\mathrm{o}(t)}{\pi {r_\mathrm{o}}^2} \tag{C.9}$$

which simplifies to:

$$\lim_{t\to\infty} \frac{V_\mathrm{i}(t)}{{r_\mathrm{i}}^2} = \lim_{t\to\infty} \frac{V_\mathrm{o}(t)}{{r_\mathrm{o}}^2} \tag{C.10}$$

rearranging gives:

$$\lim_{t\to\infty} \frac{V_\mathrm{i}(t)}{V_\mathrm{o}(t)} = \frac{{r_\mathrm{i}}^2}{{r_\mathrm{o}}^2} \tag{C.11}$$

$V_i(t)$ and $V_o(t)$ can be calculated by subtracting or adding the volume dispensed, V(t), respectively to their initial values:

$$V_\mathrm{i}(t) = V_\mathrm{i}(0) - V(t) \tag{C.12}$$

$$V_\mathrm{o}(t) = V_\mathrm{o}(0) + V(t) \tag{C.13}$$

When the well pressures are balanced:

$$\lim_{t\to\infty} \frac{V_{\mathrm{i}}(0) - V(t)}{V_{\mathrm{o}}(0) + V(t)} = \frac{{r_{\mathrm{i}}}^2}{{r_{\mathrm{o}}}^2} \tag{C.14}$$

Rearranging for the total volume discharged gives:

$$\lim_{t\to\infty} V(t) = \frac{V_{\mathrm{i}}(0) - \frac{{r_{\mathrm{i}}}^2}{{r_{\mathrm{o}}}^2} V_{\mathrm{o}}(0)}{1 + \frac{{r_{\mathrm{i}}}^2}{{r_{\mathrm{o}}}^2}} \tag{C.15}$$

Substituting this into equation C.2 gives the hydraulic capacitance in terms of easily calculable starting values:

$$C_{\mathrm{h}} = \frac{V_{\mathrm{i}}(0) - \frac{{r_{\mathrm{i}}}^2}{{r_{\mathrm{o}}}^2} V_{\mathrm{o}}(0)}{(1 + \frac{{r_{\mathrm{i}}}^2}{{r_{\mathrm{o}}}^2})\Delta P(0)} \tag{C.16}$$

The starting volumes of each well should be inconsequential to the hydraulic capacitance, which is entirely dependent on the geometry of the inlet and outlet wells. In order to calculate $\mathrm{C_h}$ in terms of geometry only, $\Delta\mathrm{P}(0)$ can be substituted in terms of starting volumes from equation C.4:

$$C_{\mathrm{h}} = \frac{V_{\mathrm{i}}(0) - \frac{{r_{\mathrm{i}}}^2}{{r_{\mathrm{o}}}^2} V_{\mathrm{o}}(0)}{(1 + \frac{{r_{\mathrm{i}}}^2}{{r_{\mathrm{o}}}^2})(\rho g \frac{V_{\mathrm{i}}(0)}{\pi {r_{\mathrm{i}}}^2} - \rho g \frac{V_{\mathrm{o}}(0)}{\pi {r_{\mathrm{o}}}^2})} \tag{C.17}$$

This equation simplifies such that all volume terms cancel out, leaving an equation in terms of well radii only:

$$C_{\mathrm{h}} = \frac{\pi {r_{\mathrm{i}}}^2 {r_{\mathrm{o}}}^2}{\rho g({r_{\mathrm{i}}}^2 + {r_{\mathrm{o}}}^2)} \tag{C.18}$$

To bring this derivation full circle, consider the special case in which the outlet well is infinitely large, such that the entire starting volume in the inlet well will be discharged:

$$\lim_{r_{\mathrm{o}}\to\infty} C_{\mathrm{h}} = \frac{\pi {r_{\mathrm{i}}}^2}{\rho g} \tag{C.19}$$

Substituting in equation C.4 gives:

$$\lim_{r_{\mathrm{o}} \to \infty} C_{\mathrm{h}} = \frac{V_{\mathrm{i}}}{P_{\mathrm{i}}} \tag{C.20}$$

which is the same as equation C.2.

Microfluidic devices such as these are commonly designed with equal sized inlets and outlets, i.e. $\mathrm{r_i} = \mathrm{r_o} = \mathrm{r}$. In this case:

$$C_{\mathrm{h}} = \frac{\pi r^2}{2\rho g} \tag{C.21}$$

Bibliography

[1] F. P. Kuhajda, K. Jenner, F. D. Wood, R. A. Hennigar, L. B. Jacobs, J. D. Dick, and G. R. Pasternack, "Fatty-acid synthesis - a potential selective target for antineoplastic therapy," *Proceedings of the National Academy of Sciences of the United States of America*, vol. 91, no. 14, pp. 6379–6383, 1994. [Online]. Available: <GotoISI>://WOS:A1994NV42000029

[2] G. B. Mills and W. H. Moolenaar, "The emerging role of lysophosphatidic acid in cancer," *Nature Reviews Cancer*, vol. 3, no. 8, pp. 582–591, 2003. [Online]. Available: <GotoISI>://WOS:000184554000014

[3] N. J. Pyne and S. Pyne, "Sphingosine 1-phosphate and cancer," *Nature Reviews Cancer*, vol. 10, no. 7, pp. 489–503, 2010. [Online]. Available: <GotoISI>://WOS:000279111900011

[4] K. Krysan, K. L. Reckamp, H. Dalwadi, S. Sharma, E. Rozengurt, M. Dohadwala, and S. M. Dubinett, "Prostaglandin e-2 activates mitogen-activated protein kinase/erk pathway signaling and cell proliferation in non-small cell lung cancer cells in an epidermal growth factor receptor-independent manner," *Cancer Research*, vol. 65, no. 14, pp. 6275–6281, 2005. [Online]. Available: <GotoISI>://WOS:000230633400037

[5] S. J. Kridel, F. Axelrod, N. Rozenkrantz, and J. W. Smith, "Orlistat is a novel inhibitor of fatty acid synthase with antitumor activity," *Cancer Research*, vol. 64, no. 6, pp. 2070–2075, 2004. [Online]. Available: <GotoISI>://WOS:000220249100027

[6] E. S. Pizer, F. D. Wood, H. S. Heine, F. E. Romantsev, G. R. Pasternack, and F. P. Kuhajda, "Inhibition of fatty acid synthesis delays disease progression in a xenograft model of ovarian cancer," *Cancer Research*, vol. 56, no. 6, pp. 1189–1193, 1996. [Online]. Available: <GotoISI>://WOS:A1996TZ52700004

[7] E. S. Pizer, J. Thupari, W. F. Han, M. L. Pinn, F. J. Chrest, G. L. Frehywot, C. A. Townsend, and F. P. Kuhajda, "Malonyl-coenzyme-a is a potential

mediator of cytotoxicity induced by fatty-acid synthase inhibition in human breast cancer cells and xenograft," *Cancer Research*, vol. 60, no. 2, pp. 213–218, 2000. [Online]. Available: <GotoISI>://WOS:000085041800003

[8] F. Mohammadzadeh, G. Mosayebi, V. Montazeri, M. Darabi, S. Fayezi, M. Shaaker, M. Rahmati, B. Baradaran, and A. Mehdizadeh, "Fatty acid composition of tissue cultured breast carcinoma and the effect of stearoyl-coa desaturase 1 inhibition," *Journal of Breast Cancer*, vol. 17, no. 2, pp. 136–142, 2014. [Online]. Available: <GotoISI>://WOS:000338395900006

[9] C. Wang, C. X. Xu, M. W. Sun, D. X. Luo, D. F. Liao, and D. L. Cao, "Acetyl-coa carboxylase-alpha inhibitor tofa induces human cancer cell apoptosis," *Biochemical and Biophysical Research Communications*, vol. 385, no. 3, pp. 302–306, 2009. [Online]. Available: <GotoISI>://WOS:000267149800003

[10] L. E. Jamieson, C. Wetherill, K. Faulds, and D. Graham, "Ratiometric raman imaging reveals the new anti-cancer potential of lipid targeting drugs," *Chemical Science*, vol. 9, no. 34, pp. 6935–6943, 2018. [Online]. Available: <GotoISI>://WOS:000444554100007

[11] L. Weiss, G. E. Hoffmann, R. Schreiber, H. Andres, E. Fuchs, E. Korber, and H. J. Kolb, "Fatty-acid biosynthesis in man, a pathway of minor importance - purification, optimal assay conditions, and organ distribution of fatty-acid synthase," *Biological Chemistry Hoppe-Seyler*, vol. 367, no. 9, pp. 905–912, 1986. [Online]. Available: <GotoISI>://WOS:A1986E361500022

[12] M. Omabe, M. Ezeani, and K. N. Omabe, "Lipid metabolism and cancer progression: The missing target in metastatic cancer treatment," *Journal of Applied Biomedicine*, vol. 13, no. 1, pp. 47–59, 2015. [Online]. Available: <GotoISI>://WOS:000350670600006

[13] D. E. Vance and J. E. Vance, *Biochemistry of Lipids, Lipoproteins and Membranes, 5th Edition*, 5th ed., ser. Biochemistry of Lipids, Lipoproteins and Membranes, 5th Edition, 2008.

[14] J. Reece, L. Urry, M. Cain, S. Wasserman, P. Minorsky, and R. Jackson, *Campbell Biology*, 9th ed. San Francisco: Pearson, 2011.

[15] A. H. Futerman and Y. A. Hannun, "The complex life of simple sphingolipids," *Embo Reports*, vol. 5, no. 8, pp. 777–782, 2004. [Online]. Available: <GotoISI>://WOS:000223005400010

[16] D. Z. Wang and R. N. Dubois, "Eicosanoids and cancer," *Nature Reviews Cancer*, vol. 10, no. 3, pp. 181–193, 2010. [Online]. Available: <GotoISI>://WOS:000274912000010

[17] O. Warburg, "Origin of cancer cells," *Science*, vol. 123, no. 3191, pp. 309–314, 1956. [Online]. Available: <GotoISI>://WOS:A1956ZQ16000002

[18] M. G. V. Heiden, L. C. Cantley, and C. B. Thompson, "Understanding the warburg effect: The metabolic requirements of cell proliferation," *Science*, vol. 324, no. 5930, pp. 1029–1033, 2009. [Online]. Available: <GotoISI>://WOS:000266246700031

[19] B. L. Horecker, "The pentose phosphate pathway," *Journal of Biological Chemistry*, vol. 277, no. 50, pp. 47 965–47 971, 2002. [Online]. Available: <GotoISI>://WOS:000179789600001

[20] K. C. Patra and N. Hay, "The pentose phosphate pathway and cancer," *Trends in Biochemical Sciences*, vol. 39, no. 8, pp. 347–354, 2014. [Online]. Available: <GotoISI>://WOS:000340075200003

[21] L. Weiss, G. E. Hoffmann, R. Schreiber, H. Andres, E. Fuchs, E. Korber, and H. J. Kolb, "Fatty-acid biosynthesis in man, a pathway of minor importance - purification, optimal assay conditions, and organ distribution of fatty-acid synthase," *Biological Chemistry Hoppe-Seyler*, vol. 367, no. 9, pp. 905–912, 1986. [Online]. Available: <GotoISI>://WOS:A1986E361500022

[22] F. Baenke, B. Peck, H. Miess, and A. Schulze, "Hooked on fat: the role of lipid synthesis in cancer metabolism and tumour development," *Disease*

Models & Mechanisms, vol. 6, no. 6, pp. 1353–1363, 2013. [Online]. Available: <GotoISI>://WOS:000329275000007

[23] E. J. Vancorven, A. Groenink, K. Jalink, T. Eichholtz, and W. H. Moolenaar, "Lysophosphatidate-induced cell-proliferation - identification and dissection of signaling pathways mediated by g-proteins," *Cell*, vol. 59, no. 1, pp. 45–54, 1989. [Online]. Available: <GotoISI>://WOS:A1989AU52300007

[24] X. J. Fang, S. X. Yu, R. LaPushin, Y. L. Lu, T. Furui, L. Z. Penn, D. Stokoe, J. R. Erickson, R. C. Bast, and G. B. Mills, "Lysophosphatidic acid prevents apoptosis in fibroblasts via g(i)-protein-mediated activation of mitogen-activated protein kinase," *Biochemical Journal*, vol. 352, pp. 135–143, 2000. [Online]. Available: <GotoISI>://WOS:000165643200014

[25] F. N. van Leeuwen, C. Olivo, S. Grivell, B. N. G. Giepmans, J. G. Collard, and W. H. Moolenaar, "Rac activation by lysophosphatidic acid lpa(1) receptors through the guanine nucleotide exchange factor tiam1," *Journal of Biological Chemistry*, vol. 278, no. 1, pp. 400–406, 2003. [Online]. Available: <GotoISI>://WOS:000180255700053

[26] M. H. Graler, R. Grosse, A. Kusch, E. Kremmer, T. Gudermann, and M. Lipp, "The sphingosine 1-phosphate receptor s1p(4) regulates cell shape and motility via coupling to gi and g(12/13)," *Journal of Cellular Biochemistry*, vol. 89, no. 3, pp. 507–519, 2003. [Online]. Available: <GotoISI>://WOS:000183135500008

[27] O. Cuvillier, G. Pirianov, B. Kleuser, P. G. Vanek, O. A. Coso, J. S. Gutkind, and S. Spiegel, "Suppression of ceramide-mediated programmed cell death by sphingosine-1-phosphate," *Nature*, vol. 381, no. 6585, pp. 800–803, 1996. [Online]. Available: <GotoISI>://WOS:A1996UU35600064

[28] T. Licht, L. Tsirulnikov, H. Reuveni, T. Yarnitzky, and S. A. Ben-Sasson, "Induction of pro-angiogenic signaling by a synthetic peptide derived from the second intracellular loop of s1p(3) (edg3)," *Blood*, vol. 102, no. 6, pp. 2099–2107, 2003. [Online]. Available: <GotoISI>://WOS:000185322800033

[29] S. H. Chang, C. H. Liu, R. Conway, D. K. Han, K. Nithipatikom, O. C. Trifan, T. F. Lane, and T. Hla, "Role of prostaglandin e-2-dependent angiogenic switch in cyclooxygenase 2-induced breast cancer progression," *Proceedings of the National Academy of Sciences of the United States of America*, vol. 101, no. 2, pp. 591–596, 2004. [Online]. Available: <GotoISI>://WOS:000188210400033

[30] M. Zeddou, R. Greimers, N. de Valensart, B. Nayjib, K. Tasken, J. Boniver, M. Moutschen, and S. Rahmouni, "Prostaglandin e-2 induces the expression of functional inhibitory cd94/nkg2a receptors in human cd8(+) t lymphocytes by a camp-dependent protein kinase a type i pathway," *Biochemical Pharmacology*, vol. 70, no. 5, pp. 714–724, 2005. [Online]. Available: <GotoISI>://WOS:000231338900008

[31] M. Ahmadi, D. C. Emery, and D. J. Morgan, "Prevention of both direct and cross-priming of antitumor cd8(+) t-cell responses following overproduction of prostaglandin e-2 by tumor cells in vivo," *Cancer Research*, vol. 68, no. 18, pp. 7520–7529, 2008. [Online]. Available: <GotoISI>://WOS:000259422400034

[32] T. Chung, A. R. Phillips, and R. D. Vierstra, "Atg8 lipidation and atg8-mediated autophagy in arabidopsis require atg12 expressed from the differentially controlled atg12a and atg12b loci," *Plant Journal*, vol. 62, no. 3, pp. 483–493, 2010. [Online]. Available: <GotoISI>://WOS:000276659400012

[33] E. White, "The role for autophagy in cancer," *Journal of Clinical Investigation*, vol. 125, no. 1, pp. 42–46, 2015. [Online]. Available: <GotoISI>://WOS:000347747300006

[34] T. Mashima, H. Seimiya, and T. Tsuruo, "De novo fatty-acid synthesis and related pathways as molecular targets for cancer therapy," *British Journal of Cancer*, vol. 100, no. 9, pp. 1369–1372, 2009. [Online]. Available: <GotoISI>://WOS:000265575200001

[35] L. Sjostrom, A. Rissanen, T. Andersen, M. Boldrin, A. Golay, H. P. F. Koppeschaar, M. Krempf, and G. European Multicentre Orlistat Study,

"Randomised placebo-controlled trial of orlistat for weight loss and prevention of weight regain in obese patients," *Lancet*, vol. 352, no. 9123, pp. 167–172, 1998. [Online]. Available: <GotoISI>://WOS:000074859800008

[36] C. D. Browne, E. J. Hindmarsh, and J. W. Smith, "Inhibition of endothelial cell proliferation and angiogenesis by orlistat, a fatty acid synthase inhibitor," *Faseb Journal*, vol. 20, no. 12, pp. 2027–2035, 2006. [Online]. Available: <GotoISI>://WOS:000241156900011

[37] P. Y. Yang, K. Liu, M. H. Ngai, M. J. Lear, M. R. Wenk, and S. Q. Yao, "Activity-based proteome profiling of potential cellular targets of orlistat - an fda-approved drug with anti-tumor activities," *Journal of the American Chemical Society*, vol. 132, no. 2, pp. 656–666, 2010. [Online]. Available: <GotoISI>://WOS:000275084600044

[38] F. Fang and J. Q. Shen, "Cerulenin induces apoptosis in hepatic cancer hepg2 cells in vitro and in vivo," *International Journal of Clinical and Experimental Medicine*, vol. 12, no. 7, pp. 8334–8341, 2019. [Online]. Available: <GotoISI>://WOS:000477991300042

[39] S. Murata, K. Yanagisawa, K. Fukunaga, T. Oda, A. Kobayashi, R. Sasaki, and N. Ohkohchi, "Fatty acid synthase inhibitor cerulenin suppresses liver metastasis of colon cancer in mice," *Cancer Science*, vol. 101, no. 8, pp. 1861–1865, 2010. [Online]. Available: <GotoISI>://WOS:000280148900014

[40] C. Rae, U. Haberkorn, J. W. Babich, and R. J. Mairs, "Inhibition of fatty acid synthase sensitizes prostate cancer cells to radiotherapy," *Radiation Research*, vol. 184, no. 5, pp. 482–493, 2015. [Online]. Available: <GotoISI>://WOS:000365800700004

[41] E. Currie, A. Schulze, R. Zechner, T. C. Walther, and R. V. Farese, "Cellular fatty acid metabolism and cancer," *Cell Metabolism*, vol. 18, no. 2, pp. 153–161, 2013. [Online]. Available: <GotoISI>://WOS:000326267200005

[42] C. V. Raman and K. S. Krishnan, "A new type of secondary radiation," *Nature*, vol. 121, pp. 501–502, 1928. [Online]. Available: <GotoISI>://WOS:000189300700216

[43] E. Smith and G. Dent, "Modern raman spectroscopy: A practical approach," *Modern Raman Spectroscopy: a Practical Approach*, pp. 1–210, 2005. [Online]. Available: <GotoISI>://WOS:000298167600009

[44] C. V. Raman, "The raman effect. investigation of molecular structure by light scattering," *Transactions of the Faraday Society*, vol. 25, pp. 0781–0791, 1929. [Online]. Available: <GotoISI>://WOS:000202768000078

[45] J. W. Williams and A. Hollaender, "The molecular scattering of light from ammonia solutions the fine structure of a vibrational raman band," *Physical Review*, vol. 42, no. 3, pp. 0379–0385, 1932. [Online]. Available: <GotoISI>://WOS:000201591700008

[46] R. L. Farrow, R. K. Chang, S. Mroczkowski, and F. H. Pollak, "Detection of excess crystalline as and sb in iii-v oxide interfaces by raman-scattering," *Applied Physics Letters*, vol. 31, no. 11, pp. 768–770, 1977. [Online]. Available: <GotoISI>://WOS:A1977EB38000022

[47] S. Krimm and J. Bandekar, "Vibrational spectroscopy and conformation of peptides, polypeptides, and proteins," *Advances in Protein Chemistry*, vol. 38, pp. 181–364, 1986. [Online]. Available: <GotoISI>://WOS:A1986E613400004

[48] M. A. Pimenta, G. Dresselhaus, M. S. Dresselhaus, L. G. Cancado, A. Jorio, and R. Saito, "Studying disorder in graphite-based systems by raman spectroscopy," *Physical Chemistry Chemical Physics*, vol. 9, no. 11, pp. 1276–1291, 2007. [Online]. Available: <GotoISI>://WOS:000244776800001

[49] J. R. Lakowicz, *Principles of Fluorescence Spectroscopy*, 3rd ed. Springer, 2006.

[50] N. Uzunbajakava, A. Lenferink, Y. Kraan, E. Volokhina, G. Vrensen, J. Greve, and C. Otto, "Nonresonant confocal raman imaging of dna and protein

distribution in apoptotic cells," *Biophysical Journal*, vol. 84, no. 6, pp. 3968–3981, 2003. [Online]. Available: <GotoISI>://WOS:000183129800042

[51] S. M. Nie and S. R. Emery, "Probing single molecules and single nanoparticles by surface-enhanced raman scattering," *Science*, vol. 275, no. 5303, pp. 1102–1106, 1997. [Online]. Available: <GotoISI>://WOS:A1997WJ50300037

[52] K. Kneipp, A. S. Haka, H. Kneipp, K. Badizadegan, N. Yoshizawa, C. Boone, K. E. Shafer-Peltier, J. T. Motz, R. R. Dasari, and M. S. Feld, "Surface-enhanced raman spectroscopy in single living cells using gold nanoparticles," *Applied Spectroscopy*, vol. 56, no. 2, pp. 150–154, 2002. [Online]. Available: <GotoISI>://WOS:000174269500002

[53] Y. W. C. Cao, R. C. Jin, and C. A. Mirkin, "Nanoparticles with raman spectroscopic fingerprints for dna and rna detection," *Science*, vol. 297, no. 5586, pp. 1536–1540, 2002. [Online]. Available: <GotoISI>://WOS:000177697300052

[54] I. Chen and A. Y. Ting, "Site-specific labeling of proteins with small molecules in live cells," *Current Opinion in Biotechnology*, vol. 16, no. 1, pp. 35–40, 2005. [Online]. Available: <GotoISI>://WOS:000227383000006

[55] M. Vendrell, K. K. Maiti, K. Dhaliwal, and Y. T. Chang, "Surface-enhanced raman scattering in cancer detection and imaging," *Trends in Biotechnology*, vol. 31, no. 4, pp. 249–257, 2013. [Online]. Available: <GotoISI>://WOS:000317457900008

[56] S. Schlucker, "Sers microscopy: Nanoparticle probes and biomedical applications," *Chemphyschem*, vol. 10, no. 9-10, pp. 1344–1354, 2009. [Online]. Available: <GotoISI>://WOS:000267928100001

[57] C. L. Evans, E. O. Potma, M. Puoris'haag, D. Cote, C. P. Lin, and X. S. Xie, "Chemical imaging of tissue in vivo with video-rate coherent anti-stokes raman scattering microscopy," *Proceedings of the National Academy of Sciences of the United States of America*, vol. 102, no. 46, pp. 16 807–16 812, 2005. [Online]. Available: <GotoISI>://WOS:000233462900051

[58] J. X. Cheng, A. Volkmer, L. D. Book, and X. S. Xie, "Multiplex coherent anti-stokes raman scattering microspectroscopy and study of lipid vesicles," *Journal of Physical Chemistry B*, vol. 106, no. 34, pp. 8493–8498, 2002. [Online]. Available: <GotoISI>://WOS:000177705200003

[59] M. Okuno, H. Kano, P. Leproux, V. Couderc, J. P. R. Day, M. Bonn, and H. Hamaguchi, "Quantitative cars molecular fingerprinting of single living cells with the use of the maximum entropy method," *Angewandte Chemie-International Edition*, vol. 49, no. 38, pp. 6773–6777, 2010. [Online]. Available: <GotoISI>://WOS:000282541300011

[60] C. J. Frank, R. L. McCreery, and D. C. B. Redd, "Raman-spectroscopy of normal and diseased human breast tissues," *Analytical Chemistry*, vol. 67, no. 5, pp. 777–783, 1995. [Online]. Available: <GotoISI>://WOS:A1995QK14400009

[61] H. Abramczyk and B. Brozek-Pluska, "New look inside human breast ducts with raman imaging. raman candidates as diagnostic markers for breast cancer prognosis: Mammaglobin, palmitic acid and sphingomyelin," *Analytica Chimica Acta*, vol. 909, pp. 91–100, 2016. [Online]. Available: <GotoISI>://WOS:000369093600011

[62] C. S. Sweetenham and I. Notingher, "Raman spectroscopy methods for detecting and imaging supported lipid bilayers," *Spectroscopy-an International Journal*, vol. 24, no. 1-2, pp. 113–117, 2010. [Online]. Available: <GotoISI>://WOS:000278029800014

[63] C. Krafft, L. Neudert, T. Simat, and R. Salzer, "Near infrared raman spectra of human brain lipids," *Spectrochimica Acta Part a-Molecular and Biomolecular Spectroscopy*, vol. 61, no. 7, pp. 1529–1535, 2005. [Online]. Available: <GotoISI>://WOS:000228736000027

[64] X. L. Li, J. J. Sha, B. Q. Chu, Y. Z. Wei, W. H. Huang, H. Zhou, N. Xu, and Y. He, "Quantitative visualization of intracellular lipids concentration in a microalgae cell based on raman micro-spectroscopy coupled with chemometrics,"

Sensors and Actuators B-Chemical, vol. 292, pp. 7–15, 2019. [Online]. Available: <GotoISI>://WOS:000467537100002

[65] A. M. Ranieri, C. Caporale, V. Fiorini, A. Hubbard, P. Rigby, S. Stagni, E. Watkin, M. I. Ogden, M. J. Hackett, and M. Massi, "Complementary approaches to imaging subcellular lipid architectures in live bacteria using phosphorescent iridium complexes and raman spectroscopy," *Chemistry-a European Journal*, p. 6. [Online]. Available: <GotoISI>://WOS:000477138800001

[66] D. B. Weibel and G. M. Whitesides, "Applications of microfluidics in chemical biology," *Current Opinion in Chemical Biology*, vol. 10, no. 6, pp. 584–591, 2006. [Online]. Available: <GotoISI>://WOS:000242919700009

[67] S. Y. Wang, F. Yue, L. C. Zhang, J. R. Wang, Y. Y. Wang, L. Jiang, B. C. Lin, and Q. Wang, "Application of microfluidic gradient chip in the analysis of lung cancer chemotherapy resistance," *Journal of Pharmaceutical and Biomedical Analysis*, vol. 49, no. 3, pp. 806–810, 2009. [Online]. Available: <GotoISI>://WOS:000264409800033

[68] C. Cao, D. Zhou, T. Chen, A. M. Streets, and Y. Y. Huang, "Label-free digital quantification of lipid droplets in single cells by stimulated raman microscopy on a microfluidic platform," *Analytical Chemistry*, vol. 88, no. 9, pp. 4931–4939, 2016. [Online]. Available: <GotoISI>://WOS:000379636600048

[69] Q. S. Chen, J. Wu, Y. D. Zhang, Z. Lin, and J. M. Lin, "Targeted isolation and analysis of single tumor cells with aptamer-encoded microwell array on microfluidic device," *Lab on a Chip*, vol. 12, no. 24, pp. 5180–5185, 2012. [Online]. Available: <GotoISI>://WOS:000311964700009

[70] N. Wen, Z. Zhao, B. Y. Fan, D. Y. Chen, D. Men, J. B. Wang, and J. Chen, "Development of droplet microfluidics enabling high-throughput single-cell analysis," *Molecules*, vol. 21, no. 7, p. 13, 2016. [Online]. Available: <GotoISI>://WOS:000381509700066

[71] T. Mulholland, M. McAllister, S. Patek, D. Flint, M. Underwood, A. Sim, J. Edwards, and M. Zagnoni, "Drug screening of biopsy-derived spheroids using a self-generated microfluidic concentration gradient," *Scientific Reports*, vol. 8, p. 12, 2018. [Online]. Available: <GotoISI>://WOS:000446035900002

[72] C. MacKerron, G. Robertson, M. Zagnoni, and T. J. Bushell, "A microfluidic platform for the characterisation of cns active compounds," *Scientific Reports*, vol. 7, p. 11, 2017. [Online]. Available: <GotoISI>://WOS:000415282900007

[73] B. Ma, G. H. Zhang, J. H. Qin, and B. C. Lin, "Characterization of drug metabolites and cytotoxicity assay simultaneously using an integrated microfluidic device," *Lab on a Chip*, vol. 9, no. 2, pp. 232–238, 2009. [Online]. Available: <GotoISI>://WOS:000262649500007

[74] B. V. Chikkaveeraiah, V. Mani, V. Patel, J. S. Gutkind, and J. F. Rusling, "Microfluidic electrochemical immunoarray for ultrasensitive detection of two cancer biomarker proteins in serum," *Biosensors & Bioelectronics*, vol. 26, no. 11, pp. 4477–4483, 2011. [Online]. Available: <GotoISI>://WOS:000293104100035

[75] S. Lee, J. Choi, L. Chen, B. Park, J. B. Kyong, G. H. Seong, J. Choo, Y. Lee, K. H. Shin, E. K. Lee, S. W. Joo, and K. H. Lee, "Fast and sensitive trace analysis of malachite green using a surface-enhanced raman microfluidic sensor," *Analytica Chimica Acta*, vol. 590, no. 2, pp. 139–144, 2007. [Online]. Available: <GotoISI>://WOS:000246321300001

[76] K. Yea, S. Lee, J. B. Kyong, J. Choo, E. K. Lee, and S. W. Joo, "Ultra-sensitive trace analysis of cyanide water pollutant in a pdms microfluidic channel using surface-enhanced raman spectroscopy," *Analyst*, vol. 130, no. 7, pp. 1009–1011, 2005. [Online]. Available: <GotoISI>://WOS:000229861800006

[77] H. Zhang, W. Zhang, L. F. Xiao, Y. Liu, T. A. Gilbertson, and A. H. Zhou, "Use of surface-enhanced raman scattering (sers) probes to detect fatty acid receptor activity in a microfluidic device," *Sensors*, vol. 19, no. 7, p. 15, 2019. [Online]. Available: <GotoISI>://WOS:000465570700182

[78] M. R. Hoonejani, A. Pallaoro, G. B. Braun, M. Moskovits, and C. D. Meinhart, "Quantitative multiplexed simulated-cell identification by sers in microfluidic devices," *Nanoscale*, vol. 7, no. 40, pp. 16 834–16 840, 2015. [Online]. Available: <GotoISI>://WOS:000362662100036

[79] M. R. Willner, K. S. McMillan, D. Graham, P. J. Vikesland, and M. Zagnoni, "Surface-enhanced raman scattering based microfluidics for single-cell analysis," *Analytical Chemistry*, vol. 90, no. 20, pp. 12 004–12 010, 2018. [Online]. Available: <GotoISI>://WOS:000447816400037

[80] H. S. Kim, S. C. Waqued, D. T. Nodurft, T. P. Devarenne, V. V. Yakovlev, and A. Han, "Raman spectroscopy compatible pdms droplet microfluidic culture and analysis platform towards on-chip lipidomics," *Analyst*, vol. 142, no. 7, pp. 1054–1060, 2017. [Online]. Available: <GotoISI>://WOS:000400689100005

[81] J. C. McDonald, D. C. Duffy, J. R. Anderson, D. T. Chiu, H. K. Wu, O. J. A. Schueller, and G. M. Whitesides, "Fabrication of microfluidic systems in poly(dimethylsiloxane)," *Electrophoresis*, vol. 21, no. 1, pp. 27–40, 2000. [Online]. Available: <GotoISI>://WOS:000085065800004

[82] H. Lorenz, M. Despont, N. Fahrni, J. Brugger, P. Vettiger, and P. Renaud, "High-aspect-ratio, ultrathick, negative-tone near-uv photoresist and its applications for mems," *Sensors and Actuators a-Physical*, vol. 64, no. 1, pp. 33–39, 1998. [Online]. Available: <GotoISI>://WOS:000071029100005

[83] W.-I. Wu, K. N. Sask, J. L. Brash, and P. R. Selvaganapathy, "Polyurethane-based microfluidic devices for blood contacting applications," *Lab on a Chip*, vol. 12, no. 5, pp. 960–970, 2012. [Online]. Available: <GotoISI>://WOS:000300047800016

[84] K. Domansky, D. C. Leslie, J. McKinney, J. P. Fraser, J. D. Sliz, T. Hamkins-Indik, G. A. Hamilton, A. Bahinski, and D. E. Ingber, "Clear castable polyurethane elastomer for fabrication of microfluidic devices," *Lab*

on a Chip, vol. 13, no. 19, pp. 3956–3964, 2013. [Online]. Available: <GotoISI>://WOS:000323835700021

[85] E. Sollier, C. Murray, P. Maoddi, and D. Di Carlo, "Rapid prototyping polymers for microfluidic devices and high pressure injections," *Lab on a Chip*, vol. 11, no. 22, pp. 3752–3765, 2011. [Online]. Available: <GotoISI>://WOS:000296099900002

[86] M. Haiducu, M. Rahbar, I. G. Foulds, R. W. Johnstone, D. Sameoto, and M. Parameswaran, "Deep-uv patterning of commercial grade pmma for low-cost, large-scale microfluidics," *Journal of Micromechanics and Microengineering*, vol. 18, no. 11, p. 7, 2008. [Online]. Available: <GotoISI>://WOS:000260263900029

[87] I. Rodriguez, P. Spicar-Mihalic, C. L. Kuyper, G. S. Fiorini, and D. T. Chiu, "Rapid prototyping of glass microchannels," *Analytica Chimica Acta*, vol. 496, no. 1-2, pp. 205–215, 2003. [Online]. Available: <GotoISI>://WOS:000186499000020

[88] K. N. Ren, W. Dai, J. H. Zhou, J. Su, and H. K. Wu, "Whole-teflon microfluidic chips," *Proceedings of the National Academy of Sciences of the United States of America*, vol. 108, no. 20, pp. 8162–8166, 2011. [Online]. Available: <GotoISI>://WOS:000290719600023

[89] H. Zheng, W. Z. Wang, X. J. Li, Z. H. Wang, L. Hood, C. Lausted, and Z. Y. Hu, "An automated teflon microfluidic peptide synthesizer," *Lab on a Chip*, vol. 13, no. 17, pp. 3347–3350, 2013. [Online]. Available: <GotoISI>://WOS:000322515200004

[90] T. W. de Haas, H. Fadaei, and D. Sinton, "Laminated thin-film teflon chips for petrochemical applications," *Lab on a Chip*, vol. 12, no. 21, pp. 4236–4239, 2012. [Online]. Available: <GotoISI>://WOS:000310916100004

[91] B. Shen and H. K. Wu, "Aqueous and nonaqueous electrochemical sensing on whole-teflon chip," *Acs Sensors*, vol. 1, no. 3, pp. 251–257, 2016. [Online]. Available: <GotoISI>://WOS:000385464400008

[92] X. L. Zhu and T. H. Cui, "Polymer shrinkage of hot embossed microstructures for higher aspect ratio and smaller size," *Sensors and Actuators a-Physical*, vol. 195, pp. 21–26, 2013. [Online]. Available: <GotoISI>://WOS:000320145000003

[93] J. Narasimhan and I. Papautsky, "Rapid fabrication of hot embossing tools using pdms," in *Conference on Microfluidics, BioMEMS, and Medical Microsystems*, ser. Proceedings of SPIE, vol. 4982. BELLINGHAM: Spie-Int Soc Optical Engineering, 2003, Conference Proceedings, pp. 110–119. [Online]. Available: <GotoISI>://WOS:000181864600016

[94] B. Shen, B. Xiong, and H. K. Wu, "Convenient surface functionalization of whole-teflon chips with polydopamine coating," *Biomicrofluidics*, vol. 9, no. 4, p. 11, 2015. [Online]. Available: <GotoISI>://WOS:000360311900013

[95] J. R. Lake, K. C. Heyde, and W. C. Ruder, "Low-cost feedback-controlled syringe pressure pumps for microfluidics applications," *Plos One*, vol. 12, no. 4, p. 12, 2017. [Online]. Available: <GotoISI>://WOS:000399351000075

[96] K. W. Oh, K. Lee, B. Ahn, and E. P. Furlani, "Design of pressure-driven microfluidic networks using electric circuit analogy," *Lab on a Chip*, vol. 12, no. 3, pp. 515–545, 2012. [Online]. Available: <GotoISI>://WOS:000298964300013

[97] W. Choi, M. Hashimoto, A. K. Ellerbee, X. Chen, K. J. M. Bishop, P. Garstecki, H. A. Stone, and G. M. Whitesides, "Bubbles navigating through networks of microchannels," *Lab on a Chip*, vol. 11, no. 23, pp. 3970–3978, 2011. [Online]. Available: <GotoISI>://WOS:000296737100006

[98] T. Pravinraj and R. Patrikar, "Modeling and characterization of surface roughness effect on fluid flow in a polydimethylsiloxane microchannel using a fractal based lattice boltzmann method," *Aip Advances*, vol. 8, no. 6, p. 6, 2018. [Online]. Available: <GotoISI>://WOS:000436855300038

[99] G. M. Walker and D. J. Beebe, "A passive pumping method for microfluidic devices," *Lab on a Chip*, vol. 2, no. 3, pp. 131–134, 2002. [Online]. Available: <GotoISI>://WOS:000178030900003

[100] M. H. Wu, S. B. Huang, and G. B. Lee, "Microfluidic cell culture systems for drug research," *Lab on a Chip*, vol. 10, no. 8, pp. 939–956, 2010. [Online]. Available: <GotoISI>://WOS:000276218900001

[101] J. Nilsson, M. Evander, B. Hammarstrom, and T. Laurell, "Review of cell and particle trapping in microfluidic systems," *Analytica Chimica Acta*, vol. 649, no. 2, pp. 141–157, 2009. [Online]. Available: <GotoISI>://WOS:000269652800002

[102] D. J. Wang and S. Bodovitz, "Single cell analysis: the new frontier in 'omics'," *Trends in Biotechnology*, vol. 28, no. 6, pp. 281–290, 2010. [Online]. Available: <GotoISI>://WOS:000278946500001

[103] D. Di Carlo, N. Aghdam, and L. P. Lee, "Single-cell enzyme concentrations, kinetics, and inhibition analysis using high-density hydrodynamic cell isolation arrays," *Analytical Chemistry*, vol. 78, no. 14, pp. 4925–4930, 2006. [Online]. Available: <GotoISI>://WOS:000239017700022

[104] C. A. Cunha-Matos, O. R. Millington, A. W. Wark, and M. Zagnoni, "Real-time assessment of nanoparticle-mediated antigen delivery and cell response," *Lab on a Chip*, vol. 16, no. 17, pp. 3374–3381, 2016. [Online]. Available: <GotoISI>://WOS:000382684100022

[105] C. Probst, A. Grunberger, W. Wiechert, and D. Kohlheyer, "Polydimethylsiloxane (pdms) sub-micron traps for single-cell analysis of bacteria," *Micromachines*, vol. 4, no. 4, pp. 357–369, 2013. [Online]. Available: <GotoISI>://WOS:000329707400001

[106] J. R. Rettig and A. Folch, "Large-scale single-cell trapping and imaging using microwell arrays," *Analytical Chemistry*, vol. 77, no. 17, pp. 5628–5634, 2005. [Online]. Available: <GotoISI>://WOS:000231652300039

[107] M. H. Wu, J. P. G. Urban, Z. Cui, and Z. F. Cui, "Development of pdms microbioreactor with well-defined and homogenous culture environment for chondrocyte 3-d culture," *Biomedical Microdevices*, vol. 8, no. 4, pp. 331–340, 2006. [Online]. Available: <GotoISI>://WOS:000241747900007

[108] S. Razaq, R. J. Wilkins, and J. P. G. Urban, "The effect of extracellular ph on matrix turnover by cells of the bovine nucleus pulposus," *European Spine Journal*, vol. 12, no. 4, pp. 341–349, 2003. [Online]. Available: <GotoISI>://WOS:000185092900001

[109] M. Sittinger, O. Schultz, G. Keyszer, W. W. Minuth, and G. R. Burmester, "Artificial tissues in perfusion culture," *International Journal of Artificial Organs*, vol. 20, no. 1, pp. 57–62, 1997. [Online]. Available: <GotoISI>://WOS:A1997WJ87700011

[110] T. Kim, M. Pinelis, and M. M. Maharbiz, "Generating steep, shear-free gradients of small molecules for cell culture," *Biomedical Microdevices*, vol. 11, no. 1, pp. 65–73, 2009. [Online]. Available: <GotoISI>://WOS:000263114000007

[111] S. K. W. Dertinger, D. T. Chiu, N. L. Jeon, and G. M. Whitesides, "Generation of gradients having complex shapes using microfluidic networks," *Analytical Chemistry*, vol. 73, no. 6, pp. 1240–1246, 2001. [Online]. Available: <GotoISI>://WOS:000167546400026

[112] E. Fennema, N. Rivron, J. Rouwkema, C. van Blitterswijk, and J. de Boer, "Spheroid culture as a tool for creating 3d complex tissues," *Trends in Biotechnology*, vol. 31, no. 2, pp. 108–115, 2013. [Online]. Available: <GotoISI>://WOS:000315179800009

[113] A. Sin, K. C. Chin, M. F. Jamil, Y. Kostov, G. Rao, and M. L. Shuler, "The design and fabrication of three-chamber microscale cell culture analog devices with integrated dissolved oxygen sensors," *Biotechnology Progress*, vol. 20, no. 1, pp. 338–345, 2004. [Online]. Available: <GotoISI>://WOS:000188861300045

[114] K. Viravaidya, A. Sin, and M. L. Shuler, "Development of a microscale cell culture analog to probe naphthalene toxicity," *Biotechnology Progress*, vol. 20, no. 1, pp. 316–323, 2004. [Online]. Available: <GotoISI>://WOS:000188861300042

[115] J. D. Wu, X. Wu, and F. Lin, "Recent developments in microfluidics-based chemotaxis studies," *Lab on a Chip*, vol. 13, no. 13, pp. 2484–2499, 2013. [Online]. Available: <GotoISI>://WOS:000319876500004

[116] B. G. Ricart, B. John, D. Lee, C. A. Hunter, and D. A. Hammer, "Dendritic cells distinguish individual chemokine signals through ccr7 and cxcr4," *Journal of Immunology*, vol. 186, no. 1, pp. 53–61, 2011. [Online]. Available: <GotoISI>://WOS:000285688700012

[117] C. Scherber, A. J. Aranyosi, B. Kulemann, S. P. Thayer, M. Toner, O. Iliopoulos, and D. Irimia, "Epithelial cell guidance by self-generated egf gradients," *Integrative Biology*, vol. 4, no. 3, pp. 259–269, 2012. [Online]. Available: <GotoISI>://WOS:000300827100002

[118] A. I. Skilitsi, T. Turko, D. Cianfarani, S. Barre, W. Uhring, U. Hassiepen, and J. Leonard, "Towards sensitive, high-throughput, biomolecular assays based on fluorescence lifetime," *Methods and Applications in Fluorescence*, vol. 5, no. 3, p. 8, 2017. [Online]. Available: <GotoISI>://WOS:000411521300001

[119] O. Caen, S. Schutz, M. S. S. Jammalamadaka, J. Vrignon, P. Nizard, T. M. Schneider, J. C. Baret, and V. Taly, "High-throughput multiplexed fluorescence-activated droplet sorting," *Microsystems & Nanoengineering*, vol. 4, p. 10, 2018. [Online]. Available: <GotoISI>://WOS:000447751200001

[120] R. Ebrahimifard, S. van den Driesche, H. Breiteneder, C. Hafner, and M. J. Vellekoop, "An infrared sensor system for the analysis and differentiation of living mammalian cells using d2o based microfluidics," *Sensors and Actuators B-Chemical*, vol. 247, pp. 981–991, 2017. [Online]. Available: <GotoISI>://WOS:000402465000121

[121] H. A. J. Al Lawati, E. Al Gharibi, S. M. Z. Al Kindy, F. E. O. Suliman, and A. M. Al-Lawati, "High throughput method for the analysis of cetrizine hydrochloride in pharmaceutical formulations and in biological fluids using a tris(2,2 '-bipyridyl)ruthenium(ii)-peroxydisulphate chemiluminescence system in

a two-chip device," *Talanta*, vol. 85, no. 2, pp. 906–912, 2011. [Online]. Available: <GotoISI>://WOS:000293116600010

[122] K. J. Klunder, K. M. Clark, C. McCord, K. E. Berg, S. D. Minteer, and C. S. Henry, "Polycaprolactone-enabled sealing and carbon composite electrode integration into electrochemical microfluidics," *Lab on a Chip*, vol. 19, no. 15, pp. 2589–2597, 2019. [Online]. Available: <GotoISI>://WOS:000476768900006

[123] D. Craig, M. Mazilu, and K. Dholakia, "Quantitative detection of pharmaceuticals using a combination of paper microfluidics and wavelength modulated raman spectroscopy," *Plos One*, vol. 10, no. 5, p. 10, 2015. [Online]. Available: <GotoISI>://WOS:000353943000006

[124] K. O'Dwyer, R. Mouras, A. A. Mani, D. Rice, M. Gleeson, N. Liu, S. A. M. Tofail, and C. Silien, "Label-free multimodal coherent anti-stokes raman scattering analysis of microparticles in unconstrained microfluidics," *Applied Optics*, vol. 57, no. 22, pp. E32–E36, 2018. [Online]. Available: <GotoISI>://WOS:000440439900005

[125] G. Bergner, S. Chatzipapadopoulos, D. Akimov, B. Dietzek, D. Malsch, T. Henkel, S. Schlucker, and J. Popp, "Quantitative cars microscopic detection of analytes and their isotopomers in a two-channel microfluidic chip," *Small*, vol. 5, no. 24, pp. 2816–2818, 2009. [Online]. Available: <GotoISI>://WOS:000273412000009

[126] C. F. A. d. A. R. d. Cunha-Matos, "Real-time, high-throughput assessment of nanoparticle interactions with single-cells using microfluidics : applications in vaccine development," Thesis, 2017.

[127] K. Domansky, D. C. Leslie, J. McKinney, J. P. Fraser, J. D. Sliz, T. Hamkins-Indik, G. A. Hamilton, A. Bahinski, and D. E. Ingber, "Clear castable polyurethane elastomer for fabrication of microfluidic devices," *Lab on a Chip*, vol. 13, no. 19, pp. 3956–3964, 2013. [Online]. Available: <GotoISI>://WOS:000323835700021

[128] E. W. K. Young, E. Berthier, D. J. Guckenberger, E. Sackmann, C. Lamers, I. Meyvantsson, A. Huttenocher, and D. J. Beebe, "Rapid prototyping of arrayed microfluidic systems in polystyrene for cell-based assays," *Analytical Chemistry*, vol. 83, no. 4, pp. 1408–1417, 2011. [Online]. Available: <GotoISI>://WOS:000287176900037

[129] A. Muck, J. Wang, M. Jacobs, G. Chen, M. P. Chatrathi, V. Jurka, Z. Vyborny, S. D. Spillman, G. Sridharan, and M. J. Schoning, "Fabrication of poly(methyl methacrylate) microfluidic chips by atmospheric molding," *Analytical Chemistry*, vol. 76, no. 8, pp. 2290–2297, 2004. [Online]. Available: <GotoISI>://WOS:000221096800018

[130] K. Matsuno, "The treatment of hydrofluoric acid burns," *Occupational Medicine-Oxford*, vol. 46, no. 4, pp. 313–317, 1996. [Online]. Available: <GotoISI>://WOS:A1996VF29900010

[131] K. N. Ren, J. H. Zhou, and H. K. Wu, "Materials for microfluidic chip fabrication," *Accounts of Chemical Research*, vol. 46, no. 11, pp. 2396–2406, 2013. [Online]. Available: <GotoISI>://WOS:000327360800006

[132] Z. X. Wang, A. A. Volinsky, and N. D. Gallant, "Crosslinking effect on polydimethylsiloxane elastic modulus measured by custom-built compression instrument," *Journal of Applied Polymer Science*, vol. 131, no. 22, p. 4, 2014. [Online]. Available: <GotoISI>://WOS:000341179900008

[133] J. H. Carpenter, "New measurements of oxygen solubility in pure and natural water," *Limnology and Oceanography*, vol. 11, no. 2, pp. 264–+, 1966. [Online]. Available: <GotoISI>://WOS:A19667752500014

[134] G. Stojkovic, M. Krivec, A. Vesel, M. Marinsek, and P. Znidarsic-Plazl, "Surface cell immobilization within perfluoroalkoxy microchannels," *Applied Surface Science*, vol. 320, pp. 810–817, 2014. [Online]. Available: <GotoISI>://WOS:000345399900111

[135] D. Chatterjee, B. Hetayothin, A. R. Wheeler, D. J. King, and R. L. Garrell, "Droplet-based microfluidics with nonaqueous solvents and solutions," *Lab on a Chip*, vol. 6, no. 2, pp. 199–206, 2006. [Online]. Available: <GotoISI>://WOS:000235684900011

[136] S. L. Liao, Y. L. He, Y. J. Chu, H. G. Liao, and Y. P. Wang, "Solvent-resistant and fully recyclable perfluoropolyether-based elastomer for microfluidic chip fabrication," *Journal of Materials Chemistry A*, vol. 7, no. 27, pp. 16 249–16 256, 2019. [Online]. Available: <GotoISI>://WOS:000475689800015

[137] Y. D. Ren, C. M. Crump, M. M. Mackley, G. Li Puma, and N. M. Reis, "Photo inactivation of virus particles in microfluidic capillary systems," *Biotechnology and Bioengineering*, vol. 113, no. 7, pp. 1481–1492, 2016. [Online]. Available: <GotoISI>://WOS:000377527900010